arXiv:2512.17534v1 [physics.flu-dyn] 19 Dec 2025

HydroGym: A Reinforcement Learning Platform for Fluid Dynamics

Christian Lagemann[1,2], Sajeda Mokbel[1,2], Miro Gondrum[3], Mario Rüttgers[4], Jared Callaham[1,2], Ludger Paehler[5], Samuel Ahnert[1,2], Nicholas Zolman[1,2], Kai Lagemann[6], Nikolaus Adams[5], Matthias Meinke[3], Wolfgang Schröder[3], Jean-Christophe Loiseau[7], Esther Lagemann[1,2], and Steven L. Brunton[1,2]

[1]*Department of Mechanical Engineering, University of Washington, Seattle, WA 98195, United States*
[2]*AI Institute in Dynamic Systems, University of Washington, Seattle, WA 98195, United States*
[3]*Chair of Fluid Mechanics and Institute of Aerodynamics, RWTH Aachen University, Aachen, Germany*
[4]*Data-Driven Fluid Engineering Laboratory, Inha University, Incheon, South Korea*
[5]*School of Engineering and Design, Technical University of Munich, Munich, Germany*
[6]*Statistics and Machine Learning, German Center for Neurodegenerative Diseases, Bonn, Germany*
[7]*Arts et Métiers Institute of Technology, CNAM, DynFluid, HESAM Université, Paris, France*

Abstract

Modeling and controlling fluid flows is critical for several fields of science and engineering, including transportation, energy, and medicine. Effective flow control can lead to, e.g., lift increase, drag reduction, mixing enhancement, and noise reduction. However, controlling a fluid faces several significant challenges, including high-dimensional, nonlinear, and multiscale interactions in space and time. Reinforcement learning (RL) has recently shown great success in complex domains, such as robotics and protein folding, but its application to flow control is hindered by a lack of standardized benchmark platforms and the computational demands of fluid simulations. To address these challenges, we introduce HydroGym, a solver-independent RL platform for flow control research. HydroGym integrates sophisticated flow control benchmarks, scalable runtime infrastructure, and state-of-the-art RL algorithms. Our platform includes 42 validated environments spanning from canonical laminar flows to complex three-dimensional turbulent scenarios, validated over a wide range of Reynolds numbers. We provide non-differentiable solvers for traditional RL and differentiable solvers that dramatically improve sample efficiency through gradient-enhanced optimization. Comprehensive evaluation reveals that RL agents consistently discover universal control principles across configurations, such as boundary layer manipulation, acoustic feedback disruption, and wake reorganization, leading to drag reductions exceeding 90%. Transfer learning studies demonstrate that controllers learned at one Reynolds number or geometry adapt efficiently to new conditions, requiring approximately 50% fewer training episodes. These findings suggest RL uncovers invariant mathematical structures governing separated flows, with profound implications for developing generalizable control strategies. The HydroGym platform is highly extensible and scalable, providing a framework for researchers in fluid dynamics, machine learning, and control to add environments, surrogate models, and control algorithms to advance science and technology.

Keywords: reinforcement learning, flow control, fluid dynamics, benchmark platform, reproducible science

Fluid flow control represents a critical challenge in several trillion-dollar industries including transportation (e.g., aerospace, automotive, shipping), energy production (e.g., wind farms, gas turbines, pipelines), manufacturing (e.g., spray processes, metal additive manufacturing, thin films and coatings), and medicine (e.g., circulatory and respiratory systems, glymphatic system). Advanced control systems could dramatically improve energy efficiency across global operations, for example enabling the aviation industry to reduce fuel consumption by up to 15% through active drag reduction [1–4], or increasing wind farm output by 4-5% through coordinated control [5–7], representing substantial economic gains. A comprehensive analysis of the economic significance and industrial applications of flow control is provided in the *Extended Introduction* (Supplementary Information).

Despite decades of progress in traditional control approaches, the nonlinear, multiscale nature of turbulence results in control problems that are high-dimensional, nonconvex, and computationally intractable using conventional methods [8–11]. Recent breakthroughs in reinforcement learning (RL) have demonstrated transformative capabilities across increasingly complex scientific applications, with AlphaFold revolutionizing protein structure

*Corresponding authors: S.L. Brunton (sbrunton@uw.edu) & C. Lagemann (clage@uw.edu)

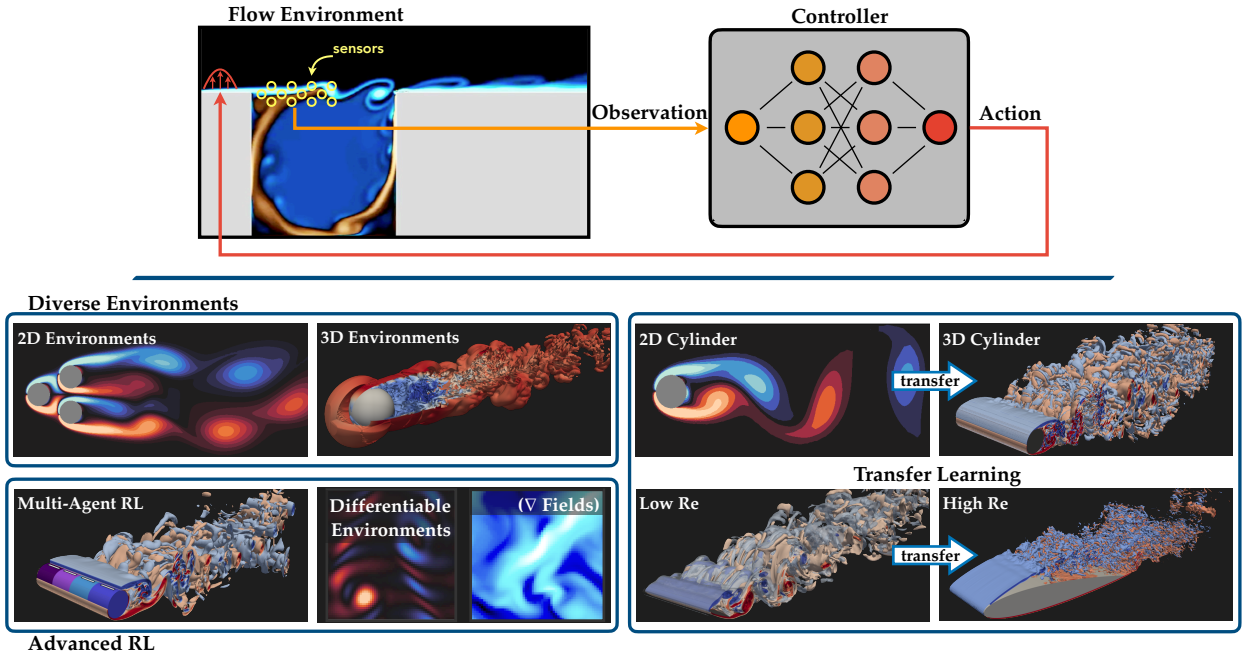

Figure 1: HydroGym reinforcement learning platform architecture for fluid dynamics control. The platform features a unified interface connecting flow environments with RL controllers through standardized observation-action loops (top), exemplified here by jet-based actuation control of an open cavity flow. HydroGym's key capabilities include: scalable environments from 2D to 3D configurations with systematic Reynolds number variations; transfer learning pathways enabling knowledge transfer across geometric configurations, Reynolds numbers, and dimensionality; and advanced RL methods including fully differentiable physics environments for gradient-enhanced optimization and multi-agent frameworks for spatially distributed control. All environments maintain compatibility with standard RL algorithms while supporting diverse computational backends.

prediction [12] and DeepMind achieving real-time control of fusion reactor plasmas [13]. These successes share a common enabler: benchmark environments that democratize research access and accelerate algorithmic innovation.

However, fluid dynamics has remained largely resistant to similar breakthroughs due to fundamental computational and accessibility barriers. Training effective RL agents typically requires thousands or millions of interactions with the environment, and each evaluation in a fluid environment requires expensive computational fluid dynamics (CFD) simulations [14–16]. This bottleneck is magnified by the inherent sample inefficiency of model-free RL [17, 18], creating severe computational limitations for large-scale flow control problems [19–21].

Moreover, controllers trained at specific flow conditions may fail to generalize to different regimes. Flow control demonstrations require an immense amount of scientific computing and domain expertise, providing a significant barrier to entry. Only a few groups worldwide have the computational resources and the combination of fluid dynamics and reinforcement learning expertise to demonstrate real advances. Unlike computer vision's ImageNet [22] or robotics' MuJoCo environments [23] that transformed their respective fields, fluid dynamics researchers lack comprehensive control benchmark platforms for systematic algorithmic comparison and reproducible research. For a review of RL applications in flow control, including shape optimization, and turbulence modeling advances, see the *Extended Literature Review* (Supplementary Information).

We address these fundamental challenges in HydroGym, a reinforcement learning platform for flow control research. Our solver-independent architecture provides forty-two validated flow control environments spanning canonical laminar flows to advanced three-dimensional turbulent scenarios, Reynolds number progressions across flow regimes to enable transfer learning, and differentiable physics implementations that dramatically reduce sample complexity through gradient-enhanced information.

The platform's key innovations, illustrated in Fig. 1, include: (1) **Computational tractability** through efficient simulation interfaces and differentiable environments that enable gradient-based policy optimization; (2) **Systematic benchmarking with standardized environments** covering 2D and 3D configurations across multiple Reynolds number regimes; (3) **Transfer learning capabilities** that enable knowledge transfer across geometric configurations, Reynolds numbers, and flow dimensionality; and (4)

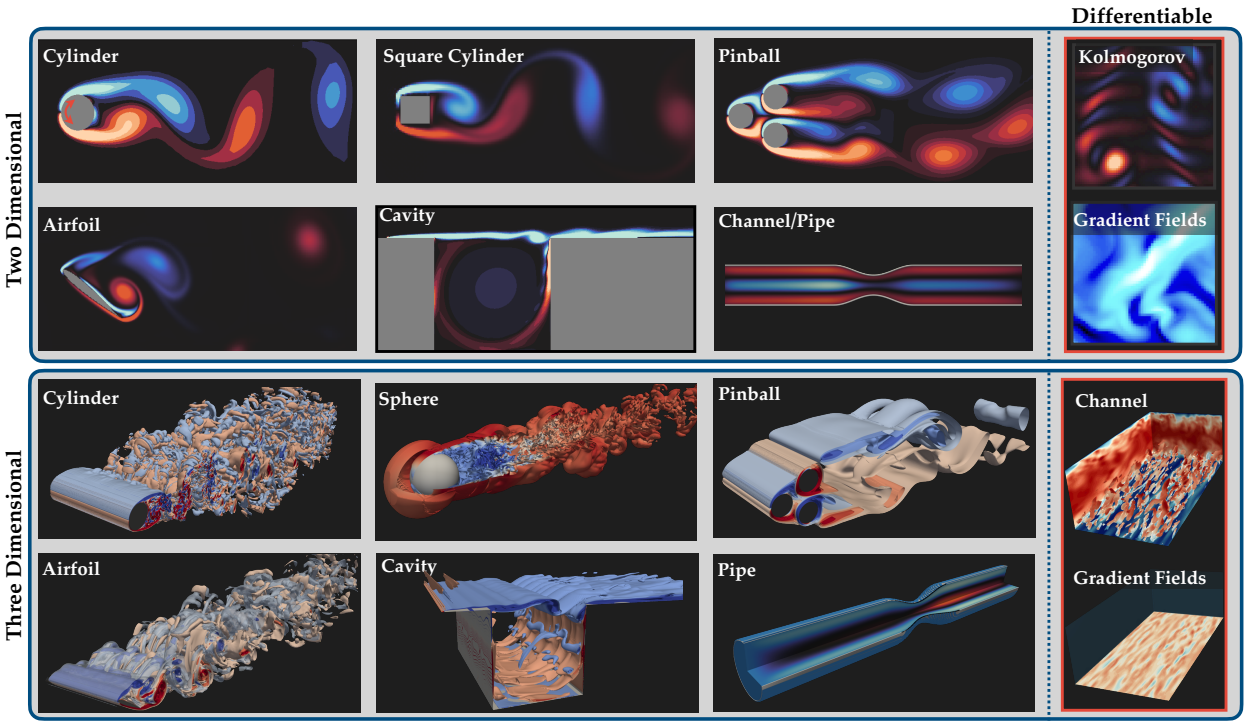

Figure 2: Comprehensive benchmark suite of HydroGym's 42+ fluid dynamics environments. The collection spans fundamental flow configurations in or around generic and real-world inspired geometries such as cylinders or spheres, airfoils, cavities, and pipes across both two-dimensional and three-dimensional domains. Each environment category includes systematic Reynolds number variations to capture different flow regimes from laminar to turbulent conditions. Special environments include differentiable physics implementations that enable gradient-based optimization methods. This standardized suite provides consistent benchmarking capabilities for systematic evaluation and comparison of reinforcement learning algorithms across diverse active flow control challenges.

Integration of advanced RL frameworks including multi-agent coordination for spatially distributed control. The versatility of this platform enables unprecedented transfer learning across flow configurations and geometries, allowing RL agents to discover universal control principles that we demonstrate generalize across diverse setups. These strategies include boundary layer manipulation, acoustic feedback disruption, and wake reorganization.

HydroGym provides the foundational infrastructure for systematic progress in RL-based flow control. This testbed enables researchers in fluid dynamics and RL to collaboratively develop environments, sample-efficient algorithms, physics-informed architectures, and generalizable strategies that transfer across flow conditions and geometric configurations. Just as standardized platforms catalyzed breakthroughs in protein folding and plasma control, HydroGym establishes a pathway for advancing modern RL methods to fluid dynamics.

The HydroGym Platform

HydroGym addresses the computational and accessibility barriers that prevent widespread adoption of reinforcement learning in fluid flow control, based on three core design principles: solver independence, comprehensive benchmarking, and scalable complexity. The platform abstracts CFD implementation from control algorithms while maintaining physical fidelity, enabling researchers from both machine learning and fluid dynamics communities to collaborate effectively without requiring deep expertise in both domains. The framework encompasses at present forty-two distinct flow scenarios across thirteen geometric configurations, systematically organized to cover multiple Reynolds number regimes within each configuration (see Fig 2). This progression enables the investigation of control strategies across different physical regimes, from laminar vortex shedding at low Reynolds numbers to transitional and turbulent dynamics at higher Reynolds numbers. It also facilitates transfer learning between related flow conditions. The benchmark suite includes classical bluff body flows (cylinders, squares, cubes, spheres) exhibiting vortex shedding, cavity flows with shear layer instabilities, airfoils under gust conditions, and the biomedically-relevant stenotic pipe flows. For a detailed technical documentation, including numerical implementations (Sections 3-4), comprehensive environment

specifications (Section 5), and validation studies for all flow configurations, see the Supplementary Information.

Computational Backends and Solver Integration. HydroGym's modular architecture supports three distinct computational backends optimized for different research requirements and computational resources: (1) The high-performance lattice Boltzmann method (LBM) solver, built on the m-AIA framework [24], enables large-scale simulations on high-performance computing systems through CPU/GPU parallelization. (2) A JAX-based implementation provides automatic differentiation [25] through complete simulation trajectories, enabling gradient-enhanced reinforcement learning methods that dramatically improve sample efficiency. (3) The Python-based Firedrake finite element backend prioritizes code transparency and extensibility for non-CFD experts, offering researchers complete access to solver internals for method development and validation due to a pure-Python implementation [26].

Each backend maintains a unified Gymnasium interface [27] that standardizes interaction between RL algorithms and fluid simulations, abstracting solver-specific details while preserving essential physics. The platform's intuitive design is exemplified by its straightforward initialization and interaction pattern as shown for an open cavity control example in the following:

```
import hydrogym

# initialize environment
env = hydrogym.FlowEnv(flow=hydrogym.Cavity,
                       solver=hydrogym.MAIA,
                       observation="pressure")

# reset environment
obs, info = env.reset()

# interact with environment
action = 0.0
for i in range(num_interactions):
    obs, reward, terminated, truncated, info = env.step(
        action=0.0)
```

This design enables control engineers to focus on algorithm development without CFD expertise, while providing fluids researchers access to state-of-the-art RL techniques. The solver-independent architecture ensures that advances in CFD can be seamlessly integrated into the platform without disrupting existing workflows.

Environment Design and Validation Framework. Each HydroGym environment follows a standardized framework that balances physical fidelity with computational tractability for iterative RL training. Environments include configurable reward functions targeting specific control objectives (typically drag reduction, flow stabilization, or mixing enhancement), flexible actuation mechanisms (jet-based control, surface motion, or temperature modulation), and adaptable sensor configurations through point probe measurements of flow quantities. The temporal coupling between CFD solvers and RL agents is carefully calibrated to match characteristic flow timescales while maintaining computational efficiency. Comprehensive validation studies demonstrate that our numerical implementations achieve excellent agreement with established benchmarks in the literature across all flow configurations. This validation foundation ensures that control strategies discovered through RL training reflect genuine physical mechanisms rather than numerical artifacts.

Differentiable Environments and Multi-Agent Control. HydroGym incorporates two advanced capabilities that distinguish it from existing flow control platforms. Differentiable environments leverage automatic differentiation through JAX-based solvers to compute exact policy gradients with respect to flow dynamics. This gradient-enhanced approach offers new ways to address the sample efficiency limitations that have historically prevented RL in computationally expensive flow problems. Substantial improvements in training convergence of RL methods were achieved compared to model-free methods [28–31].

Multi-agent reinforcement learning enables spatially distributed control strategies for large-scale applications. The platform decomposes global agents into multiple local agents, each managing actuator pairs distributed along flow boundaries. This architecture naturally scales with actuator count while maintaining computational tractability by exploiting spatial locality in flow physics. Agents share gradient information and experience buffers to enhance learning efficiency while specializing in local flow dynamics, enabling more robust and generalizable control policies than single-agent approaches [32].

Systematic Evaluation of RL Algorithms for Flow Control

The following sections demonstrate the platform's capabilities across this diverse environment suite, establishing baseline performance metrics using industry-standard RL algorithms including Proximal Policy Optimization (PPO) [33], Deep Deterministic Policy Gradient (DDPG) [34], and Twin Delayed Deep Deterministic Policy Gradient (TD3) [35]. Our implementation leverages established frameworks from TorchRL [36] and CleanRL [37] to ensure reproducible benchmarks and facilitate direct comparison with existing literature. These algorithms rep-

resent both policy-based and value-based approaches to continuous control, providing comprehensive coverage of modern RL methodologies for flow control applications. The extensive training effort—exceeding 150,000 GPU hours—produces validated benchmarks that allow researchers to immediately build upon state-of-the-art baselines rather than investing months in reproducing foundational results. More details regarding the baseline algorithms can be found in Section 4 of the Supplementary Information. The results reveal the complex control challenges that characterize different flow regimes while providing both validation of the platform's technical implementation and a foundation for future algorithmic developments leveraging HydroGym's unique combination of efficiency, physical fidelity, and accessibility.

These demonstrations reveal how RL agents autonomously discover key flow phenomena, such as boundary layer energization, acoustic feedback disruption, and wake management, through interaction alone, without explicit knowledge of these mechanisms. The agents learn to exploit the intrinsic physics of separated flows, transforming detrimental flow features into controlled, organized states while minimizing actuation. This foundation establishes the platform's capability to support both fundamental flow physics investigations and practical control system development across diverse applications.

Two-Dimensional Flow Control Demonstrations. The platform's effectiveness is demonstrated through detailed analysis of four benchmark scenarios that collectively represent the breadth of flow control challenges addressable within HydroGym. Each case study reveals how RL agents exploit specific flow physics to achieve control objectives, providing algorithmic validation and physical insights into the underlying control mechanisms.

Fluidic pinball control at $Re = 100$. We begin with the fluidic pinball at $Re = 100$, where three cylinders in an equilateral formation create wake interactions that demonstrate coordinated multi-actuator control. The uncontrolled system exhibits natural flow asymmetry with a permanent deflection of the incoming flow and irregular pressure oscillations, establishing a benchmark for multi-input multi-output flow control. As shown in Fig. 3, RL agents discover a coordinated rotation strategy achieving approximately 90% in total drag reduction through counterrotating rear cylinders. This actuation creates a high-velocity jet to inject momentum into the wake centerline, preventing shear layer interaction and suppressing vortex formation. The rotation-induced circulation generates Magnus forces that create favorable pressure gradients, vectoring separated shear layers inward while energizing boundary layers through momentum addition. This delays separation on the advancing cylinder sides and promotes controlled separation on retreating sides, fundamentally restructuring the wake topology. Moreover, the coordinated actuation establishes steady momentum injection that opposes adverse pressure gradients in the base region, mimicking splitter plate effects by preventing communication between upper and lower wake regions. Hence, the learned control policies transform irregular, asymmetric shedding into steady, symmetric base flow with narrowed effective width, reduced velocity deficits, and enhanced pressure recovery, demonstrating how targeted boundary layer manipulation can suppress complex dynamics in multi-body fluid systems.

Open cavity flow control at $Re = 4,200$. Moving to higher Reynolds numbers, the cavity flow at Re=4,200 illustrates control where small interventions can prevent transition to unsteady flow. The flow represents a balance between stabilizing viscous forces and destabilizing inertial effects, positioning it precisely at the threshold where small perturbations can trigger transition from steady recirculating flow to unsteady vortex shedding. In the uncontrolled state, the shear layer just downstream of the cavity edge exhibits weakly growing instabilities that manifest as low-amplitude pressure oscillations and incipient vortical structures (see Fig. 3). The flow field is characterized by a large, quasi-steady recirculation zone within the cavity and a thin, marginally stable free shear layer spanning the cavity opening. The reinforcement learning agent discovers a control strategy that exploits the marginal nature of this flow regime through targeted momentum injection at the upstream cavity edge. The optimal policy employs controlled blowing to modify the velocity profile and momentum thickness of the separating boundary layer, shifting the local stability characteristics away from critical conditions. This actuation thickens the separating shear layer and reduces the velocity gradient across the mixing region, thereby suppressing Kelvin-Helmholtz instability growth before it can amplify into coherent vortical structures. By stabilizing the shear layer, the control disrupts the acoustic feedback loop between vortex impingement at the downstream edge and upstream receptivity, damping the Rossiter modes and maintaining steady flow conditions. The successful control reduces the strength of the recirculation zone within the cavity, eliminating the unsteady loads characteristic of supercritical cavity flows. The strategy demonstrates that small control inputs applied at near-critical conditions can produce disproportionately large stabilization effects.

Circular cylinder control at $Re = 3,900$. The circular cylinder at $Re = 3,900$ displays shear layer instabilities, irregular shedding frequencies, and chaotic vortex patterns in the

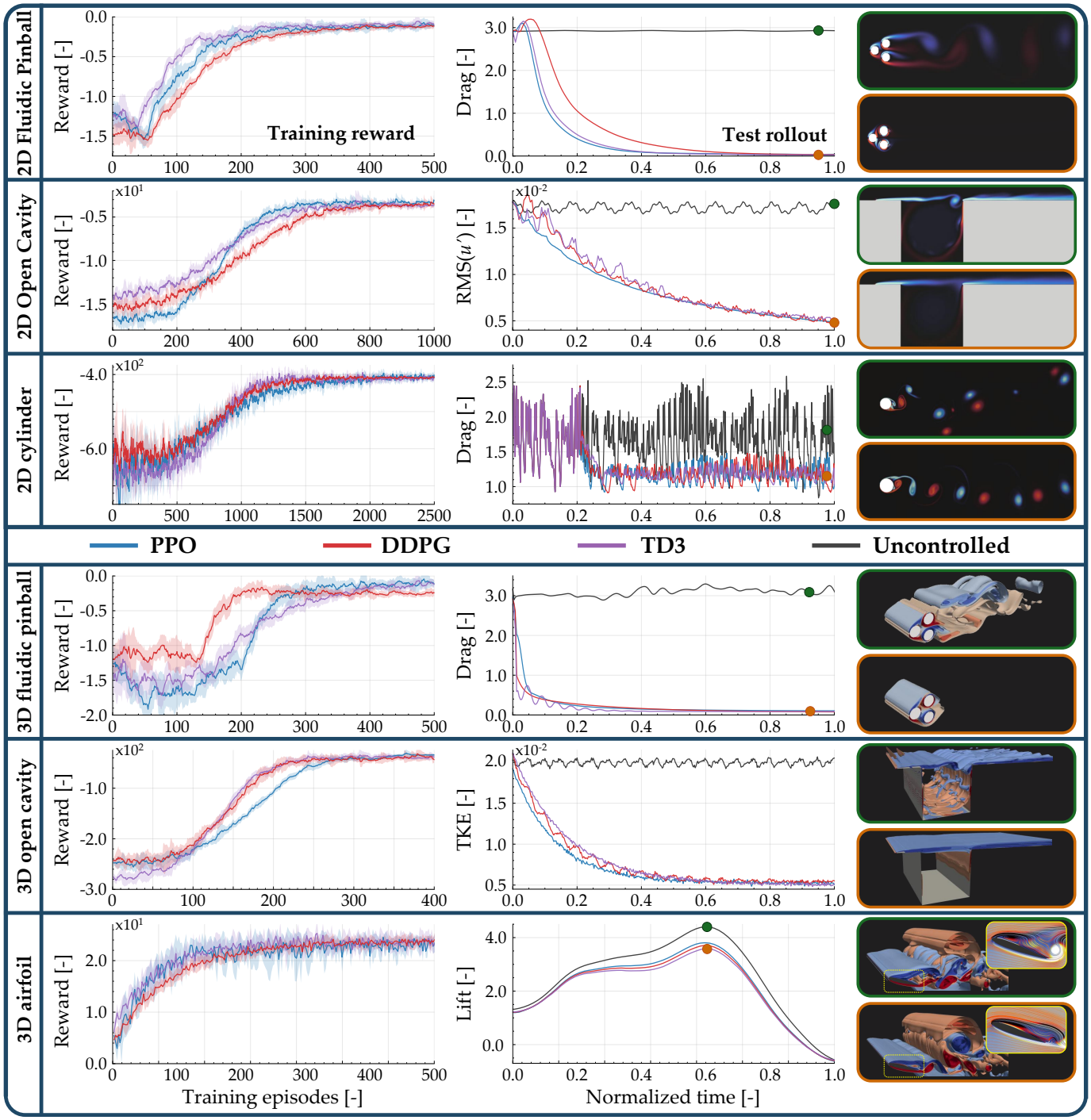

Figure 3: Reinforcement learning performance across two- and three-dimensional flow control environments. Training curves (left) show convergence behavior for PPO, DDPG, and TD3 algorithms across six benchmark scenarios: three 2D environments—fluidic pinball ($Re = 100$), open cavity ($Re = 4,200$), and cylinder ($Re = 3,900$)—and three 3D environments—fluidic pinball ($Re = 150$), open cavity ($Re = 7,500$), and gust-airfoil interaction ($Re = 1,000$). Test rollouts (right) demonstrate control effectiveness through drag reduction metrics, revealing the agents' ability to manage both two-dimensional flow reorganization and complex three-dimensional phenomena including spanwise instabilities, acoustic feedback loops, and turbulent structures. Flow visualizations highlight the sophisticated wake manipulation and flow control achieved through learned policies across increasing geometric complexity. All shown training results leverage the m-AIA solver.

wake. In this flow, RL agents discover a control strategy that reorganizes this system into coherent, predictable flow patterns. Operating under a zero-net mass flux constraint, where opposing jets maintain equal and opposite mass flow rates, the controller implements boundary layer manipulation that effectively streamlines the cylinder without adding or removing mass. The learned policy exploits asymmetric pressure distributions through coordinated suction and injection. Upper-surface suction removes low-momentum boundary layer fluid, compensating adverse pressure gradients and delaying separation, while lower-surface blowing energizes the boundary layer through direct momentum injection. This creates a time-varying "virtual geometry" that actively manages wake formation. The transformation is striking: a chaotic, three-dimensional wake is replaced by coherent vortical patterns that shed with improved regularity and symmetry. Separation points shift downstream, narrowing the wake and reorganizing the momentum deficit structure. The controlled wake converts a random turbulent wake into ordered momentum transport. This demonstrates how localized boundary layer control can transform chaotic turbulent structures into predictable flow patterns.

Three-Dimensional Flow Control Demonstrations. We also extensively study three-dimensional flows, which exhibit emergent phenomena, e.g. acoustic resonances, spanwise instabilities, and complex vortex interactions. The following demonstrations show how RL agents discover sophisticated strategies that exploit these 3D effects, revealing counterintuitive control principles that often challenge conventional flow control approaches.

Fluidic pinball control at $Re = 150$. The fluidic pinball at a Reynolds number $Re = 150$ represents a highly chaotic flow, exhibiting bifurcating vortex shedding with chaotic fluctuations, and serving as a paradigm for understanding multi-body flow interactions in natural and engineered systems. As shown in Fig. 3, RL agents discover a control strategy achieving over 93% drag reduction through coordinated cylinder rotation, revealing a fundamental principle: asymmetric forcing paradoxically creates symmetric flow. The learned policy employs counter-rotating rear cylinders with asymmetric front cylinder actuation, exploiting Magnus-induced circulation to streamline the flow through the Coanda effect. The physical mechanism disrupts the Kelvin-Helmholtz instability by asymmetrically modifying boundary layer separation. This transforms alternating von Kármán vortex streets into two independent, non-interacting shear layers, eliminating large-scale vortex interactions and converting chaotic dynamics into purely harmonic flow. As a result, the control strategy reduces velocity deficits in the wake, increases the base pressure, and narrows the wake width dramatically. This RL-driven control policy challenges conventional flow control approaches and establishes asymmetric forcing as a reliable principle for chaos suppression in multi-body fluid systems.

Open cavity flow control at Re=7,500. Cavity flows are challenged by a variety of dominant timescales and acoustic feedback mechanisms that couple flow instabilities with sound waves. At $Re = 7,500$, the three-dimensional cavity exhibits a well-developed feedback mechanism where the shear layer at the upstream edge develops into coherent vortical structures. These structures convect downstream at approximately half the freestream velocity and impinge upon the downstream cavity edge, generating acoustic waves that propagate back upstream at the speed of sound to excite the shear layer at the separation point. This resonant feedback establishes dominant cavity tones and creates intense pressure oscillations and complex three-dimensional flow features including spanwise variations in vortex strength and oblique vortex shedding modes. The flow exhbits spanwise instabilities that lead to vortex stretching, tilting, and the formation of streamwise vortical structures within the recirculation zone. These secondary flows enhance mixing and modify the downstream acoustic signature, creating a rich spectrum of cavity tones and broadband noise. The RL agents discover a sophisticated control strategy that exploits the temporal and spatial characteristics of this instability. Coordinated blowing and suction actuators operate with temporal modulation to disrupt the acoustic feedback loop while addressing three-dimensional flow structures. High-frequency, low-amplitude blowing at the upstream cavity edge artificially thickens the separating boundary layer and introduces controlled perturbations that interfere destructively with the natural Kelvin-Helmholtz instabilities. This upstream control modifies the two-dimensional roll-up process and the three-dimensional breakdown mechanisms that otherwise generate coherent spanwise vortices (see Fig. 3). Strategically placed suction near the downstream edge weakens the acoustic source by reducing the vortex-edge interactions and mitigating the formation of strong pressure gradients that drive the acoustic waves. The coordinated actuation achieves near-complete suppression of the dominant cavity tones while controlling the three-dimensional secondary flows. This results in a stable flow configuration that significantly reduces the size and complexity of the recirculation zone, also reducing unsteady loading.

Transverse gust mitigation at $Re = 1,000$. Gust mitigation is a fundamentally different control task requiring real-time adaptation. At a post-stall angle of attack $\alpha = 20°$, the separated flow around a NACA0012 airfoil exhibits a laminar separation bubble with periodic vortex shedding

from the leading and trailing edges. Under transverse gusts with gust ratio $G = u_g/u_\infty = 2$, where u_g is the characteristic gust velocity and u_∞ is the freestream velocity, the flow experiences dramatic load fluctuations as the effective angle of attack varies rapidly, creating vortex-gust interactions that compromise aerodynamic performance. The RL agents discover an adaptive control strategy utilizing three leading-edge jet actuators that alter the separated dynamics. The optimal control policy employs momentum injection directly into the separated shear layer, creating a more compact and energetic separation bubble that generates stronger, more coherent primary vortices. These enhanced vortices maintain higher circulation strength and spatial coherence compared to the uncontrolled baseline, establishing organized vortex structures that resist the destabilizing effects of transverse gust encounters. As shown in Fig. 3, the coordinated actuation strategy alleviates loads during gust encounters by synchronizing the controlled vortex shedding with the natural flow response. The resulting wake exhibits reduced velocity deficit and decreased turbulence intensity, enabling the airfoil to maintain stable aerodynamic performance.

Transfer Learning Capabilities. A fundamental question raised by these diverse control demonstrations is whether discovered mechanisms represent configuration-specific solutions or more generalizable approaches. To address this, we systematically investigate how control knowledge transfers across Reynolds numbers, geometries, and dimensions, showing that HydroGym enables efficient transfer learning to reduce computational requirements and improve controller generalization.

Fine-tuned policies achieve optimal performance in approximately 50% of the episodes compared to training from scratch (see Fig.4, rows 1 & 2), with drag reduction effectiveness maintained or improved across the tested range. This indicates that flow control strategies capture scale-invariant physics, particularly pressure gradient manipulation and momentum injection timing relative to vortex formation cycles. The effectiveness across Reynolds numbers suggests that the learned policies identify fundamental scaling relationships across flow regimes.

Beyond Reynolds number invariance, the policies demonstrate geometric transferability. Control strategies for vortex shedding suppression learned on circular cylinders effectively manage vortex shedding in square geometries. This supports the notion that policies learn mathematical structures governing pattern formation and symmetry breaking that persist across boundary conditions, rather than geometry-specific control (see Fig.4, row 3). The policies capture fundamental wake manipulation principles sufficiently general to accommodate corner effects and different separation characteristics.

The most stringent test is dimensional transfer from 2D to 3D, which confirms universality across spatial scales. Despite the increased complexity of three-dimensional flows, including spanwise coupling effects and additional instability modes, pre-trained 2D control strategies successfully delay separation and maintain effective drag reduction in 3D applications while reducing computational costs by $\approx 50 - 60\%$ (see Fig.4 - row 4). This indicates that boundary layer manipulation strategies transcend spatial dimensionality through conserved scaling laws and similarity parameters, with 2D training capturing the dominant flow physics relevant for 3D control.

The transfer mechanism itself provides insights into learning. While zero-shot performance varies across scenarios, the subsequent fine-tuning process consistently benefits from pre-trained initialization, even when immediate transfer appears limited. This pattern suggests that learned policies encode fundamental flow control relationships that may not manifest immediately in performance metrics but provide essential structure for accelerated learning, indicating that deep RL discovers mathematical invariants governing scaled flow problems.

These findings establish HydroGym's capability for systematic transfer learning in flow control. Rather than requiring individual solutions for each configuration, the platform enables learning across conditions, reducing computational cost dramatically. This systematic transfer capability could enable more efficient learning approaches where knowledge from accessible laboratory conditions is adapted for challenging deployment scenarios. Moreover, the convergence with foundation model architectures presents unprecedented opportunities. Models trained on comprehensive flow physics datasets could encode universal fluid dynamics principles, enabling zero-shot transfer to novel applications based on learned physical relationships rather than configuration-specific training. This evolution toward self-improving control systems represents a paradigm shift from static controllers to agents that improve through continuous environmental interaction while maintaining physical interpretability.

Differentiable environments and multi-agent RL. While conventional reinforcement learning has proven effective for flow control, emerging RL paradigms offer fundamentally different approaches to optimization and learning efficiency. HydroGym's advanced capabilities demonstrate how differentiable reinforcement learning exploits gradient information through entire simulation trajectories, enabling more efficient policy optimization, while multi-agent frameworks address the spatial complexity of three-dimensional flows through distributed actuator coordination. Together, these approaches provide direct access to sensitivity information and enable scalable solutions for complex 3D control scenarios.

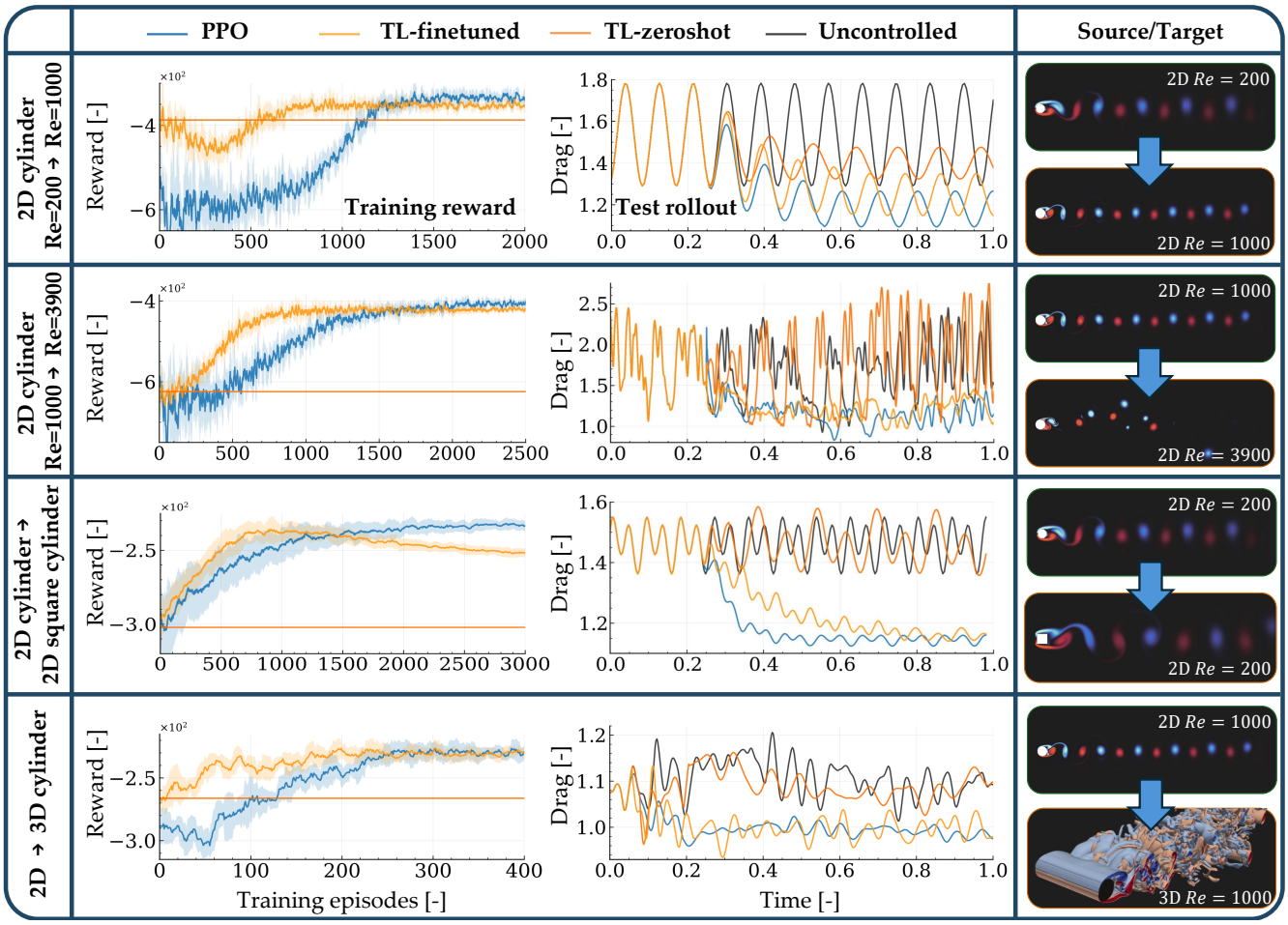

Figure 4: Transfer learning capabilities across flow configurations and conditions. Four transfer scenarios demonstrate knowledge generalization: Reynolds number scaling ($Re = 200 \rightarrow 1,000$, $Re = 1000 \rightarrow 3,900$), geometric transfer (circular to square cylinder), and dimensional scaling (2D to 3D cylinder). Training curves compare standard PPO training with transfer learning (finetuned and zeroshot). Finetuned policies consistently achieve faster convergence, requiring approximately half the training episodes of baseline methods. Test rollouts confirm that improved training efficiency translates to effective control performance, with drag reduction across all transfer scenarios.

Gradient-enhanced policy optimization through differentiable physics. In contrast to traditional CFD solvers like m-AIA or Firedrake, which lack native automatic differentiation capabilities, modern AD libraries enable physics solvers to compute sensitivities of objective functions with respect to control parameters and actuator placement, even through complex physical processes. This capability allows policy optimization using sensitivity information, yielding improved performance and sample efficiency [38, 39], which is particularly valuable for computationally intensive fluid simulations in RL training. We demonstrate this approach using the HydroGym framework with two JAX-based differentiable environments. The first is a 3D channel flow at $\mathrm{Re}_\tau = 180$, a moderately turbulent regime amenable to direct numerical simulation. It exhibits multiscale physics including large vortical structures and near-wall velocity sweeps and streaks [40]. This flow provides an ideal testbed for wall-shear stress reduction in boundary layers [41]. We compared standard PPO against gradient-augmented PPO (GPPO), where agents controlled zero-mass-flux jets via blowing and suction. In GPPO, the loss function backpropagates through both the policy and environment dynamics via an analytical gradient term (see supplementary information for details). GPPO consistently outperformed PPO, reducing required training interactions by at least 45% (see Fig. 5). The second environment implements 2D Kolmogorov flow [42], a chaotic forced turbulence system characterized by extreme energy dissipation events from nonlinear energy transfer across scales. The control task is to leverage these events to enhance mixing through adaptive forcing wavenumbers. GPPO reduced training iterations by

at least 65% while producing more efficient controllers with lower action amplitudes than PPO. These results demonstrate that incorporating gradient information into the optimization process substantially improves sample efficiency and yields more efficient policies. As differentiable simulation and control methods mature, more sophisticated gradient-based approaches may deliver further gains in both efficiency and performance.

Multi-agent coordination for spatially distributed 3D cylinder control. The HydroGym benchmark platform further supports multi-agent reinforcement learning (MARL), providing environments for the 3D cylinder at $Re \in [1,000, 3,900]$. The MARL framework exploits the inherent spatial locality of flow control by decomposing the global control problem into multiple local pseudo-environments [32], each managing a pair of zero-net-mass-flow jets distributed spanwise along the cylinder surface. Unlike [32], our approach employs shared gradient updates and a unified replay buffer across all agents, enhancing computational efficiency while maintaining the cooperative learning dynamics essential for coordinated actuation. As shown in Fig. 5, this architecture enables the discovery of efficient control strategies that utilize diverse frequency bandwidths and adaptive spanwise coordination, resulting in drag reductions of approximately 8%, similar to [32]. The agents learn to manipulate the Kelvin-Helmholtz shear layer instabilities, effectively enlarging the recirculation bubble and reshaping the wake into a more aerodynamically efficient teardrop-like configuration. The cooperative control strategy attenuates Reynolds stress fluctuations while shifting peak turbulent activity downstream, resulting in reduced pressure drag through pressure recovery at the rear surface. This distributed actuation represents a paradigm shift from traditional centralized control, offering more efficient and scalable active flow control for complex 3D flows. Hence, the multi-agent paradigm offers several key advantages for flow control applications. First, it naturally scales with the number of actuators while maintaining computational tractability by exploiting local invariances in the flow. Second, it enables parallel exploration of the control space, accelerating the discovery of effective strategies compared to single-agent approaches. The shared learning architecture allows agents to benefit from collective experience while specializing in local flow dynamics, leading to more robust and generalizable control policies. Similar MARL successes in robotic swarm coordination, autonomous vehicle networks, and multi-robot manipulation demonstrate the broad applicability of this approach for distributed control.

Discussion

HydroGym addresses the fundamental bottlenecks preventing reinforcement learning from transforming fluid dynamics control: the computational intractability of training effective policies on expensive CFD simulations, and the steep domain knowledge required to implement these policies and simulations. Our platform's solver-independent architecture and comprehensive benchmark suite demonstrate that standardized environments can accelerate algorithmic development in fluid control just as ImageNet transformed computer vision and MuJoCo revolutionized robotics research. HydroGym provides an extensive suite of rigorously validated flow environments with comprehensive RL benchmarks. These environments include 2D and 3D flows across a range of geometries and Reynolds numbers, exhibiting a diversity of control challenges. Further, the HydroGym framework supports advanced RL features, such as differentiable environments, transfer learning, and multi-agent RL.

The discovered control strategies reveal reliable principles that transcend specific configurations. Agents consistently learn to exploit boundary layer manipulation, acoustic feedback disruption, and wake reorganization across diverse geometries and Reynolds numbers. These fundamental mechanisms reflect deep mathematical structures governing separated flows. This robustness suggests that reinforcement learning discovers invariant relationships in nonlinear dynamical systems, capturing physical principles that remain conserved despite significant differences in geometry or flow conditions.

However, significant challenges remain. Current sample efficiency limitations still require thousands of environment interactions, creating computational bottlenecks for the most complex turbulent scenarios. While our differentiable environments accelerate learning using gradient information, highly turbulent 3D flows still face fundamental numerical challenges in maintaining stable automatic differentiation through chaotic dynamics. It is also imperative to compare RL control with classic control strategies [43–48], providing a fair assessment of when and how to use each approach. The platform's current Reynolds number range, while useful for method development, represents a subset of industrially relevant regimes. The transfer learning capabilities highlight opportunities and limitations in generalizing flow control knowledge. Successful Reynolds number scaling suggests that control strategies capture scale-invariant physics, while geometric transfer reveals the preservation of fundamental wake manipulation principles across different boundary conditions. Yet the modest performance of zero-shot transfer indicates the need for context-dependent adaptation. Looking forward, several developments could transform the field. First, integrating HydroGym with foundation

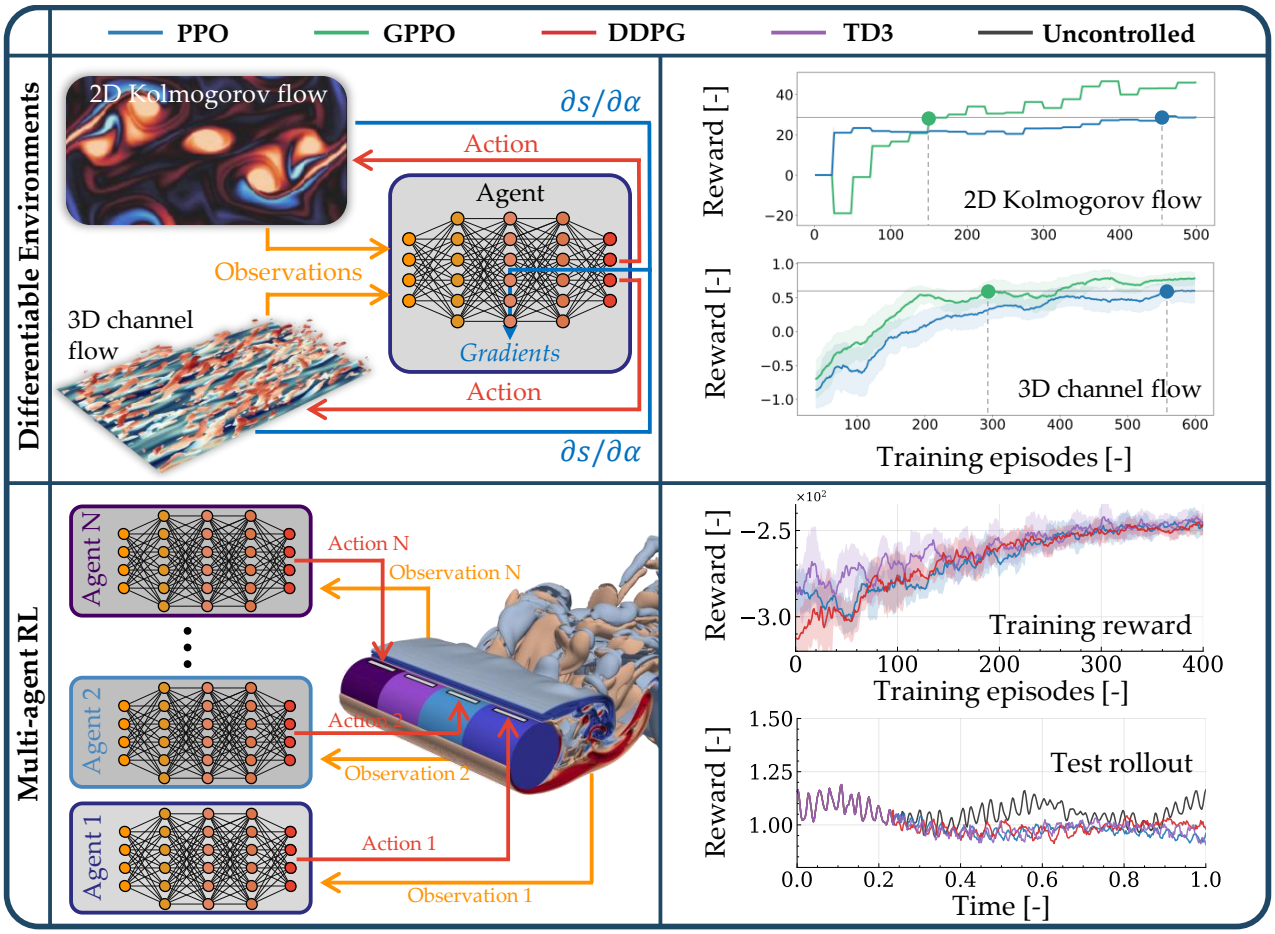

Figure 5: Advanced Reinforcement Learning. (Top) Gradient-enhanced policy optimization through differentiable environments substantially improves sample efficiency and the overall reward compared to gradient-free methods. JAX-based solvers enable automatic differentiation through complete simulation trajectories, providing exact policy gradients ($\partial s/\partial \alpha$). Training curves compare gradient-enhanced PPO (GPPO) against standard PPO for 2D Kolmogorov flow and 3D channel flow. (Bottom) Multi-agent reinforcement learning for spatially distributed control. Architecture decomposes a 3D cylinder environment at $Re = 3,900$ into multiple cooperative agents, each managing local actuator pairs while sharing gradient information and experience buffers. This distributed approach scales efficiently with actuator count and enables parallel exploration of high-dimensional control spaces. Training performance and test rollouts demonstrate effective learning and substantial drag reduction through coordinated spanwise actuation.

models trained on extensive fluid dynamics datasets spanning experimental measurements and high-fidelity simulations could dramatically improve control development. Such models may enable zero-shot transfer to entirely new flows based on learned physical principles rather than configuration-specific training. Second, advancing differentiable physics capabilities to handle fully turbulent flows would dramatically improve sample efficiency and enable gradient-based optimization at scales currently inaccessible [49–51]. Third, surrogate modeling presents a promising avenue for enhancing sample efficiency while reducing computational resources [52–55]. A hybrid approach could leverage fast surrogate models, trained on limited high-fidelity simulations, to generate the majority of training interactions, while the agent is periodically fine-tuned on a curated real-world replay buffer [17]. This would enable extensive policy exploration at minimal computational cost, reserving expensive simulations for refinement and validation. Gaussian process regression, sparse nonlinear models, neural operators, or physics-informed neural networks could serve as surrogates, providing uncertainty estimates to guide strategic high-fidelity sampling. Fourth, incorporating causal learning could enhance policy robustness and interpretability [56]. By explicitly discovering and respecting causal relationships within fluids, such as the mechanistic connections between actuator inputs, vortex dynamics, and downstream pressure gradients, agents could develop policies that gener-

alize better across operating conditions [57–60]. Causal discovery algorithms could identify invariant physical mechanisms, enabling the learned policies to maintain performance under distribution shifts [61]. Moreover, this causal perspective would transform black-box controllers into physically interpretable cause-effect chains, providing scientific insights about flow physics, validating discovered control strategies against established fluid principles, and ensuring that policies exploit genuine physical mechanisms rather than artifacts of the training environment. Fifth, the multi-agent RL success suggests a pathway toward truly scalable 3D flow control. Future developments could incorporate hierarchical architectures that learn control strategies across multiple spatial and temporal scales, from local boundary layer manipulation to global circulation control. Finally, expanding HydroGym's environments will broaden its applicability across domains. This includes developing environments for combustion in hydrogen burners, shape optimization with complex geometric constraints, aero-acoustic scenarios, multi-phase flows involving bubble dynamics, and biomedical applications ranging from nasal cavity airflow to comprehensive lung ventilation models. These specialized environments will enable targeted research into domain-specific control challenges while maintaining the framework's unified approach to reinforcement learning for fluids.

The broader implications extend beyond fluids. The demonstrated robustness of control principles suggests that deep reinforcement learning may uncover mathematical invariants governing diverse complex systems, from plasma confinement to climate dynamics. This capability to discover transferable knowledge across physical domains represents a fundamental shift from domain-specific engineering toward principled control of complex systems. Ultimately, HydroGym provides the foundation for transformative progress in flow control by democratizing access to sophisticated research tools and establishing standardized benchmarks for systematic development. Just as platform standardization catalyzed breakthroughs in protein folding and plasma control, we anticipate that HydroGym will enable the fluid dynamics community to achieve similar transformative advances across applications representing trillions of dollars in global economic activity, from next-generation aircraft and wind turbines to biomedical devices and industrial processes.

Code Availability

The HydroGym platform is publicly available at `https://cl126162.github.io/TheHydroGymProject/`. Pre-built docker containers are provided at `https://hub.docker.com/r/lpaehler/hydrogym-devpod`.

Acknowledgments

The authors acknowledge support from the the Boeing Company and the National Science Foundation AI Institute in Dynamic Systems grant number 2112085 (CL, SM, SA, EL, SLB). SLB acknowledges support from the Army Research Office (W911NF-19-1-0045) and the Air Force Office of Scientific Research (FA9550-21-1-0178). CL acknowledges support from the German Research Foundation within the Walter Benjamin fellowships LA 5508/1-1. MR acknowledges support from the German Research Foundation within the Walter Benjamin fellowship RU 2771/1-1. The authors gratefully acknowledge the Gauss Centre for Supercomputing e.V. for funding this project by providing computing time on the GCS Supercomputers.

References

[1] I. Marusic, D. Chandran, A. Rouhi, M. K. Fu, D. Wine, B. Holloway, D. Chung, and A. J. Smits. An energy-efficient pathway to turbulent drag reduction. *Nat. Comm.*, 12(1):5805, 2021.

[2] E. Mäteling, M. Albers, and W. Schröder. How spanwise travelling transversal surface waves change the near-wall flow. *J. Fluid Mech.*, 957:A30, 2023.

[3] Pierre Ricco, Martin Skote, and Michael A Leschziner. A review of turbulent skin-friction drag reduction by near-wall transverse forcing. *Prog. Aerosp. Sci.*, 123:100713, 2021.

[4] B. Font, F. Alcántara-Ávila, J. Rabault, R. Vinuesa, and O. Lehmkuhl. Deep reinforcement learning for active flow control in a turbulent separation bubble. *Nat. Comm.*, 16(1):1422, 2025.

[5] Huan Zhao, Junhua Zhao, Jing Qiu, Gaoqi Liang, and Zhao Yang Dong. Cooperative wind farm control with deep reinforcement learning and knowledge-assisted learning. *IEEE Transactions on Industrial Informatics*, 16(11):6912–6921, 2020.

[6] N. Dalili, A. Edrisy, and R. Carriveau. A review of surface engineering issues critical to wind turbine performance. *Renew. Sustain. Energy Rev*, 13(2), 2009.

[7] L. P Chamorro, REA Arndt, and Fotis Sotiropoulos. Drag reduction of large wind turbine blades through riblets: Evaluation of riblet geometry and application strategies. *Renewable Energy*, 50:1095–1105, 2013.

[8] Han Gao, S. Kaltenbach, and P. Koumoutsakos. Generative learning for forecasting the dynamics of high-dimensional complex systems. *Nat. Comm.*, 15(1):8904, 2024.

[9] S.L Brunton and B. R Noack. Closed-loop turbulence control: progress and challenges. *Appl. Mech. Rev.*, 67(5):050801, 2015.

[10] S.L. Brunton, B. R. Noack, and P. Koumoutsakos. Machine learning for fluid mechanics. *Ann. Rev. Fluid Mech.*, 52:477–508, 2020.

[11] P. Koumoutsakos. On roads less travelled between ai and computational science. *Nature Reviews Physics*, 6(6):342–344, 2024.

[12] J. Jumper, R. Evans, A. Pritzel, T. Green, M. Figurnov, O. Ronneberger, K. Tunyasuvunakool, R. Bates, A. Žídek, A. Potapenko, et al. Highly accurate protein structure prediction with AlphaFold. *Nature*, 596(7873):583–589, 2021.

[13] J. Degrave, F. Felici, J. Buchli, M. Neunert, B. Tracey, F. Carpanese, T. Ewalds, R. Hafner, A. Abdolmaleki, D. de las Casas, et al. Magnetic control of tokamak plasmas through deep reinforcement learning. *Nature*, 602(7897):414–419, 2022.

[14] D. Kochkov, J. A. Smith, A. Alieva, Q. Wang, M. P. Brenner, and S. Hoyer. Machine learning–accelerated computational fluid dynamics. *Proc. Nat. Acad. Sci.*, 118(21):e2101784118, 2021.

[15] Pol Suárez, Francisco Alcántara-Ávila, J. Rabault, Arnau Miró, Bernat Font, O. Lehmkuhl, and R. Vinuesa. Flow control of three-dimensional cylinders transitioning to turbulence via multi-agent reinforcement learning. *Communications Engineering*, 4(1):113, 2025.

[16] H. J. Bae and P. Koumoutsakos. Scientific multi-agent reinforcement learning for wall-models of turbulent flows. *Nat. Comm.*, 13(1):1443, 2022.

[17] N. Zolman, C. Lagemann, U. Fasel, J. N. Kutz, and S. L. Brunton. SINDy-RL: Interpretable and efficient model-based reinforcement learning. *arXiv preprint arXiv:2403.09110*, 2024.

[18] O. Vinyals, I. Babuschkin, W. M. Czarnecki, M. Mathieu, A. Dudzik, J. Chung, D. H. Choi, R. Powell, T. Ewalds, T. Georgiev, et al. Grandmaster level in starcraft ii using multi-agent reinforcement learning. *Nature*, 575(7782):350–354, 2019.

[19] M. Chatzimanolakis, P. Weber, and P. Koumoutsakos. Learning in two dimensions and controlling in three: Generalizable drag reduction strategies for flows past circular cylinders through deep reinforcement learning. *Phys. Rev. Fluids*, 9(4):043902, 2024.

[20] D. Fan, L. Yang, Z. Wang, M. S. Triantafyllou, and G. E. Karniadakis. Reinforcement learning for bluff body active flow control in experiments and simulations. *Proc. Nat. Acad. Sci.*, 117(42), 2020.

[21] S. Bhola, S. Pawar, P. Balaprakash, and R. Maulik. Multi-fidelity reinforcement learning framework for shape optimization. *J. Comp. Phys.*, 482:112018, 2023.

[22] Jia Deng, Wei Dong, Richard Socher, Li-Jia Li, Kai Li, and Li Fei-Fei. Imagenet: A large-scale hierarchical image database. In *2009 IEEE Conference on Computer Vision and Pattern Recognition*, pages 248–255, 2009.

[23] E. Todorov, T. Erez, and Y. Tassa. Mujoco: A physics engine for model-based control. In *2012 IEEE/RSJ Int. Conf. Intell. Robots & Sys.*, pages 5026–5033, 2012.

[24] Institute of Aerodynamics. m-AIA, 2024. https://doi.org/10.5281/zenodo.13350586.

[25] J. Bradbury, R. Frostig, P. Hawkins, M. J. Johnson, C. Leary, D. Maclaurin, G. Necula, A. Paszke, J. VanderPlas, S. Wanderman-Milne, and Q. Zhang. JAX: composable transformations of Python+NumPy programs, 2018.

[26] David A. Ham, Paul H. J. Kelly, Lawrence Mitchell, Colin J. Cotter, Robert C. Kirby, Koki Sagiyama, Nacime Bouziani, Sophia Vorderwuelbecke, Thomas J. Gregory, Jack Betteridge, Daniel R. Shapero, Reuben W. Nixon-Hill, Connor J. Ward, Patrick E. Farrell, Pablo D. Brubeck, India Marsden, Thomas H. Gibson, Miklós Homolya, Tianjiao Sun, Andrew T. T. McRae, Fabio Luporini, Alastair Gregory, Michael Lange, Simon W. Funke, Florian Rathgeber, Gheorghe-Teodor Bercea, and Graham R. Markall. *Firedrake User Manual*. Imperial College London and University of Oxford and Baylor University and University of Washington, first edition edition, 5 2023.

[27] Mark Towers, Ariel Kwiatkowski, Jordan Terry, John U Balis, Gianluca De Cola, Tristan Deleu, Manuel Goulão, Andreas Kallinteris, Markus Krimmel, Arjun KG, et al. Gymnasium: A standard interface for reinforcement learning environments. *arXiv preprint arXiv:2407.17032*, 2024.

[28] Russ Tedrake and the Drake Development Team. Drake: Model-based design and verification for robotics, 2019.

[29] Viktor Makoviychuk, Lukasz Wawrzyniak, Yunrong Guo, Michelle Lu, Kier Storey, M. Macklin, D. Hoeller, Nikita Rudin, Arthur Allshire, Ankur

Handa, et al. Isaac gym: High performance gpu-based physics simulation for robot learning. *arXiv preprint arXiv:2108.10470*, 2021.

[30] M. Mittal, C. Yu, Q. Yu, J. Liu, N. Rudin, D. Hoeller, J. L. Yuan, R. Singh, Y. Guo, H. Mazhar, A. Mandlekar, B. Babich, G. State, M. Hutter, and A. Garg. Orbit: A unified simulation framework for interactive robot learning environments. *IEEE Robotics and Automation Letters*, 8(6):3740–3747, 2023.

[31] S. Son, L. Zheng, R. Sullivan, Y.-L. Qiao, and M. Lin. Gradient informed proximal policy optimization. *Advances in Neural Information Processing Systems*, 36:8788–8814, 2023.

[32] P. Suárez, F. Alcántara-Ávila, A. Miró, J. Rabault, B. Font, O. Lehmkuhl, and R. Vinuesa. Active Flow Control for Drag Reduction Through Multi-agent Reinforcement Learning on a Turbulent Cylinder at $Re_D = 3900$. *Flow, Turb. & Combust.*, 2025.

[33] J. Schulman, F. Wolski, P. Dhariwal, A. Radford, and O. Klimov. Proximal policy optimization algorithms. *arXiv preprint arXiv:1707.06347*, 2017.

[34] T. P Lillicrap, J. J. Hunt, A. Pritzel, N. Heess, T. Erez, Y. Tassa, D. Silver, and D. Wierstra. Continuous control with deep reinforcement learning. *arXiv preprint arXiv:1509.02971*, 2015.

[35] Scott Fujimoto, Herke Hoof, and D. Meger. Addressing function approximation error in actor-critic methods. *Proceedings of the 35th International Conference on Machine Learning*, pages 1587–1596, 2018.

[36] Albert Bou, Matteo Bettini, S. Dittert, Vikash Kumar, Shagun Sodhani, Xiaomeng Yang, Gianni De Fabritiis, and Vincent Moens. TorchRL: A data-driven decision-making library for PyTorch, 2023.

[37] S. Huang, R. F. J. Dossa, C. Ye, J. Braga, D. Chakraborty, K. Mehta, and J. G. M. Araújo. CleanRL: High-quality Single-file Implementations of Deep Reinforcement Learning Algorithms. *Journal of Machine Learning Research*, 23(274):1–18, 2022.

[38] S. Son, L. Zheng, R. Sullivan, Y.-L. Qiao, and M. Lin. Gradient informed proximal policy optimization. *Advances in Neural Information Processing Systems*, 36:8788–8814, 2023.

[39] J. Xu, V. Makoviychuk, Y. Narang, F. Ramos, W. Matusik, A. Garg, and M. Macklin. Accelerated policy learning with parallel differentiable simulation. *arXiv preprint arXiv:2204.07137*, 2022.

[40] Robert D Moser, John Kim, Nagi N Mansour, et al. Direct numerical simulation of turbulent channel flow up to re= 590. *Phys. fluids*, 11(4):943–945, 1999.

[41] V. T. Hoang, A. Jafari, B. Cazzolato, and M. Arjomandi. Modification of burst events in the near-wall region of turbulent boundary layers by synthetic jets. *Int. J. Heat & Fluid Flow*, 112:109728, 2025.

[42] A. Blanchard and T. P. Sapsis. Stabilization of unsteady flows by reduced-order control with optimally time-dependent modes. *Phys. Rev. Fluids*, 4:053902, 2019.

[43] C. W Rowley, D. R Williams, T. Colonius, R. M. Murray, and D. G. Macmynowski. Linear models for control of cavity flow oscillations. *J. Fluid Mech.*, 547:317–330, 2006.

[44] Louis N Cattafesta III, Qi Song, D. R Williams, C. W Rowley, and Farrukh S Alvi. Active control of flow-induced cavity oscillations. *Prog. Aerosp. Sci.*, 44(7):479–502, 2008.

[45] S. Bagheri, J. Hoepffner, P. J. Schmid, and D. S. Henningson. Input-output analysis and control design applied to a linear model of spatially developing flows. *Appl. Mech. Rev.*, 62(2), 2009.

[46] T. Colonius and D. R. Williams. Control of vortex shedding on two-and three-dimensional aerofoils. *Phil. Trans. Roy. Soc. A*, 369(1940):1525–1539, 2011.

[47] D. Sipp and P. J. Schmid. Linear closed-loop control of fluid instabilities and noise-induced perturbations: A review of approaches and tools. *Appl. Mech. Rev.*, 68(2), 2016.

[48] C. A. Yeh and K. Taira. Resolvent-analysis-based design of airfoil separation control. *J. Fluid Mech.*, 867:572–610, 2019.

[49] B. List, L.-W. Chen, K. Bali, and N. Thuerey. Differentiability in unrolled training of neural physics simulators on transient dynamics. *Comp. Meth. Appl. Mech. Eng.*, 433:117441, 2025.

[50] F. Koehler, S. Niedermayr, N. Thuerey, et al. Apebench: A benchmark for autoregressive neural emulators of pdes. *Advances in Neural Information Processing Systems*, 37, 2024.

[51] Philipp Holl, Vladlen Koltun, and Nils Thuerey. Learning to control pdes with differentiable physics. *arXiv preprint arXiv:2001.07457*, 2020.

[52] R. Maulik, K. Fukami, N. Ramachandra, K. Fukagata, and K. Taira. Probabilistic neural networks

for fluid flow surrogate modeling and data recovery. *Phys. Rev. Fluids*, 5(10):104401, 2020.

[53] K. Duraisamy, G. Iaccarino, and H. Xiao. Turbulence modeling in the age of data. *Ann. Rev. Fluid Mech.*, 51:357–377, 2019.

[54] Q. Liu, Y. Sun, C.-A. Yeh, L. S. Ukeiley, L. N. Cattafesta III, and K. Taira. Unsteady control of supersonic turbulent cavity flow based on resolvent analysis. *J. Fluid Mech.*, 925:A5, 2021.

[55] Onofrio Semeraro, Shervin Bagheri, L. Brandt, and Dan S Henningson. Feedback control of three-dimensional optimal disturbances using reduced-order models. *J. Fluid Mech.*, 677:63–102, 2011.

[56] Miguel Beneitez, Andres Cremades, Luca Guastoni, and Ricardo Vinuesa. Improving turbulence control through explainable deep learning. *arXiv preprint arXiv:2504.02354*, 2025.

[57] A. Cremades, S. Hoyas, R. Deshpande, P. Quintero, Martin Lellep, Will Junghoon Lee, J. P. Monty, N. Hutchins, M. Linkmann, I. Marusic, et al. Identifying regions of importance in wall-bounded turbulence through explainable deep learning. *Nat. Comm.*, 15(1):3864, 2024.

[58] A. Lozano-Durán and H. J. Bae. Machine learning building-block-flow wall model for large-eddy simulation. *J. Fluid Mech.*, 963:A35, 2023.

[59] Á. Martínez-Sánchez, G. Arranz, and A. Lozano-Durán. Decomposing causality into its synergistic, unique, and redundant components. *Nat. Comm.*, 15(1), 2024.

[60] Kai Lagemann, C. Lagemann, B. Taschler, and Sach Mukherjee. Deep learning of causal structures in high dimensions under data limitations. *Nature Machine Intelligence*, 5(11):1306–1316, 2023.

[61] M. Cranmer, Alvaro Sanchez-Gonzalez, Rui Battaglia, P.and Xu, Kyle Cranmer, D. Spergel, and Shirley Ho. Discovering symbolic models from deep learning with inductive biases. *Advances in Neural Information Processing Systems*, 33:17429–17442, 2020.

[62] S. L. Brunton and B. R. Noack. Closed-loop turbulence control: Progress and challenges. *Appl. Mech. Rev.*, 67:050801–1–050801–48, 2015.

[63] S. L. Brunton, B. R. Noack, and P. Koumoutsakos. Machine learning for fluid mechanics. *Ann. Rev. Fluid Mech.*, 52:477–508, 2020.

[64] Greg Brockman, Vicki Cheung, Ludwig Pettersson, Jonas Schneider, John Schulman, Jie Tang, and Wojciech Zaremba. Openai gym. *arXiv preprint arXiv:1606.01540*, 2016.

[65] R. Vinuesa and S. L. Brunton. Enhancing computational fluid dynamics with machine learning. *Nature Computational Science*, 2(6):358–366, 2022.

[66] Eliot Xing, Vernon Luk, and Jean Oh. Stabilizing reinforcement learning in differentiable multiphysics simulation. *arXiv preprint arXiv:2412.12089*, 2024.

[67] Rishabh Puri, Junya Onishi, Mario Rüttgers, Rakesh Sarma, Makoto Tsubokura, and Andreas Lintermann. On the choice of physical constraints in artificial neural networks for predicting flow fields. *Future Generation Computer Systems*, 161:361–375, 2024.

[68] Mario Rüttgers, Junshin Park, and Donghyun You. Large-eddy simulation of turbulent flow over the drivaer fastback vehicle model. *Journal of Wind Engineering and Industrial Aerodynamics*, 186:123–138, 2019.

[69] E. Lagemann, S.L Brunton, W. Schröder, and C. Lagemann. Towards extending the aircraft flight envelope by mitigating transonic airfoil buffet. *Nat. Comm.*, 15(1):5020, 2024.

[70] Esther Lagemann, Marian Albers, Christian Lagemann, and Wolfgang Schröder. Impact of reynolds number on the drag reduction mechanism of spanwise travelling surface waves. *Flow, Turbulence and Combustion*, 113(1):27–40, 2024.

[71] J. Rabault, M. Kuchta, A. Jensen, U. Réglade, and N. Cerardi. Artificial neural networks trained through deep reinforcement learning discover control strategies for active flow control. *J. Fluid Mech.*, 865:281–302, 2019.

[72] Mikhail Tokarev, Egor Palkin, and Rustam Mullyadzhanov. Deep reinforcement learning control of cylinder flow using rotary oscillations at low reynolds number. *Energies*, 13(22):5920, 2020.

[73] Hui Xu, Wei Zhang, Jian Deng, and J. Rabault. Active flow control with rotating cylinders by an artificial neural network trained by deep reinforcement learning. *Journal of Hydrodynamics*, 32(2):254–258, 2020.

[74] J. Rabault and Alexander Kuhnle. Accelerating deep reinforcement learning strategies of flow control through a multi-environment approach. *Physics of Fluids*, 31(9), 2019.

[75] Qiulei Wang, Lei Yan, Gang Hu, Wenli Chen, J. Rabault, and B. R Noack. Dynamic feature-based deep reinforcement learning for flow control of circular cylinder with sparse surface pressure sensing. *J. Fluid Mech.*, 988:A4, 2024.

[76] Wenjie Chen, Qiulei Wang, Lei Yan, Gang Hu, and B. R Noack. Deep reinforcement learning-based active flow control of vortex-induced vibration of a square cylinder. *Physics of Fluids*, 35(5), 2023.

[77] Lei Yan, Yuerong Li, Gang Hu, Wen-li Chen, Wei Zhong, and B. R Noack. Stabilizing the square cylinder wake using deep reinforcement learning for different jet locations. *Physics of Fluids*, 35(11), 2023.

[78] Mustafa Z Yousif, Paraskovia Kolesova, Yifan Yang, Meng Zhang, Linqi Yu, J. Rabault, R. Vinuesa, and Hee-Chang Lim. Optimizing flow control with deep reinforcement learning: Plasma actuator placement around a square cylinder. *Physics of Fluids*, 35(12), 2023.

[79] Lei Yan, Gang Hu, Wenli Chen, and B. R Noack. Deep reinforcement transfer learning for active flow control of a 3D square cylinder under state dimension mismatch. *arXiv preprint arXiv:2401.12543*, 2024.

[80] Chengwei Xia, Junjie Zhang, Eric C Kerrigan, and Georgios Rigas. Active flow control for bluff body drag reduction using reinforcement learning with partial measurements. *Journal of Fluid Mechanics*, 981:A17, 2024.

[81] Wang Jia and Hang Xu. Robust and adaptive deep reinforcement learning for enhancing flow control around a square cylinder with varying reynolds numbers. *Physics of Fluids*, 36(5), 2024.

[82] Jonathan Viquerat, J. Rabault, Alexander Kuhnle, Hassan Ghraieb, Aurélien Larcher, and Elie Hachem. Direct shape optimization through deep reinforcement learning. *J. Comp. Phys.*, 428:110080, 2021.

[83] M. Rüttgers, M. Waldmann, W. Schröder, and A. Lintermann. Machine learning-based control of perturbed and heated channel flows. In *High Performance Computing*, pages 7–22, 2021.

[84] Jinhua Lou, Rongqian Chen, Jiaqi Liu, Yue Bao, Yancheng You, and Zhengwu Chen. Aerodynamic optimization of airfoil based on deep reinforcement learning. *Physics of Fluids*, 35(3), 2023.

[85] Thomas P Dussauge, Woong Je Sung, Olivia J Pinon Fischer, and Dimitri N Mavris. A reinforcement learning approach to airfoil shape optimization. *Scientific Reports*, 13(1):9753, 2023.

[86] Jignesh Patel, Yannis Spyridis, and Vasileios Argyriou. Enhancing vehicle aerodynamics with deep reinforcement learning in voxelised models. In *2024 14th International Conference on Pattern Recognition Systems (ICPRS)*, pages 1–7. IEEE, 2024.

[87] Jonathan Tran, Kai Fukami, Kenta Inada, Daisuke Umehara, Yoshimichi Ono, Kenta Ogawa, and Kunihiko Taira. Aerodynamics-guided machine learning for design optimization of electric vehicles. *Communications Engineering*, 3(1):174, 2024.

[88] Sang-Jae Yeo, Suk-Yoon Hong, and Jee-Hun Song. Deep-reinforcement-learning-based hull form optimization method for stealth submarine design. *International Journal of Naval Architecture and Ocean Engineering*, 16:100595, 2024.

[89] S.-J. Oh, M.-J. Oh, and E.-Y. Son. Reinforcement learning-based optimal hull form design with variations in fore and aft parts. *J. Comp. Design Eng.*, 11(6):1–19, 2024.

[90] J. Xiang, H. Zong, Y. Wu, J. Li, and H. Liang. Experimental control of the flow separation behind a backward facing step using deep reinforcement learning. *Physics of Fluids*, 36(10), 2024.

[91] Satoshi Shimomura, Satoshi Sekimoto, Akira Oyama, Kozo Fujii, and Hiroyuki Nishida. Closed-loop flow separation control using the deep Q network over airfoil. *AIAA Journal*, 58(10):4260–4270, 2020.

[92] X. Garcia, A. Miró, P. Suárez, F. Alcántara-Ávila, J. Rabault, B. Font, O. Lehmkuhl, and R. Vinuesa. Deep-reinforcement-learning-based separation control in a two-dimensional airfoil. *Int. J. Heat & Fluid Flow*, 116:109913, 2025.

[93] L. Guastoni, J. Rabault, Philipp Schlatter, Hossein Azizpour, and R. Vinuesa. Deep reinforcement learning for turbulent drag reduction in channel flows. *The European Physical Journal E*, 46(4):27, 2023.

[94] Taehyuk Lee, Junhyuk Kim, and Changhoon Lee. Turbulence control for drag reduction through deep reinforcement learning. *Phys. Rev. Fluids*, 8(2):024604, 2023.

[95] Zisong Zhou, Mengqi Zhang, and Xiaojue Zhu. Reinforcement-learning-based control of turbulent channel flows at high Reynolds numbers. *J. Fluid Mech.*, 1006:A12, 2025.

[96] Takahiro Sonoda, Zhuchen Liu, Toshitaka Itoh, and Yosuke Hasegawa. Reinforcement learning of control strategies for reducing skin friction drag in a

fully developed turbulent channel flow. *J. Fluid Mech.*, 960:A30, 2023.

[97] G. Novati, S. Verma, D. Alexeev, D. Rossinelli, W. M. Van Rees, and P. Koumoutsakos. Synchronisation through learning for two self-propelled swimmers. *Bioinspiration & biomimetics*, 12(3):036001, 2017.

[98] S. Verma, G. Novati, and P. Koumoutsakos. Efficient collective swimming by harnessing vortices through deep reinforcement learning. *Proc. Nat. Acad. Sci.*, 115(23):5849–5854, 2018.

[99] Ke Qin, Zonghao Zou, Lailai Zhu, and On Shun Pak. Reinforcement learning of a multi-link swimmer at low Reynolds numbers. *Physics of Fluids*, 35(3), 2023.

[100] Tongzhao Xiong, Zhaorong Liu, Yufei Wang, Chong Jin Ong, and Lailai Zhu. Chemotactic navigation in robotic swimmers via reset-free hierarchical reinforcement learning. *Nat. Comm.*, 16(1):5441, 2025.

[101] Yi Zhu, Jian-Hua Pang, Tong Gao, and Fang-Bao Tian. Learning to school in dense configurations with multi-agent deep reinforcement learning. *Bioinspiration & Biomimetics*, 18(1):015003, 2022.

[102] Daniel Wälchli, Pascal Weber, Michail Chatzimanolakis, Robert Katzschmann, and P. Koumoutsakos. Inverse reinforcement learning for objective discovery in collective behavior of artificial swimmers. *Phys. Rev. Fluids*, 10(6):064901, 2025.

[103] M. Rüttgers, M. Waldmann, K. Vogt, J. Ilgner, W. Schröder, and A. Lintermann. Automated surgery planning for an obstructed nose by combining computational fluid dynamics with reinforcement learning. *Computers in Biology and Medicine*, 173:108383, 2024.

[104] M. Rüttgers, F. Hübenthal, M. Tsubokura, and A. Lintermann. Parallel Reinforcement Learning and Gaussian Process Regression for Improved Physics-Based Nasal Surgery Planning. In *Parallel Processing and Applied Mathematics*, pages 79–96. Springer Nature Switzerland, 2025.

[105] Parisa Sarikhani, Hao-Lun Hsu, Mahmoud Zeydabadinezhad, Yuyu Yao, Mayuresh Kothare, and Babak Mahmoudi. Reinforcement learning for closed-loop regulation of cardiovascular system with vagus nerve stimulation: a computational study. *Journal of Neural Engineering*, 21, 06 2024.

[106] Yuyang Shi, Zhike Xu, Chenghan Chen, Feng He, Pengfei Hao, and Xiwen Zhang. Enhancing cardiac hemodynamic and pulsatility in heart failure via deep reinforcement learning: An in-silico and in-vitro validation study of percutaneous ventricular assist devices. *Computer Methods and Programs in Biomedicine*, 270:108975, 2025.

[107] E. Hachem, P. Meliga, A. Goetz, P. Rico, J. Viquerat, A. Larcher, R. Valette, A. Sanches, V. Lannelongue, H. Ghraieb, R. Nemer, Y. Ozpeynirci, and T. Liebig. Reinforcement learning for patient-specific optimal stenting of intracranial aneurysms. *Scientific Reports*, 13:7147, 05 2023.

[108] J. Yang, T. Dzanic, B. Petersen, J. Kudo, K. Mittal, V. Tomov, J.-S. Camier, T. Zhao, H. Zha, T. Kolev, et al. Reinforcement learning for adaptive mesh refinement. In *International conference on artificial intelligence and statistics*, pages 5997–6014. PMLR, 2023.

[109] Corbin Foucart, Aaron Charous, and Pierre FJ Lermusiaux. Deep reinforcement learning for adaptive mesh refinement. *J. Comp. Phys.*, 491:112381, 2023.

[110] Y. Zhu, S. Zhao, Y. Zhou, H. Liang, and X. Bian. An unstructured adaptive mesh refinement for steady flows based on physics-informed neural networks. *J. Comp. Phys.*, page 114283, 2025.

[111] D. Huergo, Gonzalo Rubio, and Esteban Ferrer. A reinforcement learning strategy for p-adaptation in high order solvers. *Results in Engineering*, 21:101693, 2024.

[112] Karthik Duraisamy, Gianluca Iaccarino, and Heng Xiao. Turbulence modeling in the age of data. *Ann. Rev. Fluid Mech.*, 51(1):357–377, 2019.

[113] Marius Kurz, Philipp Offenhäuser, and A. Beck. Deep reinforcement learning for turbulence modeling in large eddy simulations. *Int. J. Heat & Fluid Flow*, 99:109094, 2023.

[114] G. Novati, H. L. de Laroussilhe, and P. Koumoutsakos. Automating turbulence modelling by multi-agent reinforcement learning. *Nat. Mach. Intell.*, 3(1):87–96, 2021.

[115] Zhan Zhang. Application of deep reinforcement learning in parameter optimization and refinement of turbulence models. *Scientific Reports*, 15(1):25236, 2025.

[116] D. Zhou and H. J. Bae. Wall modeling of turbulent flows with varying pressure gradients using multi-agent reinforcement learning. *AIAA Journal*, 62(10):3713–3727, 2024.

[117] Wulong Hu, Zhangze Jiang, Mingyang Xu, and Hanyu Hu. Efficient deep reinforcement learning strategies for active flow control based on physics-informed neural networks. *Physics of Fluids*, 36(7), 2024.

[118] Colin Rodwell and Phanindra Tallapragada. Physics-informed reinforcement learning for motion control of a fish-like swimming robot. *Scientific Reports*, 13(1):10754, 2023.

[119] Minghui Ye and Ahmed H Elsheikh. Model-based reinforcement learning for active flow control. *Physics of Fluids*, 37(9), 2025.

[120] Andre Weiner and Janis Geise. Model-based deep reinforcement learning for accelerated learning from flow simulations. *Meccanica*, 60(6):1771–1788, 2025.

[121] P. L. Bhatnagar, E. P. Gross, and M. Krook. A model for collision processes in gases. I. Small amplitude processes in charged and neutral one-component systems. *Physical Review*, 94(3):511, 1954.

[122] Martin Geier, Martin Schönherr, A. Pasquali, and Manfred Krafczyk. The cumulant lattice boltzmann equation in three dimensions: Theory and validation. *Computers & Mathematics with Applications*, 70(4):507–547, 2015.

[123] Andreas Lintermann, Matthias Meinke, and Wolfgang Schröder. Fluid mechanics based classification of the respiratory efficiency of several nasal cavities. *Computers in Biology and Medicine*, 43(11):1833–1852, 2013.

[124] M. Rüttgers, M. Waldmann, W. Schröder, and A. Lintermann. A machine-learning-based method for automatizing lattice-boltzmann simulations of respiratory flows. *Applied Intelligence*, 52:9080–9100, 2022.

[125] Alexandre Dupuis and Bastien Chopard. Theory and applications of an alternative lattice boltzmann grid refinement algorithm. *Physical Review E*, 67(6):066707, 2003.

[126] Mohamed Bouzidi, Mouaouia Firdaouss, and Pierre Lallemand. Momentum transfer of a boltzmann-lattice fluid with boundaries. *Physics of Fluids*, 13(11):3452–3459, 2001.

[127] C. Lagemann, M. Rüttgers, M. Gondrum, M. Meinke, W. Schröder, A. Lintermann, and S.L. Brunton. HydroGym-GPU: From 2D to 3D Benchmark Environments for Reinforcement Learning in Fluid Flows. In *Proc. 35th Int. Conf. on Parallel Comp. Fluid Dyn.*, 2024.

[128] Sajeda Mokbel, C. Lagemann, E. Lagemann, and S. L. Brunton. Controlling chaotic energy events in fluids with reinforcement learning. In *Proceedings of the 16th ACM International Conference on Future and Sustainable Energy Systems*, pages 954–958, 2025.

[129] Robert Tjarko Lange. gymnax: A JAX-based Reinforcement Learning Environment Library, 2022.

[130] Chris Lu. PureJaxRL: End-to-End RL Training in Pure Jax, 2023.

[131] James Bradbury, Roy Frostig, M. James Hawkins, P.and Johnson, Chris Leary, Dougal Maclaurin, George Necula, Adam Paszke, Jake VanderPlas, Skye Wanderman-Milne, and Qiao Zhang. JAX: composable transformations of Python+NumPy programs, 2018.

[132] J. Schulman, P. Moritz, S. Levine, M. Jordan, and P. Abbeel. High-dimensional continuous control using generalized advantage estimation. *arXiv preprint arXiv:1506.02438*, 2015.

[133] Volodymyr Mnih, Koray Kavukcuoglu, D. Silver, et al. Human-level control through deep reinforcement learning. *Nature*, 518(7540):529–533, 2015.

[134] D. Silver, Guy Lever, Nicolas Heess, Thomas Degris, Daan Wierstra, and Martin Riedmiller. Deterministic policy gradient algorithms. In *Proceedings of the 31st International Conference on Machine Learning*, pages 387–395, 2014.

[135] George E Uhlenbeck and L. S Ornstein. On the theory of the Brownian motion. *Physical Review*, 36(5):823–841, 1930.

[136] Sergey Ioffe and C. Szegedy. Batch normalization: Accelerating deep network training by reducing internal covariate shift. In *Proceedings of the 32nd International Conference on Machine Learning*, pages 448–456, 2015.

[137] H. van Hasselt. Double Q-learning. *Advances in Neural Information Processing Systems*, 23:2613–2621, 2010.

[138] Ronald J Williams. Simple statistical gradient-following algorithms for connectionist reinforcement learning. *Machine learning*, 8(3-4):229–256, 1992.

[139] A. Griewank and A. Walther. *Evaluating derivatives: principles and techniques of algorithmic differentiation*, volume 105. SIAM, 2008.

[140] Jonathan Heek, Anselm Levskaya, Avital Oliver, Marvin Ritter, Bertrand Rondepierre, A. Steiner, and Marc van Zee. Flax: A neural network library and ecosystem for JAX, 2020.

[141] C.H.K. Williamson. Vortex dynamics in the cylinder wake. *Ann. Rev. Fluid Mech.*, 28:477–539, 1996.

[142] CHK Williamson. Three-dimensional wake transition. *J. Fluid Mech.*, 328:345–407, 1996.

[143] A.I. Aleksyuk and M. Heil. On the short-wavelength three-dimensional instability in the cylinder wake. *J. Fluid Mech.*, 999, 2024.

[144] S. Bhattacharya and J.W. Gregory. Investigation of the cylinder wake under spanwise periodic forcing with a segmented plasma actuator. *Physics of Fluids*, 27(1):014102, 2015.

[145] F. Ren, L. Cheng, Q. Xiong, F. Tong, and C. Chen. Three-dimensional wake transitions of steady flow past two side-by-side cylinders. *J. Fluid Mech.*, 969, 2023.

[146] P. Parnaudeau, J. Carlier, D. Heitz, and E. Lamballais. Experimental and numerical studies of the flow over a circular cylinder at Reynolds number 3900. *Physics of Fluids*, 20:085101, 2008.

[147] Arthur G Kravchenko and P. Moin. Numerical studies of flow over a circular cylinder at $Re_D = 3900$. *Physics of Fluids*, 12(2):403–417, 2000.

[148] Bing-Zheng Han, Wei-Xi Huang, and Chun-Xiao Xu. Deep reinforcement learning for active control of flow over a circular cylinder with rotational oscillations. *Int. J. Heat & Fluid Flow*, 96:109008, 2022.

[149] S. L. Brunton and J. N. Kutz. *Data-Driven Science and Engineering: Machine Learning, Dynamical Systems, and Control*. Cambridge University Press, 2nd edition, 2022.

[150] Kai Lagemann, C. Lagemann, and Sach Mukherjee. Invariance-based learning of latent dynamics. In *The Twelfth International Conference on Learning Representations*, 2023.

[151] Julio R Meneghini, Fábio Saltara, Cesareo de La Rosa Siqueira, and JA Ferrari Jr. Numerical simulation of flow interference between two circular cylinders in tandem and side-by-side arrangements. *J. Fluid Struct.*, 15(2):327–350, 2001.

[152] H Ding, C Shu, KS Yeo, and D Xu. Numerical simulation of flows around two circular cylinders by mesh-free least square-based finite difference methods. *International journal for numerical methods in fluids*, 53(2):305–332, 2007.

[153] M Braza, PHHM Chassaing, and H Ha Minh. Numerical study and physical analysis of the pressure and velocity fields in the near wake of a circular cylinder. *J. Fluid Mech.*, 165:79–130, 1986.

[154] O Posdziech and R Grundmann. A systematic approach to the numerical calculation of fundamental quantities of the two-dimensional flow over a circular cylinder. *J. Fluid Struct.*, 23(3):479–499, 2007.

[155] A. B. Harichandan and A. Roy. Numerical investigation of low reynolds number flow past two and three circular cylinders using unstructured grid cfr scheme. *Int. J. Heat & Fluid Flow*, 31(2):154–171, 2010.

[156] A. Colagrossi, G. Graziani, and M. Pulvirenti. Particles for fluids: Sph versus vortex methods. *Mathematics and Mechanics of complex systems*, 2(1):45–70, 2013.

[157] Danilo Durante, Emanuele Rossi, A. Colagrossi, and Giorgio Graziani. Numerical simulations of the transition from laminar to chaotic behaviour of the planar vortex flow past a circular cylinder. *Communications in Nonlinear Science and Numerical Simulation*, 48:18–38, 2017.

[158] L Ridgway Scott and Rebecca Durst. Chaotic dynamics of two-dimensional flows around a cylinder. *Physics of Fluids*, 36(2), 2024.

[159] Henry von Wahl, Leo G Rebholz, and L Ridgway Scott. Benchmark stress tests for flow past a cylinder at higher reynolds numbers using emac. *arXiv preprint arXiv:2507.09274*, 2025.

[160] Lixia Qu, Christoffer Norberg, Lars Davidson, Shia-Hui Peng, and Fujun Wang. Quantitative numerical analysis of flow past a circular cylinder at Reynolds number between 50 and 200. *J. Fluid Struct.*, 39:347–370, 2013.

[161] O. Posdziech and R. Grundmann. Numerical simulation of the flow around an infinitely long circular cylinder in the transition regime. *Theor. Comp. Fluid Dyn.*, 15(2):121–141, 2001.

[162] Bruno Souza Carmo and Julio Romano Meneghini. Numerical investigation of the flow around two circular cylinders in tandem. *J. Fluid Struct.*, 22(6-7):979–988, 2006.

[163] DFL Labbé and PA Wilson. A numerical investigation of the effects of the spanwise length on the 3-D wake of a circular cylinder. *J. Fluid Struct.*, 23(8):1168–1188, 2007.

[164] Suresh Behara and Sanjay Mittal. Parallel finite element computation of incompressible flows. *Parallel Computing*, 35(4):195–212, 2009.

[165] BN Rajani, A Kandasamy, and Sekhar Majumdar. Numerical simulation of laminar flow past a circular cylinder. *Applied Mathematical Modelling*, 33(3):1228–1247, 2009.

[166] Feifei Tong, Liang Cheng, and Ming Zhao. Numerical simulations of steady flow past two cylinders in staggered arrangements. *J. Fluid Mech.*, 765:114–149, 2015.

[167] Chengwang Lei, Liang Cheng, and Ken Kavanagh. Spanwise length effects on three-dimensional modelling of flow over a circular cylinder. *Computer methods in applied mechanics and engineering*, 190(22-23):2909–2923, 2001.

[168] Ming Zhao, Liang Cheng, and Tongming Zhou. Direct numerical simulation of three-dimensional flow past a yawed circular cylinder of infinite length. *J. Fluid Struct.*, 25(5):831–847, 2009.

[169] O Lehmkuhl, I Rodríguez, R Borrell, and A Oliva. Low-frequency unsteadiness in the vortex formation region of a circular cylinder. *Physics of Fluids*, 25(8), 2013.

[170] F Tremblay, M Manhart, and R Friedrich. LES of flow around a circular cylinder at a subcritical Reynolds number with cartesian grids. In *Advances in LES of Complex Flows: Proceedings of the Euromech Colloquium 412*, pages 133–150. Springer, 2002.

[171] B. R. Noack and Marek Morzyński. The Fluidic Pinball - a Toolkit for Multiple-Input Multiple-Output Flow Control. *Technical Report 02/2016*, 2017.

[172] Nan Deng, B. R. Noack, Marek Morzyński, and Luc R Pastur. Low-order model for successive bifurcations of the fluidic pinball. *J. Fluid Mech.*, 884:A37, 2020.

[173] Luc R. Pastur, Nan Deng, Marek Morzyński, and B. R. Noack. Reduced-order modeling of the fluidic pinball. In *11th Chaotic Modeling and Simulation International Conference*, pages 205–213. Springer International Publishing, 2019.

[174] Nan Deng, Luc R Pastur, B. R. Noack, and Marek Morzyński. Galerkin force model for transient and post-transient dynamics of the fluidic pinball. *J. Fluid Mech.*, 918:A4, 2021.

[175] Xin Wang, Nan Deng, Guy Y Cornejo Maceda, and B. R Noack. Cluster-based control for net drag reduction of the fluidic pinball. *Physics of Fluids*, 35(2), 2023.

[176] D. Sipp and A. Lebedev. Global stability of base and mean flows: a general approach and its applications to cylinder and open cavity flows. *J. Fluid Mech.*, 593:333–358, 2007.

[177] Thierry M Faure, Panayotis Adrianos, Flavio Lusseyran, and Luc Pastur. Visualization of the flow inside an open cavity at medium range reynolds numbers. *Experiments in Fluids*, 42(2):169–184, 2007.

[178] A. Barbagallo, D. Sipp, and P. J. Schmid. Closed-loop control of an open cavity flow using reduced-order models. *J. Fluid Mech.*, 641:1–50, 2009.

[179] Jesús de Vicente, Eusebio Valero, L. M González, and Vassilis Theofilis. Linear three-dimensional global and asymptotic stability analysis of incompressible open cavity flow. *J. Fluid Mech.*, 768:113–140, 2015.

[180] M. F Barone and Srinivasan Arunajatesan. A cavity depth sensitized Rossiter mode formula. *Applied Mathematics and Computation*, 340:221–226, 2018.

[181] JE Rossiter. Wind tunnel experiments on the flow over rectangular cavities at subsonic and transonic speeds. *Aeronautical Research Council Reports and Memoranda*, 1964.

[182] C. W Rowley and D. R Williams. Dynamics and Control of High-Reynolds-Number Flow over Open Cavities. *Ann. Rev. Fluid Mech.*, 38:251–276, 2006.

[183] L. N Cattafesta III, Q. Song, D. R Williams, C. W Rowley, and F. S. Alvi. Active control of flow-induced cavity oscillations. *Prog. Aerosp. Sci.*, 44(7-8):479–502, 2008.

[184] Ahmad Sohankar, Christoffer Norberg, and Lars Davidson. Simulation of three-dimensional flow around a square cylinder at moderate reynolds numbers. *Physics of Fluids*, 11(2):288–306, 1999.

[185] Honglei Bai and Md Mahbub Alam. Dependence of square cylinder wake on Reynolds number. *Physics of Fluids*, 30(1), 2018.

[186] Hongyi Jiang, Liang Cheng, and Hongwei An. Three-dimensional wake transition of a square cylinder. *J. Fluid Mech.*, 842:102–127, 2018.

[187] F. X. Trias, A. Gorobets, and A. Oliva. Turbulent flow around a square cylinder at Reynolds number

22000: A DNS study. *Computers & Fluids*, 123:87–98, 2015.

[188] Y. Srinivas, G. Biswas, A. S. Parihar, and R. Ranjan. Large-eddy simulation of high Reynolds number turbulent flow past a square cylinder. *Journal of Engineering Mechanics*, 132(3):327–336, 2006.

[189] Zihao Zhu, Pau Fradera-Soler, William Jo, and Feng Liu. Numerical simulation of the flow around a square cylinder under plasma actuator control. *Physics of Fluids*, 33(12), 2021.

[190] M. I. Yuce and D. A. Kareem. A numerical analysis of fluid flow around circular and square cylinders. *Journal - American Water Works Association*, 108(10):E546–E554, 2016.

[191] W Rodi. Comparison of LES and RANS calculations of the flow around bluff bodies. *Journal of wind engineering and industrial aerodynamics*, 69:55–75, 1997.

[192] Ahmad Sohankar, Christoffer Norberg, and Lars Davidson. Low-Reynolds-number flow around a square cylinder at incidence: study of blockage, onset of vortex shedding and outlet boundary condition. *International journal for numerical methods in fluids*, 26(1):39–56, 1998.

[193] M Cheng, DS Whyte, and J Lou. Numerical simulation of flow around a square cylinder in uniform-shear flow. *J. Fluid Struct.*, 23(2):207–226, 2007.

[194] Atsushi Okajima. Strouhal numbers of rectangular cylinders. *J. Fluid Mech.*, 123:379–398, 1982.

[195] Hongyi Jiang and Liang Cheng. Hydrodynamic characteristics of flow past a square cylinder at moderate Reynolds numbers. *Physics of Fluids*, 30(10), 2018.

[196] Christoffer Norberg. Flow around rectangular cylinders: pressure forces and wake frequencies. *Journal of wind engineering and industrial aerodynamics*, 49(1-3):187–196, 1993.

[197] Shuyang Cao, Yaojun Ge, and Yukio Tamura. Shear effects on flow past a square cylinder at moderate Reynolds numbers. *Journal of engineering mechanics*, 138(1):116–123, 2012.

[198] Dong-Hyeog Yoon, Kyung-Soo Yang, and Choon-Bum Choi. Three-dimensional wake structures and aerodynamic coefficients for flow past an inclined square cylinder. *Journal of Wind Engineering and Industrial Aerodynamics*, 101:34–42, 2012.

[199] D Mateescu and M Abdo. Analysis of flows past airfoils at very low Reynolds numbers. *Proc. Inst. Mech. Eng. G*, 224(7):757–775, 2010.

[200] Eltayeb Eljack, Julio Soria, Yasir Elawad, and Tomohisa Ohtake. Simulation and characterization of the laminar separation bubble over a NACA-0012 airfoil as a function of angle of attack. *Phys. Rev. Fluids*, 6(3):034701, 2021.

[201] Jaber AlMutairi, Eltayeb ElJack, and Ibraheem AlQadi. Dynamics of laminar separation bubble over naca-0012 airfoil near stall conditions. *Aerospace Science and Technology*, 68:193–203, 2017.

[202] Ivette Rodríguez, O. Lehmkuhl, R Borrell, and A Oliva. Direct numerical simulation of a NACA0012 in full stall. *Int. J. Heat & Fluid Flow*, 43:194–203, 2013.

[203] Hua Shan, Li Jiang, and Chaoqun Liu. Direct numerical simulation of flow separation around a NACA 0012 airfoil. *Computers & fluids*, 34(9):1096–1114, 2005.

[204] Sergio Martínez-Aranda, AL García-González, Luis Parras, JF Velázquez-Navarro, and C Del Pino. Comparison of the aerodynamic characteristics of the NACA0012 airfoil at low-to-moderate Reynolds numbers for any aspect ratio. *International Journal of Aerospace Sciences*, 4(1):1–8, 2016.

[205] Sam Zarovy, Mark Costello, Ankur Mehta, Greg Gremillion, Derek Miller, Badri Ranganathan, J Sean Humbert, and Paul Samuel. Experimental study of gust effects on micro air vehicles. In *AIAA atmospheric flight mechanics conference*, page 7818, 2010.

[206] Herbert G Küssner. Zusammenfassender Bericht über den instationären Auftrieb von Flügeln. *Luftfahrtforschung*, 13:410, 1936.

[207] Kai Fukami, Hiroya Nakao, and Kunihiko Taira. Data-driven transient lift attenuation for extreme vortex gust–airfoil interactions. *J. Fluid Mech.*, 992:A17, 2024.

[208] Kenneth Granlund, Bruno Monnier, M Ol, and D. Williams. Airfoil longitudinal gust response in separated vs. attached flows. *Physics of Fluids*, 26(2), 2014.

[209] M. Gondrum, M. Meinke, W. Schroeder, F. Avallone, and D. Ragni. Porous fairings for landing gear noise mitigation. In *30th AIAA/CEAS Aeroacoustics Conference (2024)*, page 3174, 2024.

[210] Giovanni Di Ilio, Daniele Chiappini, Stefano Ubertini, Gino Bella, and Sauro Succi. Fluid flow around NACA 0012 airfoil at low-Reynolds numbers with hybrid lattice Boltzmann method. *Computers & Fluids*, 166:200–208, 2018.

[211] Yan Liu, Kailun Li, Jiazhong Zhang, Hang Wang, and Liguang Liu. Numerical bifurcation analysis of static stall of airfoil and dynamic stall under unsteady perturbation. *Communications in Nonlinear Science and Numerical Simulation*, 17(8):3427–3434, 2012.

[212] Dilek Funda Kurtulus. On the unsteady behavior of the flow around NACA 0012 airfoil with steady external conditions at $Re = 1000$. *International journal of micro air vehicles*, 7(3):301–326, 2015.

[213] Taiba Kouser, Yongliang Xiong, Dan Yang, and Sai Peng. Direct Numerical Simulations on the three-dimensional wake transition of flows over NACA0012 airfoil at $Re = 1000$. *International Journal of Micro Air Vehicles*, 13:17568293211055656, 2021.

[214] Y. Hoarau, M. Braza, Y. Ventikos, and D. Faghani. First stages of the transition to turbulence and control in the incompressible detached flow around a NACA0012 wing. *Int. J. Heat & Fluid Flow*, 27(5):878–886, 2006.

[215] Arun K Saha. Three-dimensional numerical simulations of the transition of flow past a cube. *Physics of Fluids*, 16(5):1630–1646, 2004.

[216] Lukasz Klotz, S Goujon-Durand, Jacek Rokicki, and JE Wesfreid. Experimental investigation of flow behind a cube for moderate Reynolds numbers. *J. Fluid Mech.*, 750:73–98, 2014.

[217] Qingrui Meng, Hongwei An, Liang Cheng, and Mehrdad Kimiaei. Wake transitions behind a cube at low and moderate Reynolds numbers. *J. Fluid Mech.*, 919:A44, 2021.

[218] AK Saha. Three-dimensional numerical study of flow and heat transfer from a cube placed in a uniform flow. *Int. J. Heat & Fluid Flow*, 27(1):80–94, 2006.

[219] A Haider and O Levenspiel. Drag coefficient and terminal velocity of spherical and nonspherical particles. *Powder technology*, 58(1):63–70, 1989.

[220] A. Hölzer and Martin Sommerfeld. New simple correlation formula for the drag coefficient of nonspherical particles. *Powder Technology*, 184(3):361–365, 2008.

[221] Majid Hassan Khan, Atul Sharma, and Amit Agrawal. Simulation of flow around a cube at moderate reynolds numbers using the lattice boltzmann method. *Journal of Fluids Engineering*, 142(1):011301, 2020.

[222] Majid Hassan Khan, P Sooraj, Atul Sharma, and Amit Agrawal. Flow around a cube for Reynolds numbers between 500 and 55,000. *Experimental thermal and fluid science*, 93:257–271, 2018.

[223] TA Johnson and VC Patel. Flow past a sphere up to a Reynolds number of 300. *J. Fluid Mech.*, 378:19–70, 1999.

[224] Ananias G Tomboulides and S.A Orszag. Numerical investigation of transitional and weak turbulent flow past a sphere. *J. Fluid Mech.*, 416:45–73, 2000.

[225] Vincenzo Citro, Lorenzo Siconolfi, D. Fabre, Flavio Giannetti, and Paolo Luchini. Stability and sensitivity analysis of the secondary instability in the sphere wake. *AIAA Journal*, 55(11):3661–3668, 2017.

[226] Ivette Rodriguez, Ricard Borell, O. Lehmkuhl, Carlos D Perez Segarra, and Assensi Oliva. Direct numerical simulation of the flow over a sphere at $Re = 3700$. *J. Fluid Mech.*, 679:263–287, 2011.

[227] E. K. W. Poon, A. S. H. Ooi, M. Giacobello, G. Iaccarino, and D. Chung. Flow past a transversely rotating sphere at Reynolds numbers above the laminar regime. *J. Fluid Mech.*, 759:751–781, 2014.

[228] Frederick W Roos and William W Willmarth. Some experimental results on sphere and disk drag. *AIAA Journal*, 9(2):285–291, 1971.

[229] Jaber Almedeij. Drag coefficient of flow around a sphere: Matching asymptotically the wide trend. *Powder Technology*, 186(3):218–223, 2008.

[230] R. Clift, J. R. Grace, and M. E. Weber. *Bubbles, drops, and particles*. Courier Corporation, 2005.

[231] R Turton and O Levenspiel. A short note on the drag correlation for spheres. *Powder technology*, 47(1):83–86, 1986.

[232] Giwoong Yun, Dongjoo Kim, and Haecheon Choi. Vortical structures behind a sphere at subcritical Reynolds numbers. *Physics of Fluids*, 18(1), 2006.

[233] Sonu S. Varghese, S.H. Frankel, and Paul F. Fischer. Direct numerical simulation of stenotic flows. part 1. steady flow. *J. Fluid Mech.*, 582:253–280, 2007.

[234] M. Waldmann, M. Rüttgers, A. Lintermann, and W. Schröder. Virtual Surgeries of Nasal Cavities Using a Coupled Lattice-Boltzmann–Level-Set Approach. *Journal of Engineering and Science in Medical Diagnostics and Therapy*, 5(3), 2022.

[235] Sonu S. Varghese, S.H. Frankel, and Paul F. Fischer. Direct numerical simulation of stenotic flows. part 2. pulsatile flow. *J. Fluid Mech.*, 582:281–318, 2007.

[236] Kartik Jain. Transition to turbulence in an oscillatory flow through stenosis. *Biomechanics and Modeling in Mechanobiology*, pages 1–19, 02 2020.

[237] Mohammad Farazmand and Themistoklis P. Sapsis. Closed-loop adaptive control of extreme events in a turbulent flow. *Phys. Rev. E*, 100:033110, Sep 2019.

[238] H.K. Moffatt. Extreme events in turbulent flow. *J. Fluid Mech.*, 914:F1, 2021.

[239] Gaurav Kumar and Aditya Nair. Stabilizing two-dimensional turbulent kolmogorov flow via selective modification of inviscid invariants. *Physics of Fluids*, 35(12), 2023.

[240] Guido Boffetta and Robert E. Ecke. Two-dimensional turbulence. *Ann. Rev. Fluid Mech.*, 44, 2012.

[241] Z. Yin, H.J.H. Clercx, and D.C. Montgomery. An easily implemented task-based parallel scheme for the Fourier pseudospectral solver applied to 2D Navier–Stokes turbulence. *Computers & Fluids*, 33(4):509–520, 2004.

[242] Gideon Dresdner, Dmitrii Kochkov, P.C. Norgaard, L. Zepeda-Nunez, Jamie Smith, Michael Brenner, and Stephan Hoyer. Learning to correct spectral methods for simulating turbulent flows. *Transactions on Machine Learning Research*, 2023.

[243] R. Byron Bird, Warren E. Stewart, and Edwin N. Lightfoot. *Transport Phenomena*. John Wiley & Sons, New York, 2nd edition, 2002.

[244] K. S. Nelson and O. B. Fringer. Reducing spin-up time for simulations of turbulent channel flow. *Physics of Fluids*, 29(10):105101, 10 2017.

[245] Ville Vuorinen and K Keskinen. Dnslab: A gateway to turbulent flow simulation in matlab. *Computer Physics Communications*, 203:278–289, 2016.

[246] Jason Rader, Terry Lyons, and Patrick Kidger. Lineax: unified linear solves and linear least-squares in jax and equinox, 2023.

[247] E. P. Hammond, T. R. Bewley, and P. Moin. Observed mechanisms for turbulence attenuation and enhancement in opposition-controlled wall-bounded flows. *Physics of Fluids*, 10(9):2421–2423, 09 1998.

[248] A. Stroh, B. Frohnapfel, P. Schlatter, and Y. Hasegawa. A comparison of opposition control in turbulent boundary layer and turbulent channel flow. *Physics of Fluids*, 27(7):075101, 07 2015.

[249] E. Lagemann, S. L. Brunton, and C. Lagemann. Uncovering wall-shear stress dynamics from neural-network enhanced fluid flow measurements. *Proc. Roy. Soc. A*, 480(2292):20230798, 2024.

[250] Esther Lagemann, Julia Roeb, Steven L Brunton, and Christian Lagemann. A deep learning approach to wall-shear stress quantification: from numerical training to zero-shot experimental application. *Journal of Fluid Mechanics*, 1014:A1, 2025.

Appendices

SI 1 Extended Introduction

The control of fluid flows is a critical challenge across virtually every major industry, from aerospace and automotive to energy production and manufacturing. Improved flow control has the potential to transform trillion-dollar sectors by dramatically improving energy efficiency, transportation systems, and industrial processes. However, fluid flow control remains notoriously challenging due to the nonlinear, multiscale nature of turbulent flows, resulting in control formulations that are high-dimensional, non-convex, and computationally intractable using traditional approaches [62, 63]. The convergence of recent breakthroughs in reinforcement learning (RL) with advances in differentiable physics simulation [28, 30] and specialized hardware acceleration has created an unprecedented opportunity to revolutionize fluid dynamics control through artificial intelligence (AI).

This revolution encompasses both the practical implementation of flow control and the fundamental scientific understanding that underpins it. AI-driven differentiable physics environments represent a transformative scientific tool for advancing our fundamental understanding of fluid dynamics. The key advantage of differentiable simulations lies in their ability to compute exact gradients of objective functions (such as drag, lift, or mixing efficiency) with respect to control inputs, geometric parameters, or initial conditions through automatic differentiation. This enables gradient-based optimization and sensitivity analysis that would require prohibitively many simulations with traditional adjoint methods or finite-difference approximations, particularly for high-dimensional control spaces and long time horizons.

Moreover, the combination of differentiable physics with RL creates a unique scientific tool: agents can autonomously discover non-intuitive control strategies and flow manipulation techniques that human intuition might overlook, effectively serving as computational experiments that probe the limits of what is physically achievable. These discovered strategies often reveal unexpected connections between control actuation and flow response, inspiring new hypotheses about underlying physical mechanisms. The gradient information also enables systematic inverse design—working backward from desired flow features to determine the forcing or geometry required to achieve them—which is invaluable for developing physics-based reduced-order models and improving turbulence closure schemes. By providing efficient pathways to explore the control-response landscape and extract interpretable patterns from successful strategies, these platforms establish a new methodology for scientific discovery that complements traditional CFD while offering unique capabilities for optimization, inverse problems, and automated discovery of control principles.

To understand the potential of this technological convergence, consider the vast economic significance of fluid flow control, which extends across industries representing over $10 trillion in global market value. The industrial flow control sector alone represents a $225 billion market*, with direct applications spanning aerospace systems valued at $3.2 billion and projected to reach $30 billion by 2032†, energy systems where industrial pumping accounts for nearly 20% of global electrical demand, and manufacturing processes across sectors responsible for 38% of industrial CO_2 emissions‡. Breakthrough successes in wind energy control have reduced costs from 55+ cents/kWh in 1980 to under 3 cents/kWh today§, creating thousands of jobs and generating $10 billion in annual investments.

This economic imperative coincides with a remarkable period of breakthrough achievements in reinforcement learning, particularly in complex scientific applications that mirror the challenges of fluid dynamics control. Reinforcement learning has demonstrated transformative capabilities across increasingly complex scientific domains, recently resulting in the 2024 Nobel Prizes in Physics for foundational neural network

*McKinsey & Company, "Flow control: Sector at a crossroads?" https://www.mckinsey.com/industries/industrials-and-electronics/our-insights/flow-control-sector-at-a-crossroads

†Global Market Insights, "Aerospace & Defense Fluid Conveyance Systems Market Size, 2032." https://www.gminsights.com/industry-analysis/aerospace-defense-fluid-conveyance-systems-market

‡U.S. Department of Energy, "Transformative Pathways for US Industry," January 2025. https://www.energy.gov/sites/default/files/2025-01/transformative-pathways-for-us-industry.pdf

§American Clean Power Association, "Wind Power Facts and Statistics." https://cleanpower.org/facts/wind-power/

research that enables modern RL systems[¶], and in Chemistry for AlphaFold's revolutionary protein structure prediction [12]. AlphaFold solved the 50-year protein folding challenge by achieving experimental-level accuracy within minutes rather than months, predicting structures for over 200 million proteins and fundamentally transforming biological research[||]. Concurrent breakthroughs in plasma control demonstrate RL's capability to master complex physical systems: DeepMind's deployment of deep RL controllers on the TCV tokamak achieved real-time control of 100+ million°C plasmas at 10 kHz frequencies, enabling previously impossible configurations including sustained "droplets" and high-elongation shapes critical for fusion energy [13]. These systems overcame fundamental challenges including 19+ coupled magnetic coils, millisecond timescales with instability growth rates exceeding 1.4 kHz, and safety-critical constraints where failures could damage multi-billion dollar facilities.

These applications share common success factors that provide crucial insights for advancing fluid flow control. The success of RL across diverse domains has been catalyzed by standardized benchmark environments that democratize research access and accelerate algorithmic innovation. OpenAI Gym has attracted over 2 million users across 190 countries[**], while specialized environments, such as MuJoCo for robotics and Atari for discrete control established evaluation frameworks that transformed entire research communities [64]. These platforms enabled fair algorithmic comparison, reproducible research, and systematic progress tracking that proved essential for breakthrough developments including AlphaGo, robotics deployments, and large language model alignment through reinforcement learning from human feedback.

However, despite these remarkable successes in analogous complex domains, fluid dynamics has remained largely resistant to similar breakthroughs due to a constellation of fundamental technical barriers. The primary obstacle is computational intractability: training effective RL agents typically requires thousands of environment interactions, but each fluid dynamics evaluation demands expensive computational fluid dynamics (CFD) simulations that can require hours on high-performance computing clusters. This computational bottleneck is magnified by the inherent sample inefficiency of model-free RL methods, creating practical impossibility for complex turbulent flow problems. Moreover, traditional CFD approaches face severe limitations in real-time control applications, with typical simulations requiring wall-clock times orders of magnitude longer than the physical processes they model.

Beyond computational constraints, fundamental challenges in generalization and adaptability have further impeded progress. Current RL approaches trained at specific Reynolds numbers fail to transfer to different flow regimes, and agents optimized for particular geometries cannot adapt to modified configurations [65]. The transition from laminar to turbulent conditions introduces chaotic, irregular dynamics that destabilize training algorithms, while the multiscale nature of turbulence—spanning from energy-containing large scales to dissipative Kolmogorov microscales—necessitates extensive data collection across multiple scales, which amplifies computational costs. Traditional control approaches face complementary limitations: PID controllers with fixed parameters cannot adapt to highly nonlinear turbulent flows, while optimal control theory encounters severe time horizon limitations due to instability in adjoint equations for chaotic systems [14].

Compounding these technical challenges, the fluid dynamics community has lacked the comprehensive benchmark platforms that have enabled other domains. While computer vision benefits from standardized datasets, such as ImageNet, that enable systematic algorithmic comparison, fluid dynamics researchers work with limited, problem-specific configurations that prevent fair evaluation and reproducible research. Most existing fluid dynamics RL efforts have concentrated on computationally inexpensive 2D configurations at moderate Reynolds numbers, with the extension to highly turbulent flows, complex 3D geometries, and multiphysics applications representing the current frontier of research.

Remarkably, the technological landscape has undergone a dramatic transformation that now makes it possible to overcome these historical barriers. GPU-accelerated differentiable fluid simulators now achieve

[¶]The Nobel Prize, "Press release: The Nobel Prize in Physics 2024." https://www.nobelprize.org/prizes/physics/2024/press-release/

[||]Google DeepMind, "AlphaFold." https://deepmind.google/science/alphafold/

[**]OpenAI, "OpenAI Gym Beta." https://openai.com/index/openai-gym-beta/

orders-of-magnitude speedups over traditional CFD methods, with modern platforms enabling parallel environment training at scales previously requiring supercomputers [14]. The ML4CFD competition at NeurIPS 2024, featuring over 240 teams, demonstrated 300-600x speedups over traditional solvers while maintaining accuracy[††], indicating the maturity of these approaches for practical applications. Differentiable reinforcement learning methods specifically designed for continuous control problems address sample efficiency challenges, with approaches using analytic gradients from differentiable simulation to dramatically reduce sample complexity in multiphysics environments [66]. Physics-informed neural networks provide principled ways to incorporate fluid dynamics knowledge into RL systems, achieving superior performance in strongly nonlinear problems with sparse data [67].

The commercial sector has validated this technological readiness through concrete deployments and performance improvements. Major CFD vendors including Ansys and Siemens have launched GPU-accelerated solvers showing 20-33x performance improvements, while enterprise platforms provide production-grade tools for physics-informed machine learning. This convergence of mature differentiable simulation technology, breakthrough RL algorithms, and accessible hardware represents the first time that large-scale fluid dynamics RL training has become computationally feasible.

The urgency of capitalizing on this technological convergence is underscored by the massive economic stakes and immediate industrial needs for improved fluid control solutions. Advanced aerodynamic control in automotive and aerospace applications could generate billions in fuel savings across global fleets. For instance, removing side mirrors alone in vehicles (accounting for around 6% of form drag [68]) improves fuel economy by 1.5-2 miles per gallon, while comparable drag reductions in aircraft yield proportionally larger savings due to higher fuel consumption rate [69, 70]. Coordinated wind turbine controls can increase farm output by 4-5%[‡‡], representing substantial returns across the $10 billion annual wind investment market. Industrial applications present even larger opportunities: pumping systems account for nearly 20% of global electrical energy demand, with potential energy savings up to 75% through advanced control. Manufacturing industries face direct competitive pressures where fluid control improvements translate to immediate economic advantages, from billion-dollar steel production operations to chemical processing facilities requiring millisecond response times for safety-critical applications.

Responding to this critical convergence of technological capability and economic opportunity, we introduce HydroGym, a benchmark flow control platform designed to bridge the gap between cutting-edge RL method development and fluid dynamics applications. HydroGym provides a flexible, solver-independent interface that seamlessly integrates with industry-standard RL frameworks while supporting both differentiable and non-differentiable fluid dynamics environments. Our platform abstracts computational fluid dynamics complexity from control algorithm development, enabling researchers from both communities to advance the field through standardized benchmarks and reproducible evaluation protocols.

The specific contributions of this work directly address each of the critical barriers that have prevented breakthrough progress in fluid dynamics RL:

- **Comprehensive benchmark platform**: Introduction of the first scalable RL platform specifically designed for fluid dynamics control, featuring a solver-independent architecture that supports diverse CFD backends and computational configurations.
- **Diverse environment suite**: Forty-two non-differentiable flow control environments with increasing complexity, from canonical flows past cylinders to advanced turbulent control scenarios on 3D aircraft wings, plus an initial set of differentiable flow control environments enabling gradient-based RL methods.
- **Systematic algorithmic evaluation**: Comprehensive performance assessment using industry-standard algorithms including Proximal Policy Optimization (PPO), Deep Deterministic Policy Gradient (DDPG), and Twin Delayed DDPG (TD3), establishing baseline performance metrics for future research.

[††]"NeurIPS 2024 ML4CFD Competition: Results and Retrospective Analysis." https://arxiv.org/abs/2506.08516

[‡‡]U.S. Department of Energy, "Next-Generation Wind Technology." https://www.energy.gov/eere/wind/next-generation-wind-technology

- **Democratized research access**: Platform enables RL researchers and fluids experts to collaborate via standardized interfaces, lowering barrier to entry and accelerating interdisciplinary progress.
- **Extensible foundation**: Readily extensible framework supports integration of new CFD solvers, environments, and RL algorithms, to evolve with advancing technology and research needs.

Through this comprehensive approach, HydroGym addresses the specific technical barriers that have prevented breakthrough progress – computational intractability through state-of-the-art GPU-powered CFD solvers and efficient simulation interfaces, sample inefficiency through differentiable environments, generalization challenges through diverse benchmarks, and accessibility barriers through democratized platforms – thereby enabling the transition from traditional engineering approaches to AI-driven fluid control systems. The platform arrives at a critical juncture where enabling technologies have matured and economic pressures intensify, positioned to catalyze transformative progress comparable to breakthroughs in protein folding, plasma control, and other complex scientific domains. Just as AlphaFold demonstrated that the convergence of deep learning, domain expertise, and computational resources could solve seemingly intractable scientific challenges, HydroGym establishes the foundation for similar breakthroughs in fluid dynamics control. Success in this domain promises a fundamental transformation of how we approach complex flow systems across trillion-dollar industries, establishing artificial intelligence as an essential tool for addressing the most challenging problems in fluid mechanics and beyond.

SI 2 Extended literature review

The intersection of reinforcement learning and flow control represents a paradigm shift in fluid system optimization. Traditional methods rely on predetermined strategies based on domain knowledge, while reinforcement learning enables autonomous discovery of optimal control policies through the direct interaction with flow environments. This capability is particularly valuable in turbulent flows, where traditional linear control theory fails due to high-dimensional, chaotic dynamics. Since the first successful demonstration of deep reinforcement learning for cylinder wake control [71], the field has experienced rapid growth. The progression from proof-of-concept studies to practical implementations reveals the maturation of core methodologies and sophisticated frameworks capable of handling realistic engineering problems. This evolution has been driven by advances in deep learning architectures, increased computational resources, and growing recognition of traditional control limitations for complex fluid systems.

Canonical Flow Problems and Foundational Methods. The journey toward practical reinforcement learning in flow control began with carefully chosen problems that balanced complexity with computational feasibility. The application of reinforcement learning to circular cylinder wake control was a first step, establishing foundational principles for the field [71]. The canonical von Kármán vortex street suppression provided a computationally tractability testbed, allowing researchers to develop and validate core methodologies before tackling more challenging applications.

Building on these initial successes, numerous studies consistently achieved $8-15\%$ drag reduction with minimal actuation energy (0.5-1% of momentum deficit), demonstrating that neural agents could autonomously discover effective control strategies without prior knowledge of flow physics [19, 72–75]. These results were encouraging because they showed that reinforcement learning could match or exceed the performance of carefully tuned traditional controllers without prior understanding of the underlying flow physics. Crucially, experimental validation eliminated concerns about simulation-to-reality transfer that had plagued earlier computational studies. Laboratory studies using rotating cylinders achieved similar performance improvements [20], with drag reductions of 25-30% at Reynolds numbers up to 140,000. This success proved that reinforcement learning can handle noise, measurement uncertainties, and modeling errors inherent in real fluid systems.

Attention has since turned to more complex geometries that better represent practical engineering challenges. Square cylinder flows present additional complexity due to fixed separation points and pronounced pressure fluctuations [76–80]. Reinforcement learning policies often learn to employ multi-frequency patterns differing significantly from natural shedding frequencies, highlighting the discovery potential of learning-based methods.

The field has rapidly matured towards industrially relevant flows. Studies at Reynolds numbers exceeding 200,000 have achieved substantial drag reduction through multi-frequency control strategies [81]. Further, multi-agent reinforcement learning has shown superior performance compared to single-actuator approaches [15, 32], setting the stage for more complex applications requiring distributed control.

Shape Optimization and Advanced Applications. A natural next step in RL for fluids was to explore design optimization where the geometry itself becomes the control parameter. Reinforcement learning for shape optimization represents a major step toward autonomous design generation [82, 83]. This transition from controlling existing geometries to generating new ones opened new possibilities for fluid engineering. Modern frameworks parameterize complex shapes via Bézier curves or B-splines with hundreds of design variables [21, 84]; optimization in these spaces was previously intractable. The key advantage over conventional optimization lies in reinforcement learning's ability to navigate high-dimensional design spaces without getting trapped in local optima, while simultaneously handling multiple competing objectives.

This multi-objective capability has proven particularly valuable for airfoil design, where competing requirements must be balanced across flight conditions. Reinforcement learning frameworks generate continuous Pareto fronts representing optimal trade-offs between lift and drag across ranges of Reynolds numbers and angles of attack [85]. Performance comparisons consistently demonstrate superiority over traditional optimization methods, with superior resistance to local minima and better generalization to untested operating conditions.

The success in two-dimensional applications naturally led to more ambitious and industrially relevant three-dimensional flows. Automotive and marine applications have leveraged reinforcement learning for complex three-dimensional geometries [86, 87], where traditional optimization approaches become computationally prohibitive. Marine applications have achieved significant reductions in acoustic signatures while maintaining hydrodynamic performance [88], while hull optimization frameworks generate designs meeting multiple constraints simultaneously [89], demonstrating the technology's readiness for real-world engineering problems.

Separation Control and Turbulent Flow Applications. Flow separation control represents one of the most demanding applications, requiring precise manipulation of boundary layer dynamics in highly unsteady environments. Reinforcement learning has revealed sophisticated strategies surpassing traditional periodic actuation [4, 90], often discovering control mechanisms that human experts had not previously considered. Plasma actuators enable precise boundary layer manipulation [91], with learned policies discovering multi-frequency control strategies that simultaneously modify large-scale structures while fine-tuning smaller-scale phenomena. This multi-scale control represents a significant advance over traditional approaches that typically target single frequency ranges or specific flow scales.

The complexity of separation control is perhaps best illustrated in dynamic stall applications, where reinforcement learning has achieved complete stall prevention rather than mere mitigation [92]. These applications require real-time adaptation to rapidly changing flow conditions, demonstrating the technology's potential for autonomous flight control. Multi-actuator systems coordinated by multi-agent frameworks enable spatially distributed manipulation with precision unattainable through centralized approaches.

The application of reinforcement learning to fully turbulent channel flow control has emerged as a canonical problem for high Reynolds number evaluation [93–96], representing conditions typical of many engineering applications. Successful agents achieve drag reduction levels of 20-40% across Reynolds numbers spanning two orders of magnitude, with performance scaling favorably with system size. The RL

control mechanisms often differ fundamentally from traditional opposition control, employing sophisticated strategies that redistribute turbulent kinetic energy across different components and locations. Multi-agent reinforcement learning has addressed scalability for spatially distributed control, enabling parallelization across multiple locations while avoiding exponential complexity growth, pointing toward practical implementations in large-scale systems.

Bio-Inspired and Bio-medical Applications. Researchers have also explored how RL can provide insights into biological systems, while simultaneously investigating bio-inspired approaches for artificial applications. These studies yield insights into natural propulsion while revealing opportunities for artificial systems to potentially exceed biological performance. Self-propelled swimming studies reproduce complex behaviors including rheotaxis and Kármán gaiting [97–100], demonstrating that reinforcement learning can discover sophisticated control strategies evolved by natural swimmers. Multi-agent applications to collective swimming reveal coordination emerging from individual optimization without explicit communication [101, 102], suggesting new approaches for autonomous swarms.

Reinforcement learning for bio-medical fluids have mainly been used for respiration and hemodynamics. In the respiratory system, patient-specific respiratory flow simulations have been coupled with reinforcement learning to propose surgical interventions in the nasal cavity that optimize nasal resistance and improve the airway's capacity to heat incoming air [103, 104]. In the cardiovascular system, reinforcement learning agents have been trained to regulate nerve stimulation to maintain target heart rate and mean arterial pressure [105], to control the motor speed of cardiovascular pumps in order to restore pulsatility under varying heart failure conditions [106], or to design optimal stent placements in patient-specific aneurysm geometries [107]. Together, these studies highlight the potential of reinforcement learning and physics-based simulations to enable personalized medicine and support clinical decision-making.

Computational Enhancement and Algorithmic Advances. Parallel to advances in direct flow control applications, reinforcement learning has begun transforming the computational tools used to study fluid mechanics itself. RL for CFD solver optimization represents a paradigm shift toward intelligent computational fluid dynamics, where the simulation process itself becomes adaptive and self-optimizing. Adaptive mesh refinement applications treat grid optimization as sequential decision problems [108–110], with learned strategies demonstrating superior performance compared to conventional error-based approaches. High-order method integration enables simultaneous optimization of mesh topology and polynomial order distributions [111], potentially revolutionizing how CFD simulations are constructed and executed.

Concurrently, reinforcement learning has emerged as a transformative approach for turbulence modeling, addressing long-standing challenges in Reynolds-Averaged Navier-Stokes (RANS) closure and Large-Eddy subgrid scale modeling. By treating model parameter optimization as an adaptive learning problem where coefficients adjust based on local flow conditions [112–115], these approaches overcome the fundamental limitation of traditional turbulence models that rely on universal constants derived from canonical flows.

Multi-agent reinforcement learning frameworks have been successfully applied to wall-model development for large eddy simulations, enabling distributed optimization of near-wall turbulence representations while maintaining computational efficiency [16, 116]. Physics-informed reinforcement learning approaches have integrated governing differential equations directly into the learning framework, ensuring that learned turbulence models satisfy fundamental conservation laws while improving predictive accuracy across diverse flow configurations [117, 118]. Data-driven model development leveraging high-fidelity simulation databases has demonstrated superior performance compared to traditional fixed-parameter approaches, with learned models providing better uncertainty quantification and adaptability to new flow regimes. Model-consistent training strategies that incorporate CFD solvers directly into the learning process have addressed the distribution shift problems that previously limited machine learning applications to turbulence modeling, enabling effective deployment in practical engineering simulations.

These advances represent a paradigm shift toward intelligent turbulence modeling where algorithms

continuously adapt their closure strategies based on evolving flow physics rather than relying on universal constants derived from canonical flows. This adaptability is particularly valuable for complex engineering flows that deviate significantly from the canonical configurations used to calibrate traditional models.

Another promising direction targets model-based reinforcement learning approaches in flow control learning surrogate models of fluid dynamics to enable more sample-efficient policy optimization [17, 119, 120]. These lightweight, physics-informed models provide significant computational advantages over high-fidelity CFD simulations during policy training while maintaining sufficient accuracy for effective control strategy development, enabling practical deployment of reinforcement learning in scenarios where extensive interaction with expensive fluid solvers would otherwise be prohibitive.

The convergence of reinforcement learning with fluid mechanics has evolved from isolated demonstrations to a comprehensive framework capable of addressing fundamental challenges across the discipline, from turbulence closure modeling to autonomous system design. This progression demonstrates not just the maturation of individual techniques, but the emergence of a new paradigm for approaching fluid mechanics problems that emphasizes adaptation, learning, and autonomous optimization. Looking forward, the integration of physics-informed learning algorithms with high-performance computing promises to unlock previously intractable optimization problems in fluid systems, potentially revolutionizing fields ranging from renewable energy harvesting to biomedical device design. As these methodologies mature beyond laboratory settings toward real-world implementation, they represent a paradigmatic shift toward intelligent, adaptive fluid systems that autonomously optimize their performance in response to changing environmental conditions, fundamentally changing how we design and operate fluid mechanical systems.

SI 3 HydroGym - Numerical Backends and Implementation

HydroGym provides multiple computational backends to accommodate diverse research requirements and computational resources in flow control applications. The framework's modular architecture supports three distinct solver implementations: a high-performance lattice Boltzmann method (LBM) solver built on the m-AIA framework for large-scale simulations (Section 3.1), a JAX-based implementation optimized for machine learning workflows (Section 3.2), and a Firedrake finite element backend designed for maximum code transparency and extensibility (Section 3.3). Each implementation targets specific use cases while maintaining a unified interface for reinforcement learning integration, enabling researchers to select the most appropriate computational approach based on their performance requirements, hardware constraints, and research objectives.

3.1 m-AIA implementation

The direct numerical simulations are conducted using a lattice Boltzmann method (LBM) embedded within the m-AIA solver framework, which is continuously developed at the Institute of Aerodynamics of RWTH Aachen University for over two decades [24]. This method solves a discretized form of the Boltzmann equation, which describes the evolution of the particle distribution function $f(\mathbf{x}, \mathbf{v}, t)$ in time t and space $x = (x, y, z)$:

$$\frac{\partial f}{\partial t} + \mathbf{v} \cdot \nabla f = \Omega(f). \tag{1}$$

Here, $\Omega(f)$ is the collision operator, which models the redistribution of particle populations due to intermolecular collisions. Through a first-order Chapman-Enskog expansion of this equation, the Navier-Stokes equations can be recovered, establishing the method's connection to macroscopic fluid dynamics.

The discretization of the continuous Boltzmann equation results in the lattice Boltzmann equation (LBE), which evolves discrete particle populations f_i on a computational grid. The LBE update rule follows a

two-step process consisting of collision and streaming phases:

$$f_i(\mathbf{x} + \mathbf{c}_i \Delta t, t + \Delta t) = f_i(\mathbf{x}, t) + \Omega_i(f). \tag{2}$$

For the present test cases, a three-dimensional lattice with 27 discrete velocity vectors ($\mathbf{c}_i$) is employed, which is known as the D3Q27 model. From these discrete particle distributions, macroscopic fluid variables such as density ρ and velocity $\mathbf{u}$ are computed from the moments:

$$\rho = \sum_i f_i \quad \text{and} \quad \rho \mathbf{u} = \sum_i \mathbf{c}_i f_i. \tag{3}$$

Overall, m-AIA's LBM solver offers two different collision operators. The first approach is the widely-used Bhatnagar-Gross-Krook (BGK) model [121], which relaxes the particle distributions towards a local Maxwellian equilibrium f_i^{eq} with a single relaxation frequency ω_{BGK}:

$$\Omega_i = \omega_{\text{BGK}}(f_i^{\text{eq}} - f_i). \tag{4}$$

The relaxation frequency is related to the effective kinematic viscosity v_{eff} of the fluid by $\omega_{\text{BGK}} = (\Delta t c_s^2)/(v_{\text{eff}} + 0.5\Delta t c_s^2)$, where c_s is the lattice speed of sound. For isothermal and low-Mach number flows, the equilibrium distribution is given by:

$$f_i^{\text{eq}} = w_i \rho \left[1 + \frac{\mathbf{c}_i \cdot \mathbf{u}}{c_s^2} + \frac{(\mathbf{c}_i \cdot \mathbf{u})^2}{2c_s^4} - \frac{\mathbf{u} \cdot \mathbf{u}}{2c_s^2} \right], \tag{5}$$

with w_i being the lattice-dependent weighting factors.

For enhanced stability in simulations of higher Reynolds number flows, an alternative cumulant-based collision operator is employed [122]. In this approach, the collision is performed in the space of statistical cumulants c_α, which are relaxed towards their equilibrium values with a set of distinct relaxation rates ω_α. The post-collision state in cumulant space is expressed as $c_\alpha^* = c_\alpha + \omega_\alpha(c_\alpha^{\text{eq}} - c_\alpha)$. Following the methodology of Geier et al. [122], all relaxation rates are set to unity except for one, which is set equal to ω_{BGK} to control the fluid viscosity.

For thermal simulations, a second set of particle distributions g_i is solved. To compute the thermal equilibrium distributions, three approaches have been validated and employed in respiratory flow simulations with m-AIA: (1) treating the temperature (T) solely as a passive scalar [83, 123], (2) including internal energy effects [124], and (3) considering total energy [103, 104]. Similar to Eq. 3, T is computed from the moments of g_i.

Furthermore, local grid refinement is implemented based on the method proposed by Dupuis and Chopard [125] to efficiently resolve flow features across different length scales. This refinement strategy involves adjusting the relaxation frequency on different grid levels to maintain a constant kinematic viscosity across the entire domain. Since the time step Δt is scaled with the local grid spacing Δ, the viscosity is kept constant by setting the local relaxation frequency according to:

$$v_{\text{eff}} = \Delta t c_s^2 \left(\frac{1}{\omega_{\text{BGK}}} - \frac{1}{2} \right). \tag{6}$$

Boundary Conditions and actuation control. Solid boundaries within the fluid domain are handled using an interpolated bounce-back scheme [126]. This method provides a second-order accurate representation of the no-slip condition for arbitrarily shaped geometries. For the far-field boundaries, inlet and outlet conditions are imposed by setting the particle distributions to an equilibrium state based on prescribed velocity, density, or temperature values, while using second-order extrapolation for any unknown variables from the domain's interior.

Flow control is implemented by changing the inflow temperature in the thermal benchmark cases, and by imposing time-varying Dirichlet boundary conditions on the surface of the immersed body in the remaining cases. These conditions modify the standard no-slip wall condition by specifying a non-zero velocity vector, $\mathbf{u}_w$, which is then enforced through the interpolated bounce-back scheme. Two distinct types of actuation are employed: synthetic jet actuation and surface rotation. Both methods utilize a temporal ramping mechanism to ensure smooth transitions between control actions, which is critical for numerical stability.

Temporal Smoothing of Control Actions. To prevent numerical instabilities arising from discontinuous changes in boundary conditions, the control action is never applied instantaneously. Instead, the actuation magnitude $A(t)$ (representing either jet velocity or angular velocity) is smoothly interpolated from its value at the previous control step, A^{old}, to the new target value, A^{new}, over a predefined number of sub-iterations N_r.

Hence, the instantaneous actuation magnitude is calculated as:

$$A(t) = A^{\text{old}} + (A^{\text{new}} - A^{\text{old}}) \cdot R(\tau), \tag{7}$$

where $\tau = (t - t_{\text{update}})/(N_r \Delta t)$ is the normalized time within the ramping interval, such that $\tau \in [0, 1]$. The function $R(\tau)$ is a normalized ramp function that maps from 0 to 1. Two different ramp functions are available to tune the actuation response:

- Hyperbolic Tangent Ramp: This function provides a smooth, S-shaped transition that is gentle at the beginning and end of the ramp period. It is defined as:

$$R_{\tanh}(\tau) = \frac{1}{2} \left(\tanh \left(b(\tau - 0.5) \right) + 1 \right). \tag{8}$$

  The parameter b controls the steepness of the ramp.

- Exponential Ramp: This function provides a ramp that starts slowly and accelerates, allowing for a more aggressive actuation towards the end of the interval. It is defined as:

$$R_{\exp}(\tau) = \frac{e^{k\tau} - 1}{e^k - 1}. \tag{9}$$

  The parameter k controls the curvature, or aggressiveness, of the exponential ramp.

Synthetic Jet Actuation. This boundary condition models synthetic jets by prescribing a velocity profile over specified regions of the wall. Each jet j is defined by its center position $\mathbf{x}_j$, blowing angle α_j, and width W_j. The velocity profile is parabolic, ensuring it is maximal at the centerline and smoothly decays to zero at the jet's edges. The velocity vector $\mathbf{u}_w(\mathbf{x}, t)$ for a point $\mathbf{x}$ within the jet's active region is determined by the product of a spatial profile function $\mathbf{S}_j(\mathbf{x})$ and the time-varying jet velocity magnitude $A_j(t)$:

$$\mathbf{u}_w(\mathbf{x}, t) = A_j(t) \cdot \mathbf{S}_j(\mathbf{x}). \tag{10}$$

The spatial profile vector $\mathbf{S}_j(\mathbf{x})$ combines the jet's shape and direction:

$$\mathbf{S}_j(\mathbf{x}) = \left(1 - \left(\frac{2d_\perp}{W_j} \right)^2 \right) \mathbf{t}_j, \tag{11}$$

where $\mathbf{t}_j = (\cos \alpha_j, \sin \alpha_j)$ is the unit vector in the direction of the jet, and $d_\perp$ is the perpendicular distance from the point $\mathbf{x}$ to the jet's centerline. This profile is applied for locations where $d_\perp \leq W_j/2$. The jet magnitude $A_j(t)$ is supplied by the control agent and interpolated using one of the temporal smoothing

functions described by Eq. 7.

Surface Rotation Actuation. This boundary condition simulates the rotation of solid surfaces, such as a cylinder. The actuation is defined by an angular velocity $\omega(t)$ around a specified center of rotation $\mathbf{x}_c$ and axis of rotation $\hat{\mathbf{a}}$. The resulting tangential velocity at any point $\mathbf{x}$ on the boundary is given by the cross product:

$$\mathbf{u}_w(\mathbf{x}, t) = \omega(t)\hat{\mathbf{a}} \times (\mathbf{x} - \mathbf{x}_c). \tag{12}$$

For a 2D simulation in the $x - y$ plane, the rotation axis is fixed to $\hat{\mathbf{a}} = (0, 0, 1)$, and the control action is the scalar angular velocity $\omega_z(t)$, which serves as the actuation magnitude $A(t)$. The velocity vector at the wall simplifies to:

$$\mathbf{u}_w(x, y, t) = \omega_z(t)(-(y - y_c), (x - x_c)). \tag{13}$$

The angular velocity $\omega_z(t)$ provided by the control agent is temporally smoothed between control updates.

MPI communications and GPU acceleration. HydroGym's C++ code implementation benefits from hybrid parallelization based on MPI and shared memory models, i.e., OpenMP and higher-level parallelism features introduced by C++17 parallel algorithms. This allows for a hardware-agnostic implementation on both CPU and GPU-based architectures, relying on GPU backends provided in, e.g., NVIDIA HPC SDK or AMD ROCm HIPSTDPAR. The hierarchical unstructured Cartesian grids are generated using a massively parallel grid generator. Previous work has achieved favorable strong and weak scaling on modern HPC systems [127]. To facilitate reproducibility and ease of deployment, we provide (pre-built) containerized environments and pre-configured setup files that enable users to readily deploy the HydroGym framework with minimal configuration overhead.

3.2 JAX implementation

Physics simulators built with modern automatic differentiation libraries make it possible to compute gradients of output quantities with respect to desired input parameters, even with complex physical processes in the middle. These gradients can then be integrated into gradient-based control schemes, one of them being gradient-enhanced reinforcement learning [38]. The HydroGym framework explores this capability by offering flow solvers written in JAX —a differentiable programming language with GPU acceleration— to model flows described by the incompressible Navier–Stokes equations:

$$\frac{\partial \mathbf{u}}{\partial t} + (\mathbf{u} \cdot \nabla)\mathbf{u} = -\nabla p + \nu \nabla^2 \mathbf{u} + \mathbf{f}, \quad \nabla \cdot \mathbf{u} = 0, \tag{14}$$

where $\mathbf{u}$ denotes the velocity, p is the pressure, ν is the kinematic viscosity and $\mathbf{f}$ is an external forcing term. HydroGym currently provides two differentiable environments which model Equation 14: a three-dimensional turbulent channel flow and a two-dimensional forced turbulence problem known as the Kolmogorov flow [128]. A more detailed implementation description of both environments is given in Secs. 5.9 & 5.10.

Software Architecture. Each environment employs a modular architecture that separates physical problem definitions from the reinforcement learning interface, following the design principles of HydroGym's Firedrake environments (Sec. 3.3) to ensure code clarity, extensibility, and ease of use. The differentiable environments differ by implementing a Gymnax interface [129] and inheriting reinforcement learning frameworks from PureJaxRL [130], enabling a fully synchronous training pipeline compatible with JAX's automatic differentiation. This architecture allows users to compute gradients of any flow output with respect to tunable input parameters at any point during environment execution or RL training via JAX's `grad` function, facilitating gradient-based optimization and control strategies.

GPU acceleration and parallelization. The JAX environments leverage GPU acceleration and parallelization to enable rapid RL training. The end-to-end framework supports parallel execution across multiple random seeds using JAX's automatic vectorization functions such as `vmap` for batch processing. This enables training hundreds of agents simultaneously in a fraction of the time required for single-agent training in PyTorch [37, 130]. Additionally, just-in-time compilation via `jit` automatically optimizes code execution on GPU hardware.

3.3 Firedrake implementation

The HydroGym framework provides an alternative implementation using Firedrake [26], a finite element framework built on PETSc that offers automatic code generation and optimization for variational problems. This implementation targets researchers requiring full access to solver internals and complete Python-based extensibility, prioritizing code transparency and flexibility over computational performance. The Firedrake backend implements two-dimensional flow control problems using mixed finite element methods for the incompressible Navier-Stokes equations.

Mathematical Formulation and Discretization. The solver employs Taylor-Hood elements with second-order continuous Galerkin (CG) elements for velocity and first-order CG elements for pressure, ensuring inf-sup stability. The discretized system takes the form:

$$\mathbf{M}\frac{\partial \mathbf{q}}{\partial t} + \mathbf{R}(\mathbf{q}) = \mathbf{0}, \tag{15}$$

where $\mathbf{q} = (\mathbf{u}, p)$ represents the mixed velocity-pressure state, $\mathbf{M}$ is the mass matrix, and $\mathbf{R}(\mathbf{q})$ is the nonlinear residual of the incompressible Navier-Stokes equations:

$$\mathbf{R}(\mathbf{q}) = \int_\Omega \left[-(\mathbf{u}\cdot\nabla)\mathbf{u}\cdot\mathbf{v} - \boldsymbol{\sigma}(\mathbf{u}, p) : \boldsymbol{\epsilon}(\mathbf{v}) + (\nabla\cdot\mathbf{u})s\right] d\Omega, \tag{16}$$

where $(\mathbf{v}, s)$ are velocity and pressure test functions, $\boldsymbol{\sigma}(\mathbf{u}, p) = 2\nu\boldsymbol{\epsilon}(\mathbf{u}) - p\mathbf{I}$ is the Newtonian stress tensor, and $\boldsymbol{\epsilon}(\mathbf{u}) = \frac{1}{2}(\nabla\mathbf{u} + (\nabla\mathbf{u})^T)$ is the strain rate tensor. Time integration is performed using implicit schemes with automatic selection of solver parameters based on Reynolds number and grid resolution.

Software Architecture. The implementation follows a three-tier modular architecture that separates physical problem definition from numerical methods and reinforcement learning interfaces. This design enables extensibility while maintaining code clarity and facilitating rapid prototyping of new flow control scenarios.

The `PDEBase` class serves as an abstract template defining the core functionality required for PDE-based control problems. It encapsulates the physical configuration including domain discretization, boundary conditions, and objective function evaluation, while remaining solver-agnostic. Key abstract methods include mesh handling (`load_mesh`, `initialize_state`), state management (`set_state`, `copy_state`, `reset`), and problem-specific definitions (`get_observations`, `evaluate_objective`). The class provides a standardized interface through which control agents interact with the underlying fluid physics, handling the conversion between control inputs and boundary condition modifications. Additionally, it manages actuator dynamics and maintains checkpoint functionality for simulation restart capabilities.

The `TransientSolver` class implements the time-stepping algorithms for evolving the PDE state. It provides a `solve` method that integrates the flow equations over specified time intervals, supporting optional callback functions for data collection and visualization. The core `step` method advances the simulation by one time increment, accepting control inputs and updating the PDE state accordingly. This

separation allows for different time integration schemes to be implemented without modifying the physical problem definition. The solver supports both open-loop time integration and closed-loop operation with feedback controllers of the form $u(t, y)$.

The `FlowEnv` class bridges the PDE framework with reinforcement learning by implementing the Farama Foundation Gymnasium interface. It wraps `PDEBase` and `TransientSolver` instances, translating between RL concepts (observations, actions, rewards) and CFD operations (state queries, boundary condition updates, objective evaluation). The environment handles episode management through reset functionality, computes rewards as the negative of the time-integrated objective function, and manages termination conditions. This design allows any combination of PDE problem and solver to be automatically instantiated as a Gym-compatible environment through configuration dictionaries.

Available Environments. The framework includes three benchmark flow configurations: flow around a circular cylinder with rotary control, flow around a cylinder with blowing/suction actuation, cavity flow with leading-edge control, and the three-cylinder pinball configuration with independent rotary actuation for each cylinder.

Computational Infrastructure The implementation supports MPI parallelization through Firedrake's distributed mesh capabilities and leverages PETSc's parallel linear algebra routines. While computational efficiency is secondary to code accessibility, the framework maintains reasonable performance for research applications through automatic optimization of generated finite element code and efficient sparse linear system solvers. The modular architecture enables researchers to extend the framework with new flow configurations by implementing problem-specific methods while inheriting the complete finite element infrastructure and RL integration capabilities. Similar to the m-AIA environments, we also provide pre-built container environments.

SI 4 Benchmarked RL Agents

The HydroGym platform conducts comprehensive performance evaluation using four distinct reinforcement learning algorithms, representing both established model-free approaches and emerging gradient-enhanced methodologies. For the non-differentiable environments, we employ TorchRL [36] as a stable baseline implementation for Proximal Policy Optimization (PPO), Deep Deterministic Policy Gradient (DDPG), and Twin Delayed Deep Deterministic Policy Gradient (TD3). Additionally, we utilize in-house implementations of PPO and Gradient-Enhanced Proximal Policy Optimization (GPPO) specifically designed for JAX-based differentiable environments [131]. This dual implementation strategy ensures optimal performance across both traditional CFD solvers and modern differentiable simulation frameworks while maintaining algorithmic consistency and reproducibility.

4.1 Proximal Policy Optimization (PPO)

PPO implements a trust region policy optimization approach that constrains policy updates through a clipped surrogate objective function to prevent destructive parameter changes during training [33]. The core innovation lies in its clipped probability ratio mechanism, which limits the extent of policy updates based on the ratio between new and old policy probabilities. The algorithm optimizes the following clipped objective:

$$L^{CLIP}(\theta) = \mathbb{E}_t \left[\min(r_t(\theta) A_t, \text{clip}(r_t(\theta), 1 - \epsilon, 1 + \epsilon) A_t) \right] \tag{17}$$

where $r_t(\theta) = \frac{\pi_\theta(a_t|s_t)}{\pi_{\theta_{old}}(a_t|s_t)}$ represents the probability ratio, A_t denotes the advantage estimate, and ϵ controls the clipping range (typically 0.2).

A Generalized Advantage Estimation (GAE) with $\lambda = 0.95$ for variance reduction in advantage calculations [132] is employed, combined with a value function loss term and entropy regularization to maintain exploration. Network architectures utilize fully connected layers with ReLU activations, featuring separate actor and critic networks. The algorithm demonstrates consistent convergence across most HydroGym flow configurations, successfully learning control policies for drag reduction tasks, cavity flow stabilization, and multi-body coordination in the fluidic pinball. Training hyperparameters are adapted per environment, with learning rates ranging from 5×10^{-5} to 1×10^{-3}, batch sizes of 16-48 experiences, and episode lengths matching the physical timescales of each flow configuration.

4.2 Deep Deterministic Policy Gradient (DDPG)

DDPG extends the deterministic policy gradient theorem to high-dimensional continuous action spaces through an actor-critic architecture combined with experience replay and target networks [34]. The algorithm involves four neural networks: an actor network $\mu(s|\theta^\mu)$ that deterministically maps states to actions, a critic network $Q(s, a|\theta^Q)$ that estimates action-value functions, and corresponding networks μ' and Q' to provide stable learning targets [133]. The critic is trained using temporal difference learning with the Bellman equation:

$$L(\theta^Q) = \mathbb{E}_{s,a,r,s' \sim \mathcal{D}} \left[(Q(s, a|\theta^Q) - y)^2 \right] \tag{18}$$

where $y = r + \gamma Q'(s', \mu'(s'|\theta^{\mu'})|\theta^{Q'})$ represents the target value computed using target networks. The actor network is updated using the deterministic policy gradient [134]:

$$\nabla_{\theta^\mu} J \approx \mathbb{E}_{s \sim \mathcal{D}} \left[\nabla_{\theta^\mu} \mu(s|\theta^\mu) \nabla_a Q(s, a|\theta^Q)|_{a=\mu(s)} \right] \tag{19}$$

Exploration during training is achieved through additive Ornstein-Uhlenbeck noise $\mathcal{N}$ with parameters $\theta = 0.15$, $\sigma = 0.2$, providing temporally correlated exploration in the action space [135]. Target networks are updated using soft updates with $\tau = 0.005$ to ensure stable learning dynamics. We employ replay buffers of size 10^4 to 10^5 experiences, with batch sampling of 256 transitions per update step. Network architectures feature 256-512 hidden units across two hidden layers, utilizing batch normalization for improved training stability [136].

4.3 Twin Delayed Deep Deterministic Policy Gradient (TD3)

TD3 addresses the overestimation bias inherent in DDPG through three key modifications: twin critic networks, delayed policy updates, and target policy smoothing [35]. The twin critic architecture maintains two independent Q-functions Q_{θ_1} and Q_{θ_2}, taking the minimum estimate for target value computation to reduce overestimation [137]:

$$y = r + \gamma \min_{i=1,2} Q_{\theta_i'}(s', \tilde{a}) \tag{20}$$

where $\tilde{a} = \mu'(s') + \text{clip}(\epsilon, -c, c)$ represents the smoothed target action with clipped noise $\epsilon \sim \mathcal{N}(0, \sigma)$. Policy updates occur less frequently than critic updates (typically every second iteration) to allow critics to converge before policy modification. This delayed update mechanism prevents policy updates from exploiting temporary critic errors. Target policy smoothing adds regularized noise to target actions during critic training, smoothing the value function over similar actions and reducing the impact of function approximation errors [35].

The complete TD3 update procedure alternates between critic training using both networks and periodic actor updates using the first critic network only. Hyperparameter selection follows $\sigma = 0.2$ for target noise, clipping bounds $c = 0.5$, and policy delay factor of 2.

4.4 Gradient-Enhanced Proximal Policy Optimization (GPPO)

GPPO represents a hybrid approach that integrates analytic gradient information from differentiable fluid simulations into the standard PPO framework [14]. This method exploits the differentiability of JAX-based flow solvers to compute exact policy gradients with respect to the flow dynamics, providing more informative gradient signals than traditional finite-difference estimates or likelihood ratio methods [138].

The algorithm combines analytic gradients $\nabla_\theta \mathbb{E}[R(\tau)]$ computed directly through the differentiable simulator with PPO's clipped surrogate objective. The enhanced gradient computation leverages automatic differentiation through the entire simulation trajectory [139]:

$$\nabla_\theta J = \nabla_\theta \mathbb{E}_{\tau \sim \pi_\theta} \left[\sum_{t=0}^{T} R(s_t, a_t) \right] \tag{21}$$

where θ represents the tunable policy parameters, J is the objective, R is the reward, and the expectation gradient is computed analytically through the deterministic fluid dynamics, eliminating variance associated with policy gradient estimation. To provide a more clear example, consider the 3D channel flow, where the objective is to minimize the wall-shear stress, τ_w, and the reward signal was a function of τ_w. At a point in time t, the environment backward pass can compute:

$$\frac{\partial \tau_w}{\partial \theta} = \frac{\partial \tau_w}{\partial s_t} \frac{\partial s_t}{\partial \theta} + \frac{\partial \tau_w}{\partial a_t} \frac{\partial a_t}{\partial \theta} \tag{22}$$

which can be added to the loss term for optimization. This concept was applied to both flow environments, the 3D channel flow and the 2D Kolmogorov flow, to train the GPPO agent.

The implementation maintains PPO's trust region constraints while incorporating these enhanced gradients through a weighted combination scheme. The gradient weighting balances analytic precision with exploration requirements, using adaptive coefficients based on gradient magnitude and policy entropy. Network architectures are specifically designed for JAX compatibility, utilizing Flax layers with consistent initialization schemes across differentiable and non-differentiable components [140].

SI 5 Environments

The HydroGym platform provides a comprehensive suite of fluid dynamics environments specifically designed for reinforcement learning benchmarking and active flow control research. These environments span a diverse range of canonical flow configurations that capture fundamental fluid mechanics phenomena while maintaining computational tractability for iterative RL training processes.

As detailed in Fig. and Tab. SI 1, the framework encompasses 42 distinct flow scenarios across 13 different geometric configurations, ranging from two-dimensional cylinder flows to complex three-dimensional turbulent channel cases. The environments are systematically organized to cover multiple Reynolds number regimes within each configuration, enabling the investigation of flow control strategies across different physical regimes—from laminar vortex shedding at lower Reynolds numbers to transitional and turbulent dynamics at higher values.

The benchmark suite includes both classical bluff body flows (cylinders, squares, cubes, spheres) that exhibit well-documented vortex shedding phenomena as well as more specialized configurations such as cavity flows with shear layer instabilities, NACA 0012 airfoils under gust interactions, extreme events-driven Kolomogorov flows and biomedically-relevant stenotic pipe flows. Additionally, the framework incorporates

multi-agent reinforcement learning (MARL) scenarios for spatially-distributed control strategies and differentiable physics environments (Kolmogorov and channel flows) that enable gradient-based optimization approaches.

Each environment follows a standardized framework that includes configurable reward functions targeting specific control objectives (typically drag reduction and flow stabilization), flexible actuation mechanisms (jet-based control, surface rotation, or temperature modulation), and adaptable sensor configurations through point probe measurements of flow quantities. The temporal coupling between CFD solvers and reinforcement learning agents is carefully calibrated to match characteristic flow timescales while maintaining computational efficiency for training.

The validation status indicators in Table SI 1 demonstrate the current benchmark status across different RL algorithms (PPO, TD3, DDPG, GPPO), with the majority of environments successfully benchmarked

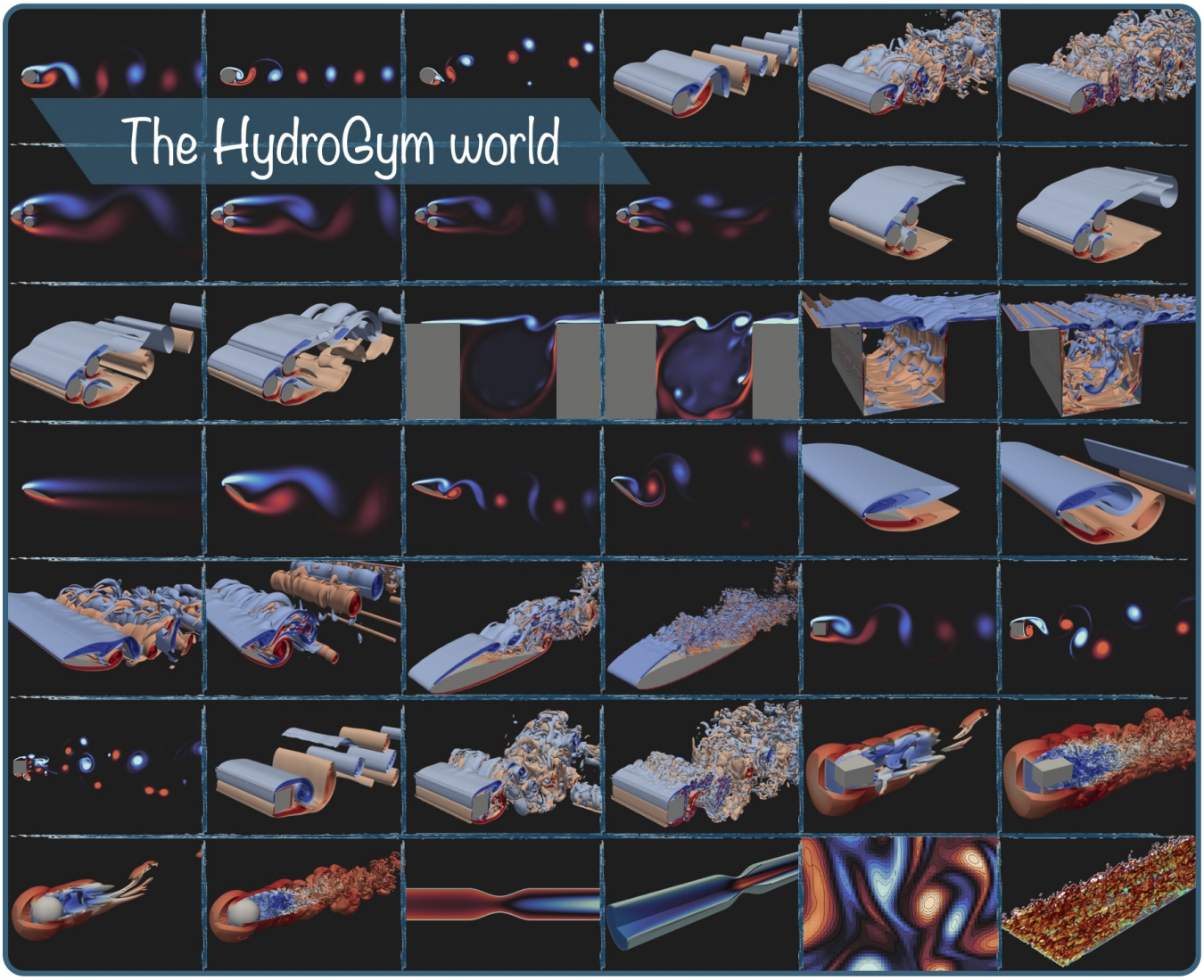

Figure SI 1: The HydroGym Environment Suite and Standardized Interface. The HydroGym platform provides standardized access to over 42 benchmarked fluid dynamics environments through a unified Gymnasium-compatible interface. The comprehensive environment gallery showcases diverse flow configurations spanning two-dimensional and three-dimensional scenarios including cylinder flows, cavity flows, airfoils, channel flows, and turbulent cases across multiple Reynolds number regimes. This standardized approach enables consistent benchmarking and comparison of reinforcement learning algorithms across a vast spectrum of active flow control problems.

using numerous established deep reinforcement learning methods. The systematic organization of these environments provides researchers with a progressive pathway from fundamental flow control problems to increasingly complex multi-physics scenarios, supporting both algorithm development and practical flow control applications. The following subsections provide detailed descriptions of each environment category, including the underlying flow physics, numerical implementation specifics, validation against literature benchmarks, and the specific RL environment setup including state spaces, action spaces, and reward formulations.

It is simple to initialize the environments as environments are configured through a dictionary specifying

Environments	Re # range	Computational domain	Number of cells	Computational method	Objective	Benchmarks			
						PPO	TD3	DDPG	GPPO
2D Cylinder	100	$[40D \times 20D]$ | $[20D \times 10D]$	122,781 | (8,744)	m-AIA | Firedrake	drag reduction wake stabilization	✅	✅	✅	❌
	200	$[40D \times 20D]$	122,781	m-AIA		✅	✅	✅	❌
	1,000	$[40D \times 20D]$	308,856	m-AIA		✅	✅	✅	❌
	3,900	$[40D \times 20D]$	353,768	m-AIA		✅	✅	✅	❌
2D Pinball	30	$[40D \times 20D]$ | $[26D \times 12D]$	170,216 | (25,695)	m-AIA | Firedrake	drag reduction	✅	✅	✅	❌
	75	$[40D \times 20D]$ | $[26D \times 12D]$	170,216 | (25,695)	m-AIA | Firedrake		✅	✅	✅	❌
	100	$[40D \times 20D]$ | $[26D \times 12D]$	170,216 | (25,695)	m-AIA | Firedrake		✅	✅	✅	❌
	150	$[40D \times 20D]$ | $[26D \times 12D]$	170,216 | (25,695)	m-AIA | Firedrake		✅	✅	✅	❌
2D Cavity	4,140	$[2.5H \times 1.25H]$	169,516	m-AIA	shear layer stabilization	✅	✅	✅	❌
	7,500	$[2.5H \times 1.25H]$ | $[3.75D \times 1.25D]$	169,516 | (110,576)	m-AIA | Firedrake		✅	✅	✅	❌
2D Square Cylinder	200	$[40D \times 20D]$	122,786	m-AIA	drag reduction wake stabilization	✅	✅	✅	❌
	1,000	$[40D \times 20D]$	238,400	m-AIA		✅	✅	✅	❌
	3,900	$[40D \times 20D]$	459,584	m-AIA		✅	✅	✅	❌
2D NACA 0012	$Re = 100 \mid \alpha = 20°$	$[33.75c \times 15c]$	145,865	m-AIA	gust mitigation wake stabilization	✅	✅	✅	❌
	$Re = 100 \mid \alpha = 40°$	$[33.75c \times 15c]$	145,881	m-AIA		✅	✅	✅	❌
	$Re = 1,000 \mid \alpha = 20°$	$[33.75c \times 15c]$	145,865	m-AIA		✅	✅	✅	❌
	$Re = 1,000 \mid \alpha = 40°$	$[33.75c \times 15c]$	145,881	m-AIA		✅	✅	✅	❌
2D Stenotic Pipe	100	$[16D \times D]$	25,000	m-AIA		✅	✅	✅	❌
3D Cylinder	200	$[32D \times 16D \times 4D]$	46,033,631	m-AIA	drag reduction wake stabilization	✅	✅	✅	❌
	1,000	$[32D \times 16D \times 4D]$	82,954,157	m-AIA		✅	⏳	⏳	❌
	3,900	$[32D \times 16D \times 4D]$	82,954,157	m-AIA		✅	⏳	⏳	❌
3D Cylinder (MARL)	1,000	$[32D \times 16D \times 4D]$ ($[32D \times 16D \times D]$)	82,954,157	m-AIA	drag reduction wake stabilization	✅	⏳	⏳	❌
	3,900	$[32D \times 16D \times 4D]$ ($[32D \times 16D \times 0.4D]$)	82,954,157	m-AIA		✅	✅	✅	❌
3D Pinball	30	$[32D \times 16D \times 4D]$	57,460,497	m-AIA	drag reduction	✅	✅	✅	❌
	75	$[32D \times 16D \times 4D]$	57,460,497	m-AIA		✅	✅	✅	❌
	100	$[32D \times 16D \times 4D]$	57,460,497	m-AIA		✅	✅	✅	❌
	150	$[32D \times 16D \times 4D]$	57,460,497	m-AIA		✅	✅	✅	❌
3D Cavity	4,140	$[2.5H \times 1.25H \times 2.25H]$	34,990,848	m-AIA	shear layer stabilization	✅	✅	✅	❌
	7,500	$[2.5H \times 1.25H \times 2.25H]$	34,990,848	m-AIA		✅	✅	✅	❌
3D Square cylinder	200	$[32H \times 16H \times 4H]$	81,962,816	m-AIA	drag reduction wake stabilization	✅	✅	✅	❌
	1,000	$[32H \times 16H \times 4H]$	81,962,816	m-AIA		⏳	⏳	⏳	❌
	3,900	$[32H \times 16H \times 4H]$	81,962,816	m-AIA		⏳	⏳	⏳	❌
3D NACA 0012	$Re = 100 \mid \alpha = 20°$	$[32c \times 16c \times 4c]$	34,145,524	m-AIA	gust mitigation wake stabilization	✅	✅	✅	❌
	$Re = 100 \mid \alpha = 40°$	$[32c \times 16c \times 4c]$	34,486,966	m-AIA		✅	✅	✅	❌
	$Re = 1,000 \mid \alpha = 20°$	$[32c \times 16c \times 4c]$	67,645,241	m-AIA		✅	✅	✅	❌
	$Re = 1,000 \mid \alpha = 40°$	$[32c \times 16c \times 4c]$	67,743,775	m-AIA		✅	✅	✅	❌
	$Re = 10,000 \mid \alpha = 12°$	$[32c \times 16c \times 0.5c]$	93,070,696	m-AIA		⏳	⏳	⏳	❌
	$Re = 50,000 \mid \alpha = 12°$	$[32c \times 16c \times 0.5c]$	93,070,696	m-AIA		⏳	⏳	⏳	❌
3D Cube	300	$[32H \times 16H \times 16H]$	32,338,392	m-AIA	drag reduction wake stabilization	⏳	⏳	⏳	❌
	3,700	$[32H \times 16H \times 16H]$	115,965,412	m-AIA		⏳	⏳	⏳	❌
3D Sphere	300	$[32D \times 16D \times 16D]$	40,798,880	m-AIA	drag reduction wake stabilization	⏳	⏳	⏳	❌
	3,700	$[32D \times 16D \times 16D]$	89,649,414	m-AIA		⏳	⏳	⏳	❌
3D Stenotic Pipe	100	$[16D \times D \times D]$	1,000,000	m-AIA		✅	✅	✅	❌
2D Kolmogorov (diff)	40-500	$[2\pi \times 2\pi]$	4,096	JAX	extreme event mitigation increase mixing	✅	⏳	⏳	✅
3D Channel (diff)	$Re_\tau = 180$	$[2\pi \times 2 \times \pi]$	373,248	JAX	reduce wall shear stress	✅	⏳	⏳	✅

Table SI 1: Overview of HydroGym's flow control environments available for reinforcement learning benchmarking. The table catalogs 2D and 3D flow configurations including cylinders, pinball setups, cavity flows, square cylinders, NACA 0012 airfoils, stenotic pipes, cubes, and spheres across various Reynolds numbers (Re - based on the diameter D, cavity height H, cube height H, or the chord length c) and angles of attack (α). Additional environments include multi-agent reinforcement learning (MARL) scenarios and differentiable physics cases (Kolmogorov and turbulent channel flows). Status markers indicate the current benchmarking status. GPPO is exclusively available for JAX environments, as it requires fully differentiable environments to backpropagate gradients with respect to arbitrary input parameters.

flow parameters and instantiated using hydrogym.FlowEnv(), with agents interacting through standard reset() and step() methods :

```
import hydrogym

env_config = {
    "flow": hydrogym.Cavity,
    "solver": hydrogym.MAIA,
    "Re": 7500,
    "observation": 'pressure',
    "probe_locations": probe_locations,
    "configuration_file": './config.yaml',
}

env = hydrogym.FlowEnv(env_config)
```

It is then simple to interact with them:

```
# reset environment
obs, info = env.reset()

# interact with environment
action = 0.0
for _ in range(num_interactions):
    (obs, reward, terminated, truncated, info) = env.step(action)

# close environment
env.terminate_run()
```

5.1 Circular cylinder flow

Characteristic physics. The flow around circular cylinders in the Reynolds number range 200-3,900 based on the cylinder diameter and the free-stream velocity exhibits rich dynamical behavior characterized by distinct regime transitions and complex three-dimensional instabilities that have profound implications for both fundamental fluid mechanics research and practical flow control applications. This transitional range encompasses the evolution from two-dimensional laminar vortex shedding to fully three-dimensional turbulent wakes, presenting unique challenges for modeling, prediction, and control.

The flow physics within this range is governed by two critical transitions that fundamentally alter wake dynamics. The first occurs at Reynolds numbers around 190-200, where the initially two-dimensional von Kármán vortex street undergoes its first three-dimensional instability, known as Mode A. This elliptic instability manifests as large-scale spanwise undulations with characteristic wavelengths of approximately 3-4 cylinder diameters, originating in the primary vortex cores and representing the onset of three-dimensional wake behavior [141, 142]. As the Reynolds number continues to increase beyond $Re = 230 - 260$, a second transition emerges through Mode B instability. Unlike Mode A, this hyperbolic instability develops in the braid shear layers and exhibits much smaller spanwise wavelengths of approximately 0.8-1.0 cylinder diameters [143, 144]. Together, these successive transitions mark the beginning of a complex regime where two-dimensional approximations become progressively inadequate for accurate flow prediction. These three-dimensional instabilities create fundamental differences between 2D and 3D flow configurations that extend well beyond simple geometric considerations. While two-dimensional simulations remain computationally efficient and provide reasonable approximations for basic flow characteristics below $Re = 189$, they fundamentally cannot capture the governing physics once three-dimensional instabilities develop [145]. That is, the spanwise variations introduced by Mode A and Mode B instabilities significantly affect drag

coefficients, vortex shedding frequencies, and heat transfer characteristics, with these effects becoming increasingly dominant as the Reynolds number increases. In the subcritical regime ($Re > 1,000$), the wake transitions to fully turbulent characteristics while maintaining coherent large-scale vortex shedding patterns. This creates a complex interplay between organized and chaotic motion that further challenges traditional modeling approaches [146, 147].

Overall, the rich dynamical behavior has established cylinder wakes as particularly valuable canonical test cases for developing and validating flow control strategies. The combination of the relatively simple geometry with complex physics provides an ideal benchmark for both traditional control methods and emerging machine learning approaches. Recent developments in deep reinforcement learning have demonstrated remarkable success, achieving drag reductions of $8 - 25\%$ using various actuator configurations including synthetic jets, rotational oscillation, and plasma actuators [71, 72]. The Reynolds number range 200-3,900 proves especially well-suited for these applications because the flow exhibits sufficient complexity to challenge control algorithms while remaining computationally tractable for iterative training processes.

However, the practical implementation of flow control in this Reynolds number range faces several specific challenges stemming from the complex transitional flow physics. Three-dimensional instabilities introduce spanwise variations that complicate sensor placement and actuator design, while the coexistence of laminar and turbulent regions creates difficulties in developing robust control strategies. Energy efficiency considerations become particularly critical, as the power required for active control can exceed the benefits gained through drag reduction, especially at lower Reynolds numbers within this range [148]. Furthermore, the sensitivity of the wake behavior to boundary conditions and geometric details makes experimental validation of numerical control studies challenging, often requiring careful attention to computational domain size and boundary condition implementation. To address these challenges, multi-agent deep reinforcement learning frameworks have been designed to target the three-dimensional control problems, though most successful demonstrations remain limited to lower Reynolds numbers within the transitional range [15].

To summarize, the established nature of cylinder wake physics makes this configuration particularly valuable as emerging computational methods and experimental techniques continue to provide new insights into flow control possibilities. The comprehensive understanding of fundamental mechanisms enables researchers to confidently assess whether novel approaches capture the essential physics or merely exploit computational artifacts [9, 149, 150]. Therefore, the well-documented cylinder wake serves as a valuable benchmark scenario for validating new innovations before applying them to more complex geometries and flow physics.

Numerical setup and validation. The cylinder benchmark scenario comprises 2D and 3D low Mach number flows ($Ma < 0.2$) over circular cylinders at different Reynolds number, i.e. $Re \in [100,\ 200,\ 1,000,\ 3,900]$. For the 2D cases, the computational domain is defined by $(x/D, y/D) \in [0, 40] \times [-10, 10]$ with the cylinder being centered at $(x/D, y/D) = (10, 0)$ and x representing the streamwise coordinate direction. The grid spacing is determined by the grid refinement level n via $\Delta_n = \Delta_0/2^n$ with $\Delta_0^{(2D)} = 40D$. Three refinement patches decrease the grid spacing up to a level of $n = 14$, see Fig. SI 2, corresponding to more than 320 cells per cylinder diameter.

In 3D the domain is $(x/D, y/D, z/D) \in [0, 32] \times [0, 16] \times [-2, 2]$, being periodic in the z-direction while the center of the cylinder is located at $(x/D, y/D) = (8, 8)$ and its axis is aligned in z-direction. The grid spacing is defined by $\Delta_0^{(3D)} = 32D$ and refinement levels of $n \in [9, 14]$ resolving the cylinder by 500 grid points.

At the inlet, a Dirichlet boundary condition is implemented with a prescribed constant velocity profile. The velocity vector is read from the properties file and applied uniformly across the inlet cross-section. The density at the inlet boundary cells is extrapolated from the interior domain using second-order accurate extrapolation to maintain consistency with the low Mach number assumption. The equilibrium distribution functions are calculated based on the prescribed velocity and extrapolated density values.

(a) $Re = 200$

Reference	St	$\overline{C_D}$	$\overline{C_L}$
Present study	**0.196**	**1.341**	**±0.659**
Meneghini et al.[151]	0.196	1.30	–
Ding et al.[152]	0.196	1.348	±0.659
Braza et al.[153]	0.200	1.40	±0.75
Posdziech & Grundmann[154]	0.194	1.311	±0.66
Harichandan & Roy[155]	0.192	1.32	±0.602

(b) $Re = 1,000$

Reference	St	$\overline{C_D}$	$\overline{C_L}$
Present study	**0.234**	**1.533**	**±1.449**
Colagrossi et al.[156]	0.231	1.507	±1.457
Durante et al.[157]	0.235	1.491	±1.46
Scott & Durst[158]	0.2276	1.54	±1.225
Chatzimanolakis et al.[19]	–	1.61	–
von Wahl et al.[159]	0.23	1.53	–

(c) $Re = 3,900$

Reference	St	$\overline{C_D}$	$\overline{C_L}$
Present study	**0.21**	**1.68**	**±1.61**
Chatzimanolakis et al.[19]	–	1.75	–
Durante et al.[157] ($\mathrm{Re} = 1 \times 10^4$)	0.19	1.98	±1.73

Table SI 2: Validation of 2D cylinder flow results at different Reynolds numbers. St: Strouhal number; $\overline{C_D}$: Time-averaged drag coefficient; $\overline{C_L}$: Time-averaged lift coefficient; ±: Oscillation amplitude; –: Data not reported or not applicable

(a) $Re = 200$

Reference	St	$\overline{C_D}$	$C_{L'}$
Present study	**0.192**	**1.318**	**0.418**
Qu et al.[160]	0.183	1.25	0.35
Posdziech & Grundmann[161]	0.182	1.24	–
Carmo & Meneghini[162]	0.184	1.28	–
Labbé & Wilson[163]	0.195	1.318	–
Behara & Mittal[164]	0.195	1.38	–
Rajani et al.[165]	0.1936	1.338	0.4276

(b) $Re = 1,000$

Reference	St	$\overline{C_D}$	$C_{L'}$
Present study	**0.213**	**1.102**	**0.374**
Tong et al.[166]	0.215	1.08	0.2
Lei et al.[167]	–	1.112	0.325
Labbé & Wilson[163]	0.215	1.200	–
Zhao et al.[168]	0.21	1.17	0.335

(c) $Re = 3,900$

Reference	L_z	St	$\overline{C_D}$
Present study	**4.0**	**0.217**	**1.074**
Suárez et al.[32]	π	0.220	1.08
Lehmkuhl et al.[169]	π	0.215	1.015
Parnaudeau et al.[146]	23	0.208	–
Tremblay et al.[170]	π	0.22	1.03
Kravchenko & Moin[147]	π	0.21	1.04

Table SI 3: Comparison of 3D cylinder flow results at different Reynolds numbers. St: Strouhal number; $\overline{C_D}$: Time-averaged drag coefficient; $C_{L'}$: RMS lift coefficient; L_z: Span length; L_r/D: Recirculation length to diameter ratio; –: Data not reported or not applicable

At the outlet, non-reflecting boundary conditions are applied minimizing spurious wave reflections. The velocity components are extrapolated from the interior domain using von Neumann conditions (zero normal gradient). The density is computed using a non-reflecting formulation:

$$\rho = \frac{\rho_{\text{old}} + \rho_{\text{ref}}/c_s(|\vec{v}| - |\vec{v}_{\text{old}}|) + \alpha \Delta t \rho_{\text{ref}}}{1 + \alpha \Delta t} \tag{23}$$

where ρ_{old} and $\vec{v}_{\text{old}}$ are values from the previous time step, c_s is the speed of sound, ρ_{ref} is a reference density term that can be specified as either density fluctuations or absolute density depending on the simulation requirements, and $\alpha = 1.0$ is the relaxation parameter.

Periodic boundary conditions are applied to the lateral boundaries (side walls) of the computational domain. This treatment ensures mass conservation and eliminates the need for additional boundary condition specifications at these surfaces, effectively creating an infinite domain in the lateral directions.

Based on a comprehensive validation study, our numerical simulations demonstrate good agreement with established literature values across multiple Reynolds numbers and flow configurations. For 2D cylinder flows, our results closely match reference data, with Strouhal numbers within $1-3\%$ of published values and drag coefficients typically within 5% of established benchmarks. The 3D simulations show similarly strong validation, with our Strouhal numbers and drag coefficients falling well within the scatter of literature values across all tested Reynolds numbers. The close correspondence between our computed flow parameters and the extensive reference database confirms the accuracy and reliability of our numerical approach for cylinder flow simulations.

Environment setup. The default reward objective r for the cylinder flow environment targets drag minimization and the reduction of lift force oscillations and reads $r = -|C_D| - \omega|C_L|$, where C_D, C_L denote the normalized drag and lift coefficients, and ω is a Reynolds number-dependent scaling factor with values of 0.1, 0.2, 1.0, and 1.0 for $Re = 100,\ 200,\ 1,000,\ 3,900$, respectively. Since the unstable symmetric state is also the minimum-drag configuration, this objective corresponds to stabilizing this unstable fixed point. This reward formulation serves as the default configuration, though additional reward shaping terms can be easily implemented by users according to their specific research objectives.

Two different actuation strategies are implemented to provide the RL agent with control authority over

the flow dynamics. First, a zero-net mass-flux blowing/suction strategy is provided, comprised of two equal and opposite jets - one at the top and one at the bottom of the cylinder. The RL agent controls the mass flux of the upper jet, which automatically specifies the lower jet through the zero-net-mass constraint. In the default configuration, the jets are placed at 90° and 270° positions and cover 10° of the cylinder circumference each, though the HydroGym framework is designed to allow for flexible user-specified adjustments of the jet number, placement angles, and coverage areas. Second, a rotating surface actuator is implemented for which the RL agent directly controls the angular velocity of the cylinder surface. Both action spaces are normalized to the range $[-1, 1]$ to ensure consistent RL algorithm performance across different actuation modes.

The environment supports both two-dimensional and three-dimensional cylinder flow configurations across multiple Reynolds numbers ($Re = 100,\ 200,\ 1,000,\ 3,900$), enabling the investigation of flow control across different flow regimes from laminar vortex shedding to fully turbulent conditions. For three-dimensional cases at $Re = 1,000$ and $3,900$, the framework additionally supports multi-agent reinforcement learning through spanwise domain decomposition, where the cylinder is divided into 4 and 10 subcylinder segments respectively, each individually controlled by a dedicated agent. This multi-agent approach enables the investigation of cooperative control strategies and spanwise flow coordination. The framework provides flexibility in multi-agent coordination, allowing agents to share gradient information and experience buffer data if desired, though independent agent operation is also supported based on user requirements.

The state space representation consists of user-configurable point probes distributed throughout the computational domain, providing measurements of velocity components, pressure, density, and body forces at specified locations. By default, the state observations consist of the raw solver output, but different normalization strategies are implemented to normalize the state space in the range $[-1, 1]$ for consistent RL training performance. This flexible sensor configuration allows the investigation of minimal sensing strategies and optimal sensor placement for effective flow control.

Each training episode spans 200 control actions, corresponding to approximately 10 vortex shedding periods, providing sufficient time for the agent to observe and respond to flow dynamics. The temporal coupling between the CFD solver and RL agent employs Reynolds number-specific action frequencies: 200, 350, and 600 CFD timesteps per control action for 2D cases at $Re = 200,\ 1,000,\ 3,900$ respectively, and 400, 500, and 1,200 timesteps for corresponding 3D cases. These ratios are designed to match the characteristic timescales of vortex shedding dynamics while maintaining computational efficiency and control authority.

The environment framework provides a comprehensive testbed for investigating reinforcement learning-based active flow control strategies, supporting both fundamental research into control mechanisms and practical development of sensing and actuation approaches for cylinder wake management. All described configurations represent default settings that can be easily modified by users to accommodate specific research requirements, including custom reward functions, alternative actuation strategies, modified sensor placements, and adjusted temporal coupling parameters.

5.2 Fluidic pinball flow

Characteristic physics. The fluidic pinball serves as an exemplary test case for investigating complex wake dynamics and flow control strategies in transitional flow regimes. This benchmark configuration consists of three equal-diameter circular cylinders positioned at the vertices of an equilateral triangular arrangement, with one vertex directed toward the incoming flow [171]. Although geometrically simple, this arrangement demonstrates a diverse spectrum of nonlinear flow behaviors, including steady-state solutions, time-periodic oscillations, quasi-periodic motion, and fully chaotic dynamics across different operating parameters.

The fluidic pinball exhibits distinct flow regime transitions as the Reynolds number varies from 30 to 150, with critical thresholds that differ from classical single-cylinder wake behavior. Initial investigations by [172] identified specific transition points unique to this multi-cylinder configuration. For Reynolds numbers below $\mathrm{Re} < 18$, the flow field maintains global stability with symmetric recirculation zones forming downstream of the cylinder cluster. The transition from this steady state occurs via a supercritical Hopf bifurcation at

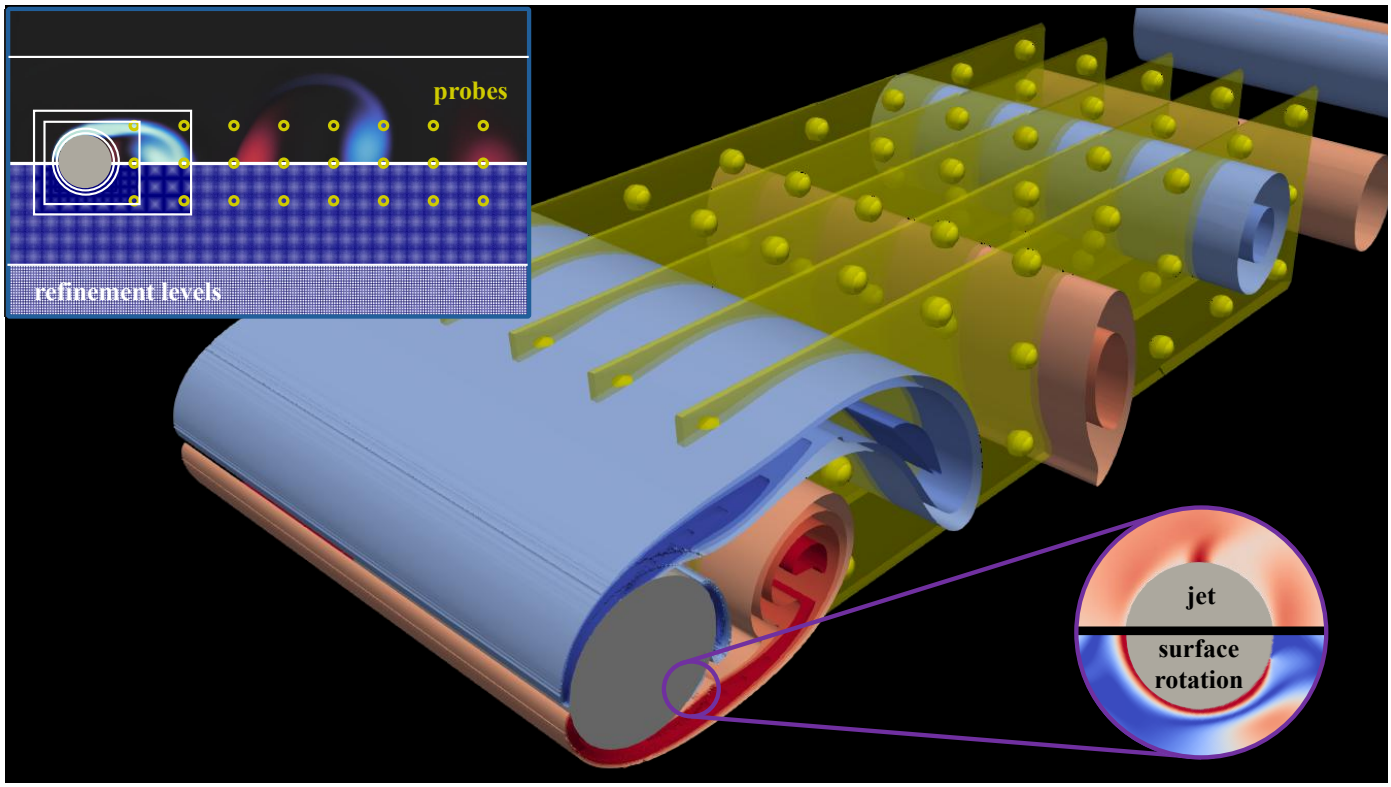

Figure SI 2: Computational domain setup, sensor probe distribution and actuation strategy for the circular cylinder flows: Three-dimensional view showing the probe distribution around the cylinder setup with vortical structures visualized through Q-criterion isosurfaces. The yellow dots in the zoom-in highlight sensor probe locations in a single spanwise plane. Active flow control is either performed using jet actuators positioned at the top and bottom of the cylinder or via surface rotation.

approximately $Re = 18$ [172]. This early onset of instability results from the enhanced wake interactions between the three cylinders. The Hopf bifurcation introduces time-periodic vortex shedding characterized by complex conjugate eigenvalues crossing the stability boundary in the linearized flow equations. The resulting flow exhibits von Kármán-type vortex shedding with dimensionless frequency (Strouhal number) of approximately 0.2. Importantly, this initial instability preserves the mirror-plane symmetry about the configuration centerline, maintaining symmetric shedding patterns until $Re \approx 68$.

At $Re \approx 68$, the fluidic pinball undergoes a second critical transition through a supercritical pitchfork bifurcation [173]. This transition fundamentally alters the wake dynamics by breaking the mirror symmetry preserved during the initial periodic regime. The physical mechanism involves the destabilization of the jet flow between the two downstream cylinders, which becomes susceptible to preferential deflection in either the upward or downward direction. This symmetry-breaking creates two mirror-symmetric stable solutions - one with upward jet deflection and another with downward deflection. The system exhibits bistable behavior, where initial conditions determine which asymmetric state the flow adopts [173]. This represents a qualitative change from the previous symmetric periodic shedding to asymmetric limit cycle dynamics.

Beyond $Re = 104$, the fluidic pinball system develops additional complexity through a secondary Neimark-Sacker bifurcation [174]. This mathematical bifurcation introduces quasi-periodic motion by creating torus-like attractors in the system's phase space. The primary vortex shedding frequency becomes modulated by secondary low-frequency oscillations, establishing multi-frequency dynamics characteristic of weakly chaotic flows. The transition to fully chaotic motion occurs above $Re \approx 130$, following what was identified by [174] as a Newhouse-Ruelle-Takens scenario. In this Re number regime, the quasi-periodic torus structure

becomes unstable and breaks down, leading to aperiodic motion with sensitive dependence on initial conditions - the hallmark of deterministic chaos.

Moreover, three-dimensional effects can introduce additional complexity beyond the two-dimensional analysis. Following the foundational work of [141] on cylinder wake transitions, the fluidic pinball exhibits spanwise instabilities originating from hyperbolic regions within the braid shear layers. These instabilities manifest as short-wavelength structures with characteristic spanwise dimensions comparable to the cylinder diameter. The three-dimensional modes create streamwise vortical structures that interact with the primary cross-stream vortex shedding. Multiple instability modes can coexist and compete, leading to complex scenarios including cooperative destabilization and vortex reconnection phenomena that cannot be captured by two-dimensional computational models.

To summarize, the fluidic pinball's value as a benchmark derives from the combination of geometric simplicity and dynamical richness, making it suitable for testing advanced control strategies while remaining computationally tractable. The independent rotation capability of each cylinder provides multiple actuation inputs, enabling implementation of various flow control mechanisms established in the literature. Classical flow control approaches applicable to this configuration include boundary layer manipulation through surface blowing (analogous to base bleeding techniques), high-amplitude periodic forcing for vortex synchronization, and circulation control via cylinder rotation utilizing Magnus force effects. Additionally, modern approaches such as opposition control and model-based feedback strategies can be evaluated.

Hence, the fluidic pinball presents several fundamental challenges for flow control design. The succession of bifurcations means that control strategies must adapt to qualitatively different flow physics as operating conditions change. Systems designed for the symmetric periodic regime may prove ineffective or counterproductive when applied to the asymmetric bistable regime. The multi-frequency dynamics create coupling between different temporal scales, where actuation at one frequency can influence the entire spectral content of the flow response. This cross-frequency coupling necessitates control architectures that account for broadband nonlinear interactions rather than targeting individual frequency components. Furthermore, the presence of multiple coexisting attractors (in the bistable regime) and hysteresis effects between flow states require control strategies capable of managing state transitions and maintaining desired operating points despite external disturbances.

Extension to three-dimensional control introduces requirements for spanwise-distributed actuation to address the various three-dimensional instability modes. The transition between different three-dimensional regimes creates scenarios where two-dimensional control approaches become inadequate, necessitating fundamentally different control frameworks. Control strategies optimized for one three-dimensional mode may lose effectiveness or become destabilizing when the flow transitions to alternative modal states. This highlights the importance of robust adaptive control approaches that maintain performance across regime boundaries.

Numerical setup and validation. The fluidic pinball configuration consists of three circular cylinders arranged in an equilateral triangle formation, creating a fundamentally different flow topology compared to the single cylinder case. Relative to the pinball center at $(x/D, y/D) = (10.0, 0.0)$ for the 2D simulations and $(8.0, 0.0)$ for the 3D counterpart, the cylinders are positioned with centers at $(x/D, y/D) = (-1.299, 0.0)$, $(0.0, 0.75)$, and $(0.0, -0.75)$, where the upstream cylinder interacts with two downstream cylinders to generate complex wake dynamics and vortex interactions.

The computational setup employs the same domain dimensions and boundary condition treatments as described for the single cylinder benchmark. However, the fluidic pinball operates at lower Reynolds numbers $Re \in [30, 100, 150]$, allowing for a uniform refinement strategy with $n = 12$ across all cases. This refinement level provides adequate resolution to capture the intricate flow features arising from the multi-cylinder interaction, including wake merging, vortex pairing, and the characteristic frequency modulation effects.

The triangular arrangement leads to inherently asymmetric flow patterns, where the downstream cylinders experience different flow conditions due to their positioning relative to the upstream cylinder's wake. This asymmetry manifests in the lift coefficient distributions and requires careful validation against established benchmarks to ensure accurate representation of the flow physics. Validation results are summarized in Table SI 4, demonstrating good agreement with the reference data of Wang et al. [175]. The simulations accurately predict the natural frequencies across all Reynolds numbers. The time-averaged drag coefficients show good agreement (within 2% deviation), while the asymmetric lift coefficients on the downstream cylinders are well-captured, confirming a proper resolution of the wake interaction dynamics. The 3D results maintain similar accuracy levels, validating the three-dimensional extension of the fluidic pinball configuration.

Re	Reference	Dim	f_0	$\overline{C_D}$	$\overline{C_{L,2}}$	$\overline{C_{L,3}}$
30	**Present study**	**2D**	**0.064**	**2.651**	**-0.361**	**0.361**
	Present study	**3D**	**0.061**	**2.597**	**-0.358**	**0.359**
	Wang et al.[175]	2D	0.065	2.656	-0.365	0.365
100	**Present study**	**2D**	**0.088**	**2.904**	**-0.079**	**0.110**
	Present study	**3D**	**0.087**	**2.795**	**-0.0107**	**0.119**
	Wang et al.[175]	2D	0.090	2.874	-0.0745	0.108
150	**Present study**	**2D**	**0.120**	**2.922**	**-0.0441**	**0.0330**
	Present study	**3D**	**0.113**	**2.949**	**-0.0467**	**0.0297**
	Wang et al.[175]	2D	0.118	2.960	-0.043	0.0319

Table SI 4: Validation of the fluidic pinball flow results at different Reynolds numbers. Dim: Dimensionality (2D/3D); f_0: Natural frequency; $\overline{C_D}$: Time-averaged drag coefficient; $\overline{C_{L,i}}$: Time-averaged lift coefficient for cylinder i

Environment setup. The fluidic pinball environment features a multi-cylinder flow control setup comprising three circular cylinders positioned in an equilateral triangular arrangement. The primary reward function r for the fluidic pinball targets total drag reduction across all three cylinders and is defined as $r = -|\sum_{i=1}^{3} C_{D,i}| - \omega|\sum_{i=1}^{3} C_{L,i}|$, where $C_{D,i}$ represents the normalized drag coefficient of cylinder i and $\omega = 1.0$ serves as the scaling parameter consistently applied across all Reynolds numbers to avoid control policies that introduce a significant lift generation. Users can readily adapt this reward structure to explore different objectives including thrust control or independent cylinder optimization.

The control mechanism employs surface rotation actuation, where the RL agent manages the angular velocity of each cylinder individually (see Fig. SI 3). This creates a three-dimensional continuous action space with components bounded within $[-1, 1]$, facilitating exploration of cooperative multi-cylinder control approaches. Although jet-based actuation is not part of the standard setup, the framework design accommodates user integration of blowing/suction mechanisms for extended research applications or comparative analysis.

The framework encompasses both two-dimensional and three-dimensional fluidic pinball flow scenarios across various Reynolds numbers ($Re = 30, 75, 100, 150$), covering flow regimes from steady symmetric configurations through periodic vortex shedding to bistable asymmetric behavior and quasi-periodic dynamics. This Reynolds number spectrum encompasses the distinctive bifurcation characteristics of the fluidic pinball, including the initial Hopf bifurcation at $Re \approx 18$, the symmetry-breaking pitchfork bifurcation at $Re \approx 68$, and progressive transitions toward chaotic flow patterns. The setup utilizes a single-agent configuration, where one agent manages all three cylinder rotations concurrently, promoting research into unified control methodologies for multi-body flow applications.

The observation space utilizes the same adaptable probe-based methodology as established in other environments, featuring user-definable point measurements of velocity components, pressure, density, and body forces positioned throughout the computational domain. Training episodes encompass 200 control actions, equivalent to roughly 10 vortex shedding cycles, offering an adequate temporal scope for agents to perceive and react to the intricate multi-frequency behavior inherent in the fluidic pinball. The CFD-RL coupling utilizes Reynolds number-dependent action intervals tailored to match evolving flow characteristics: 230, 190, 170, and 100 CFD timesteps per control action for 2D scenarios at $Re = 30, 75, 100, 150$ respectively, with corresponding 3D cases using 250, 235, 225, and 200 timesteps. These intervals adapt to the changing temporal scales and flow complexity encountered as the system progresses through distinct dynamical states, maintaining suitable control responsiveness while preserving computational tractability. All outlined

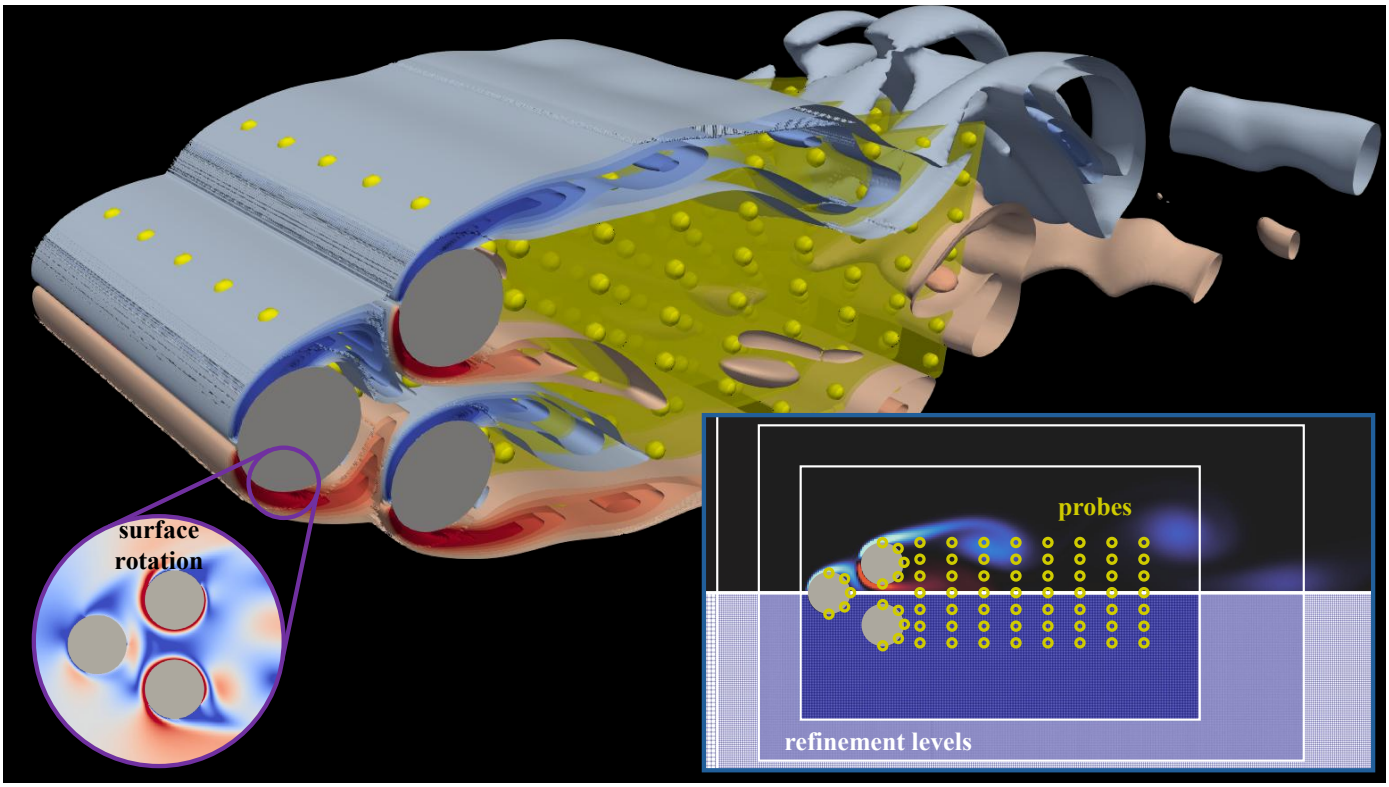

Figure SI 3: Computational domain setup, sensor probe distribution and actuation strategy for the fluidic pinball environment: Three-dimensional view showing the probe distribution around the fluidic pinball with vortical structures visualized through Q-criterion isosurfaces. The yellow dots in the zoom-in highlight sensor probe locations in a single spanwise plane. Active flow control is performed by individual surface rotation of each cylinder.

specifications serve as baseline configurations that users can readily adjust to meet particular research needs, encompassing modified reward structures, alternative control mechanisms, customized sensor layouts, and tailored temporal coupling settings.

5.3 Open cavity flow

Characteristic physics. The flow around open cavities in the Reynolds number range 4,000-7,500 based on the cavity height and the freestream velocity exhibits complex transitional behavior characterized by distinct regime evolutions and sophisticated three-dimensional instabilities that have profound implications for both fundamental aeroacoustics research and practical flow control applications. This transitional range encompasses the evolution from predominantly steady two-dimensional recirculation patterns to complex three-dimensional unsteady dynamics with strong acoustic coupling, presenting unique challenges for modeling, prediction, and control that distinguish it from both lower and higher Reynolds number regimes.

Within this Reynolds number range, the flow physics is governed by several critical transitions that fundamentally alter the cavity dynamics and acoustic characteristics. At Reynolds numbers around 4,000-5,000, the initially stable two-dimensional recirculation undergoes its first significant three-dimensional instability through centrifugal mechanisms arising from curved streamlines in the recirculation region [176, 177]. This transition manifests as weakly unsteady flow behavior with emerging spanwise variations that mark the onset of complex temporal dynamics. As the Reynolds number continues to increase, a second critical transition occurs around Re = 7,000-8,000, where strong temporal instabilities emerge through Hopf bifurcation characteristics, introducing multiple competing temporal modes and mode-switching phenomena

where different frequencies compete for energy [178]. These successive transitions create a regime where simplified two-dimensional approximations become progressively inadequate for an accurate prediction of both aerodynamic and acoustic behavior.

The emergence of these transitional instabilities creates fundamental differences between 2D and 3D cavity flow configurations that extend far beyond geometric considerations. While two-dimensional simulations remain computationally efficient and provide valuable insights into fundamental feedback mechanisms, they systematically overpredict cavity tone amplitudes by up to 15 dB compared to three-dimensional cases and miss critical mixing processes that govern realistic flow physics [179]. The three-dimensional effects introduce end-wall influences that cause flow spillage over cavity sides, development of Taylor-Görtler-like vortices, and breakdown of coherent shear layer structures due to spanwise instabilities. In compressible flows within this Reynolds number range, the acoustic feedback mechanisms become particularly complex, with the classical Rossiter formula requiring depth-sensitized modifications to account for three-dimensional cavity effects and modified convection velocities [180, 181].

This rich transitional behavior makes cavity flows particularly valuable as canonical test cases for developing and validating advanced flow control strategies, especially those employing machine learning approaches. The geometric simplicity combined with complex physics provides an ideal benchmark that bridges fundamental research and practical aerodynamic applications. Various frameworks have provided theoretical foundations for understanding the underlying bifurcation mechanisms and sensitivity characteristics that govern cavity flow transitions [176]. However, the practical implementation of flow control in this Reynolds number range faces several specific challenges that stem from the complex transitional flow physics and multi-frequency acoustic coupling. The strong nonlinear coupling between Rossiter modes creates frequency cross-talk and triadic interactions that complicate traditional linear control approaches, while mode-switching regimes introduce time-varying dynamics that challenge adaptive control systems [182]. Multiple time scales ranging from fast Kelvin-Helmholtz instabilities to slow mode-switching phenomena create complex control requirements, with real-time implementation demanding computational capabilities supporting control frequencies up to 10 kHz. Energy efficiency considerations become particularly critical in practical applications, as the spatially disjoint measurement and control locations inherent in cavity flows introduce time-delay effects that can destabilize feedback control systems if not properly addressed [183].

As a result, the rich transitional physics and computational accessibility make cavity flows in this Reynolds number range an enduring benchmark for flow control innovation, particularly as machine learning approaches mature and computational resources continue to expand.

Numerical setup and validation. The open cavity benchmark comprises 2D and 3D low Mach number flows ($Ma < 0.2$) over square cavities at Reynolds numbers $Re_D \in [4,140,\ 7,500]$, based on the cavity depth D and free-stream velocity U_∞, following the configuration of Barbagallo et al. [178]. For the 2D case, the computational domain is defined by $(x/D, y/D) \in [0.0, 2.5] \times [0, 1.5]$ with the square cavity located at $(x/D, y/D) \in [0.27, 1.27] \times [0, 1]$. The grid spacing is determined by the grid refinement level n via $\Delta_n = \Delta_0/2^n$ with $\Delta_0^{(2D)} = 2.5D$.

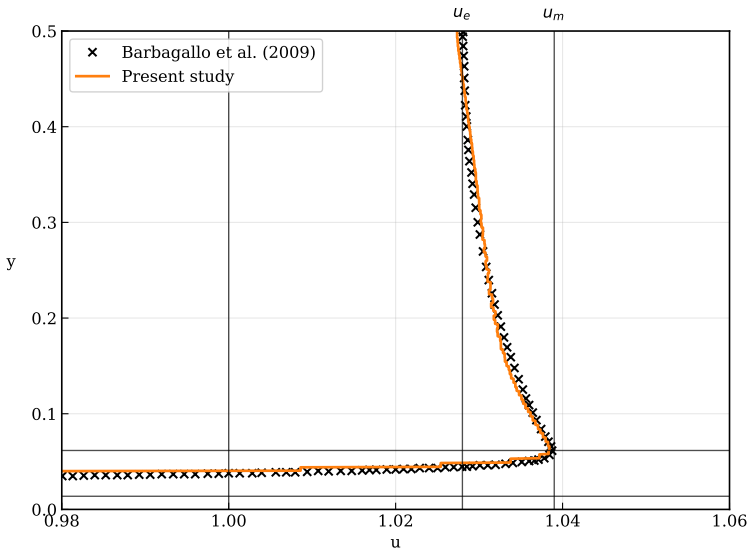

Figure SI 4: Time-averaged leading edge velocity profiles for 2D cavity flow at $Re = 7,500$. Present numerical results (solid line) compared with Barbagallo et al. (2009) [178] reference data (crosses). Velocities normalized by free-stream velocity; vertical coordinate normalized by cavity length.

Multiple refinement patches are employed with maximum refinement levels of $n = 12$ near the cavity edges and shear layer regions, corresponding to approximately 227 cells per cavity depth (see Fig. SI 5). Special attention is given to resolving the boundary layer upstream of the cavity, targeting a displacement thickness of $\delta_1 \approx 0.012D$. This numerical setup demonstrates good agreement with established literature [178] as shown in Fig. SI 4. In 3D, the domain extends to $(x/D, y/D, z/D) \in [0.0, 2.5] \times [0, 1.5] \times [0, 2.25]$ with periodic boundary conditions applied in the spanwise z-direction. A similar grid compared to the 2D test case is used to maintain adequate resolution of three-dimensional instabilities while keeping computational costs manageable.

At the inlet, a Dirichlet boundary condition implements a uniform velocity profile $(u, v, w) = (U_\infty, 0, 0)$. The top boundary implements symmetry conditions $(\partial_y u = 0, v = 0, \partial_y w = 0)$. No-slip conditions $(u = v = w = 0)$ are applied on the cavity walls and the bottom surface from $x/D = 0.1777$ onwards, while symmetry conditions are used for $x/D < 0.1777$ to generate appropriate boundary layer development.

Environment setup. The open cavity environment features a flow control setup designed to stabilize the inherent shear layer instability of cavity flows. This configuration provides a consistent framework across both 2D and 3D flow scenarios, enabling comprehensive investigation of the cavity flow dynamics and active control strategies.

The primary objective centers on minimizing flow fluctuations through targeted stabilization of the shear layer that develops across the cavity opening. The reward function r quantifies this stabilization goal as:

$$r = -\sum_i \left(\frac{\text{obs}_i - \text{target}_{mean,i}}{\text{target}_{std,i}} \right)^2 \tag{24}$$

where obs_i represents the observed quantity at measurement location i, $\text{target}_{mean,i}$ denotes the target reference value, and $\text{target}_{std,i}$ provides normalization scaling. This formulation encourages the control system to maintain observed flow quantities close to their target states, thereby reducing the amplitude of shear layer oscillations and associated cavity resonance phenomena. For simplicity, the target system state is approximated by a temporal mean over 1,000 instability cycles.

The control mechanism employs jet-based actuation strategically positioned to influence the shear layer development and cavity flow dynamics. The standard configuration utilizes a single jet oriented in the y-direction and located at the cavity leading edge, providing direct interaction with the separating boundary layer. For enhanced control authority, an extended configuration incorporates additional jets positioned within the cavity at coordinates $(1.277, 0.75)$ and $(0.277, 0.5)$ that act in streamwise direction, enabling multi-point flow manipulation and improved stabilization capabilities.

The jet actuation creates a continuous action space where the RL agent controls the jet momentum coefficients or velocity ratios. This setup facilitates exploration of both passive flow stabilization through steady jet injection and active control strategies involving time-varying actuation patterns. The framework design readily accommodates user modifications to jet positioning, orientation, and actuation parameters to investigate alternative control approaches or cavity geometries.

The CFD-RL coupling employs 400 CFD timesteps per control action for 2D test cases and 375 timesteps for 3D counterparts, providing sufficient temporal resolution to capture the essential flow physics while maintaining computational efficiency. This interval balances the need to resolve the characteristic timescales of cavity flow instabilities with practical training considerations, allowing the control agent adequate time to observe the effects of its actions on the flow field evolution. Training episodes are designed to encompass multiple characteristic flow timescales, enabling agents to learn both short-term stabilization responses and longer-term flow management strategies. The environment supports the investigation of various Reynolds numbers and cavity aspect ratios, accommodating research into the Reynolds number dependence of control effectiveness and the geometric sensitivity of stabilization approaches.

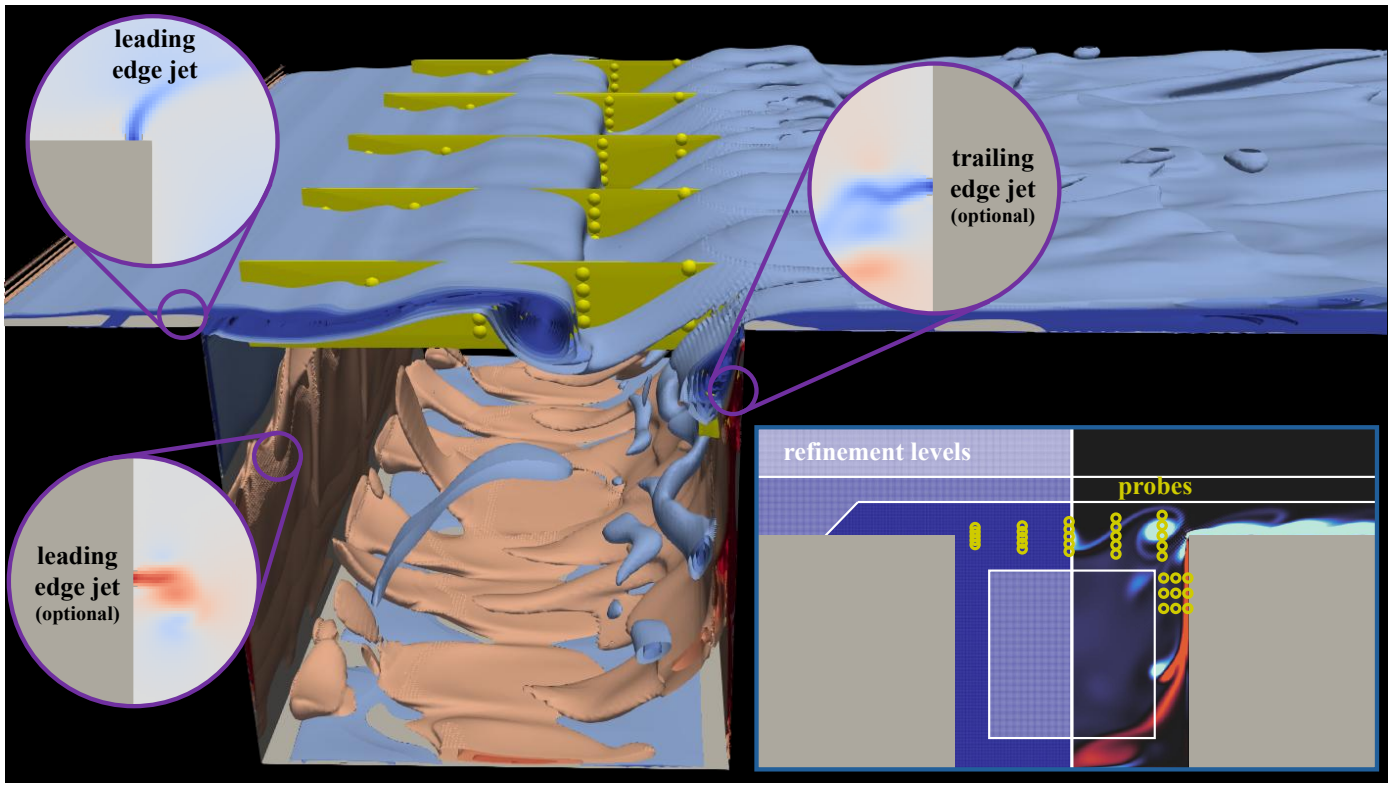

Figure SI 5: Computational domain setup, sensor probe distribution and actuation strategy for the open cavity flow: Three-dimensional view showing the probe distribution in the open cavity environment with vortical structures visualized through Q-criterion isosurfaces. The yellow dots highlight sensor probe locations in a single spanwise plane. Active flow control is performed using up to three independent jet actuators positioned at the leading edge and inside the cavity.

5.4 Square cylinder flow

Characteristic physics. The flow around a square cylinder represents a canonical configuration for studying bluff body aerodynamics, providing fundamental insights relevant to both scholarly inquiry and a wide range of engineering applications, including the design of buildings, bridges, and offshore structures. The interaction of the fluid with the sharp corners of the cylinder forces flow separation, leading to the formation of an unsteady wake dominated by the periodic shedding of large-scale vortices [141]. This alternating vortex shedding generates fluctuating aerodynamic forces on the body, which can induce structural vibrations—a phenomenon termed vortex-induced vibration—posing a significant risk of material fatigue and creating acoustic noise.

The dynamics of the flow are highly dependent on the Reynolds number, and within the range of 200 to 3,900, the wake undergoes a series of complex transitions from a two-dimensional laminar state to a fully three-dimensional turbulent one. The initial transition from a purely two-dimensional to a three-dimensional wake occurs at a critical Reynolds number between approximately 150 and 200 [184, 185]. This transition is marked by the emergence of spanwise instabilities, akin to those observed in circular cylinder wakes. The first of these is the Mode A instability, which appears around $\mathrm{Re} \approx 165$ and is characterized by the formation of large-scale streamwise vortex loops with a spanwise wavelength of about four to five times the cylinder diameter [185, 186]. As the Reynolds number increases further, a transition to the Mode B instability occurs around $\mathrm{Re} \approx 210$, which involves smaller-scale, rib-like streamwise vortices with a much shorter spanwise wavelength of approximately one cylinder diameter [186]. Beyond these initial instabilities, for Reynolds

numbers approaching and exceeding 1,000, the separated shear layers themselves become unstable, leading to the roll-up of Kelvin-Helmholtz vortices which subsequently break down into finer turbulent structures [187]. At higher Reynolds numbers the wake is fully turbulent and characterized by a broad spectrum of interacting eddies [187, 188].

Significant distinctions exist between the flow around square and circular cylinders, primarily stemming from the nature of the flow separation. The sharp corners of the square cylinder fix the separation points, whereas for a circular cylinder, these points are mobile and their location depends on the Reynolds number [189]. This fixed separation generally leads to a wider, more pronounced wake and a higher overall drag coefficient for the square cylinder under identical inflow conditions [190]. While the wake instability modes are qualitatively similar, their onset and development occur at different critical Reynolds numbers. The differences between 2D and 3D configurations are also profound; two-dimensional simulations are incapable of capturing the physics of spanwise instabilities and the resulting energy cascade to smaller turbulent scales. Consequently, 2D models often yield inaccurate predictions of aerodynamic forces and wake dynamics for Reynolds numbers beyond the onset of three-dimensionality [184].

The complex, multi-scale nature of this flow presents considerable challenges for numerical modeling. Reynolds-Averaged Navier-Stokes (RANS) models often fail to accurately predict the highly unsteady and separated flow, particularly the subtle dynamics of vortex shedding and turbulent transition [191]. Scale-resolving approaches, such as Large Eddy Simulation (LES) and Direct Numerical Simulation (DNS), are better suited but are computationally intensive. Achieving accurate results with these methods requires not only extremely fine computational meshes but also large domain sizes and long integration times to ensure that the statistics are fully converged and free from boundary condition influences [187, 192].

These well-defined yet complex flow characteristics make the square cylinder an important test case for the development and validation of flow control strategies, including those leveraging advanced RL techniques. Key challenges for applying RL in this context include the high computational cost of simulations required for training, which can limit the exploration of the solution space, and the persistent difficulty of transferring control policies learned in simulation to real-world experimental setups.

Numerical setup and validation. The square cylinder benchmark follows the same computational setup as the circular cylinder case described above, with the key difference being the bluff body geometry. The square cylinder has a side length D and the Reynolds number is based on this characteristic length, i.e. $Re \in [200,\ 1,000,\ 3,900]$.

The computational domains, grid spacing definitions, and refinement strategies remain identical to the circular cylinder configuration. For 2D cases, the domain spans $(x/D, y/D) \in [0, 40] \times [-10, 10]$ with the square cylinder centered at $(x/D, y/D) = (10, 0)$. The 3D domain is $(x/D, y/D, z/D) \in [0, 32] \times [0, 16] \times [-2, 2]$ with the square cylinder centered at $(x/D, y/D) = (8, 8)$ and periodic boundary conditions in the z-direction as shown in Fig. SI 6.

All boundary condition implementations—inlet Dirichlet conditions with prescribed velocity profiles, non-reflecting outlet conditions, and periodic lateral boundaries—are applied identically to the circular cylinder setup. The grid refinement levels up to $n = 14$ and the resolution criteria also follow the same specifications as detailed in the previous subsection resulting in 512 cells per side length D.

Our validation results for the square cylinder demonstrate comparable accuracy to the circular cylinder cases, with computed Strouhal numbers and drag coefficients showing good agreement with established literature values across available Reynolds numbers in literature (see Tab. SI 5).

Environment setup. The square cylinder environment follows the same fundamental framework as the circular cylinder configuration described above, with identical reward formulation ($r = -|C_D| - \omega|C_L|$), state space representation through configurable point probes, and episode structure spanning 200 control actions over approximately 10 vortex shedding periods.

The key distinction lies in the actuation strategy, where jet-based control is exclusively employed. Unlike

(a) 2D, $Re = 200$

Reference	St	$\overline{C_D}$	$C_{L'}$
Present study	**0.151**	**1.469**	**0.391**
Sohankar et al.[184]	0.170	1.46	0.32
Sohankar et al.[192]	0.15	1.462	0.377
Cheng et al.[193]	0.15	1.45	0.372
Okajima[194]	0.148	1.45	–
Jiang & Cheng[195]	0.152	1.443	0.412

(b) 2D, $Re = 1,000$

Reference	St	$\overline{C_D}$	$std(C_L)$
Present study	**0.121**	**2.302**	**1.405**
Yan et al.[77]	0.120	2.34	1.49
Okajima[194]	0.124	–	–
Norberg[196]	0.124	2.02–2.33	–
Cao & Tamura[197]	0.123	2.07	–
Bai & Alam[185]	0.120	2.10–2.33	–

(c) 3D, $Re = 300$

Reference	St	$\overline{C_D}$	$C_{L'}$
Present study	**0.146**	**1.441**	**0.222**
Sohankar et al.[184]	0.153	1.47	0.2
Yoon et al.[198]	0.145	1.431	0.205
Jiang & Cheng[195]	0.146	1.434	0.183

Table SI 5: Comparison of 2D and 3D square cylinder flow results at different Reynolds numbers. St: Strouhal number; $\overline{C_D}$: Time-averaged drag coefficient; $C_{L'}$: RMS lift coefficient; $std(C_L)$: Standard deviation of lift coefficient; –: Data not reported or not applicable

the circular cylinder's zero-net mass-flux configuration, the square cylinder utilizes individual jets that can be positioned at four discrete locations: leading edge upper, leading edge lower, trailing edge upper, and trailing edge lower surfaces. The RL agent controls the mass flux of each active jet independently, with actions normalized to the range $[-1, 1]$ for consistent algorithm performance.

The temporal coupling between the CFD solver and RL agent employs Reynolds number-specific action frequencies: 225, 750, and 375 CFD timesteps per control action for 2D cases at $Re = 200,\ 1,000,\ 3,900$ respectively, and 700, 900, and 875 timesteps for corresponding 3D cases. This environment configuration enables the investigation of asymmetric control strategies and the comparative effectiveness of leading versus trailing edge actuation for square cylinder wake management, while maintaining the same comprehensive sensing and reward framework established for the circular cylinder testbed.

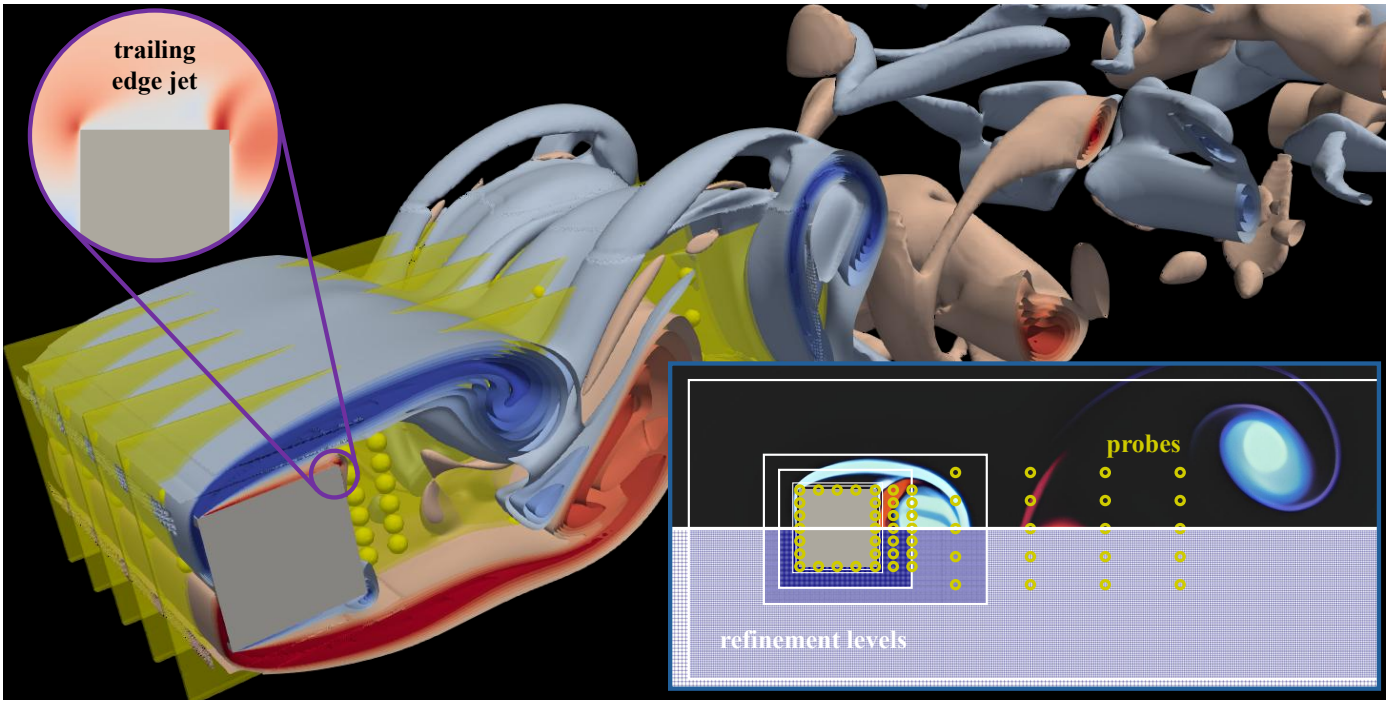

Figure SI 6: Computational domain setup, sensor probe distribution and actuation strategy: Three-dimensional view showing the probe distribution around the square cylinder with vortical structures visualized through Q-criterion isosurfaces. The yellow dots in zoom-in highlight sensor probe locations in a single spanwise plane. Active flow control is performed through jet actuators positioned at the leading and/or trailing edge.

5.5 Flow around a NACA 0012 airfoil

Characteristic physics. The flow around a NACA 0012 airfoil in the Reynolds number range of 100 to 50,000 presents a rich variety of fluid dynamics phenomena, transitioning from steady, laminar flow to complex unsteady, transitional, and separated regimes. At the lower end of this spectrum, for Reynolds numbers on the order of 10^2, the flow is characterized by thick laminar boundary layers that are susceptible to separation, even at high angles of attack [199]. As the angle of attack is increased, the wake is often dominated by unsteady vortex shedding.

With an increase in the Reynolds number into the range of 10^3, the flow dynamics are frequently governed by the formation of a laminar separation bubble (LSB) on the suction side of the airfoil [200, 201]. This phenomenon occurs when the laminar boundary layer separates due to an adverse pressure gradient, transitions to a turbulent state within the separated shear layer, and then reattaches to the airfoil surface. The formation, size, and behavior of the LSB are highly sensitive to both the Reynolds number and the angle of attack, which can lead to significant nonlinearities in the aerodynamic characteristics of the airfoil [200]. Near-stall conditions can induce self-sustained, low-frequency oscillations in the flow field, which are linked to the quasi-periodic bursting and reforming of the laminar separation bubble [201]. The various flow regimes can be categorized based on these dynamics, from steady attached flow at very low angles of attack, to the formation of a stable LSB, and ultimately to large-scale separation and stall, which is characterized by the shedding of large vortices [202].

A primary challenge in the computational modeling of these flow regimes is the accurate prediction of the laminar-to-turbulent transition. This transition is a critical element as it determines whether the separated flow will reattach. Standard RANS models often struggle to accurately capture the complex physics within the separation bubble. Consequently, higher-fidelity methods such as LES or DNS are necessary to resolve the fine-scale turbulent structures and transition mechanisms, albeit at a much greater computational expense. The intricate interplay between the Kelvin-Helmholtz instability of the separated shear layer, the amplification of disturbances, and the eventual turbulent breakdown and reattachment complicates the fundamental understanding of the physics.

Significant differences are observed between 2D and 3D configurations. While 2D simulations can capture many of the fundamental aspects of LSB formation and vortex shedding, they do not account for spanwise instabilities. In a 3D flow, the separated shear layer is subject to three-dimensional instabilities that can lead to a more rapid and complex transition to turbulence [203]. These three-dimensional effects can alter the size and shape of the separation bubble and, as a result, the overall aerodynamic forces [204]. This generally leads to a decrease in aerodynamic performance when compared to idealized two-dimensional predictions.

The NACA 0012 airfoil within the considered Reynolds number range is a crucial benchmark case for the development and testing of flow control applications, including those that utilize RL. The simple, symmetric geometry of the airfoil produces fundamentally important and challenging flow phenomena, which are directly relevant to the performance of micro air vehicles (MAVs), drones, and small wind turbine blades. The high sensitivity of the flow to small perturbations makes it an excellent platform for evaluating active flow control strategies aimed at suppressing separation, reducing drag, and enhancing lift. To this end, RL is a particularly promising approach as it can discover complex, non-intuitive, time-dependent control strategies, such as using blowing and suction jets, without requiring a precise analytical model of the flow physics. Nonetheless, the inherent instabilities of the shear layer and the broadband nature of turbulence necessitate control systems with high bandwidth and precise actuation. The effectiveness of a control strategy can be highly dependent on the specific flow state, which poses a challenge for the development of robust controllers that can operate effectively across a range of angles of attack and Reynolds numbers.

Characteristic physics in gust-airfoil interactions. Understanding the aerodynamic consequences of an airfoil encountering an atmospheric gust is a pivotal challenge in aeronautics, with direct implications for aircraft structural integrity, safety, and flight stability. The issue is especially pronounced for smaller aerial platforms,

such as drones and MAVs, whose lower operating speeds make them highly susceptible to disturbances. When the flight speed of such a vehicle is on the same order as the gust velocity, a condition of near-resonance can occur, which dramatically magnifies the gust's aerodynamic impact [205]. The increasing deployment of autonomous aircraft in unpredictable environments, such as urban settings or mountainous terrain, has intensified the need for robust technologies capable of mitigating these adverse gust-induced effects.

The nature of this aerodynamic interaction can be broadly classified based on the gust ratio, G, which compares the gust's velocity to that of the aircraft's freestream. For large commercial aircraft, their high cruise speeds ensure the gust ratio is typically low ($G < 1$). In these scenarios, provided the gust amplitude is not excessive, the aerodynamic response can often be approximated using linear theoretical models [206]. However, the validity of these linear models degrades as nonlinearities become more prominent. In sharp contrast, smaller vehicles frequently operate in conditions where the gust velocity matches or exceeds their flight speed ($G \geq 1$). This high-G regime, often termed 'extreme aerodynamics', introduces a set of physical phenomena far more complex than those seen in milder encounters, rendering linear theories inadequate [207].

Physically, a high-G interaction is dominated by highly unsteady and often violent aerodynamic events. As the gust alters the oncoming flow, the airfoil experiences a rapid and substantial change in its effective angle of attack. This can trigger the formation of a large, coherent leading-edge vortex. Concurrently, the rapid adjustment in the airfoil's overall circulation leads to the shedding of vorticity from the trailing edge, forming a trailing-edge vortex. If the effective angle of attack surpasses a critical threshold, the flow can undergo dynamic stall, a process distinct from its steady-state counterpart. During dynamic stall, large-scale vortical structures detach from the airfoil's surface and convect downstream, causing dramatic and often unpredictable shifts in lift and moment characteristics [208]. The resulting aerodynamic loads can momentarily spike to levels $200 - 300\%$ greater than the maximum steady-state loads. This behavior is also accompanied by significant hysteresis in the force and moment curves, meaning the aerodynamic response depends on the history of the motion, which presents a major complication for control system design.

To summarize, the development of effective flow control strategies for gust load alleviation is the ultimate engineering goal. Conventional control systems, which rely on the deflection of large control surfaces, often have actuation delays and bandwidth limitations that make them too slow to counteract the rapid onset of high-frequency gusts. This has spurred innovation in active flow control technologies. The inherent complexity and unpredictability of gust encounters make them an ideal application area for reinforcement learning as the agent learns an optimal control strategy through direct trial-and-error interaction with its environment, making it well-suited to mastering the nonlinear dynamics of gust-airfoil interactions. However, the transient nature of the gust event demands a control policy that can respond almost instantaneously. To systematically develop and validate these advanced data-driven models and control algorithms, the aerospace community urgently needs well-documented benchmark test cases, such as flow over the NACA 0012 airfoil.

Numerical setup and validation. The NACA 0012 airfoil simulations are conducted in both 2D and 3D configurations to capture the full spectrum of flow physics relevant to gust-airfoil interactions. For the 2D cases, the computational domain is defined by $(x/c, y/c) \in [0, 40] \times [-10, 10]$ with the NACA 0012 airfoil centered at $(x/c, y/c) = (10, 0)$. This 2D configuration allows for efficient exploration of parameter spaces and validation against classical airfoil theory, while serving as a baseline for understanding the fundamental flow mechanisms before extending to 3D effects. The reduced computational cost of 2D simulations enables systematic studies across wider ranges of angles of attack and Reynolds numbers.

For the 3D cases, the computational domain spans $[32 \times 16 \times 4]$ chord lengths $c = 1.0$ for $Re \leq 1,000$ and $[32 \times 16 \times 0.5]$ chord lengths for $Re \in [10,000,\ 50,000]$, with the NACA 0012 airfoil positioned 8c from the inflow boundary. The domain extent is designed to minimize boundary reflections while maintaining computational efficiency. The airfoil surface is treated as a no-slip boundary condition implemented through an interpolated bounce-back scheme. Periodic boundary conditions are imposed in the spanwise direction to

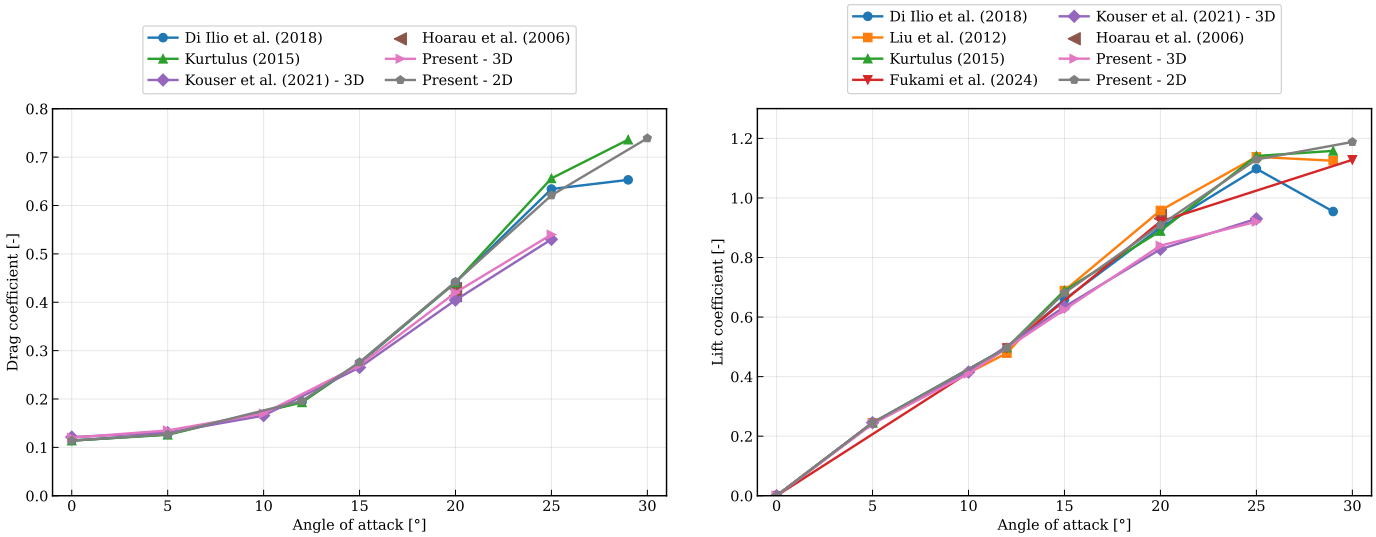

(a) drag coefficient

(b) lift coefficient

Figure SI 7: Comparison of (a) drag coefficient and (b) lift coefficient as a function of the angle of attack for a NACA 0012 airfoil at $Re = 1,000$. Results from the present study (2D and 3D simulations) are compared with experimental and numerical data from the literature.

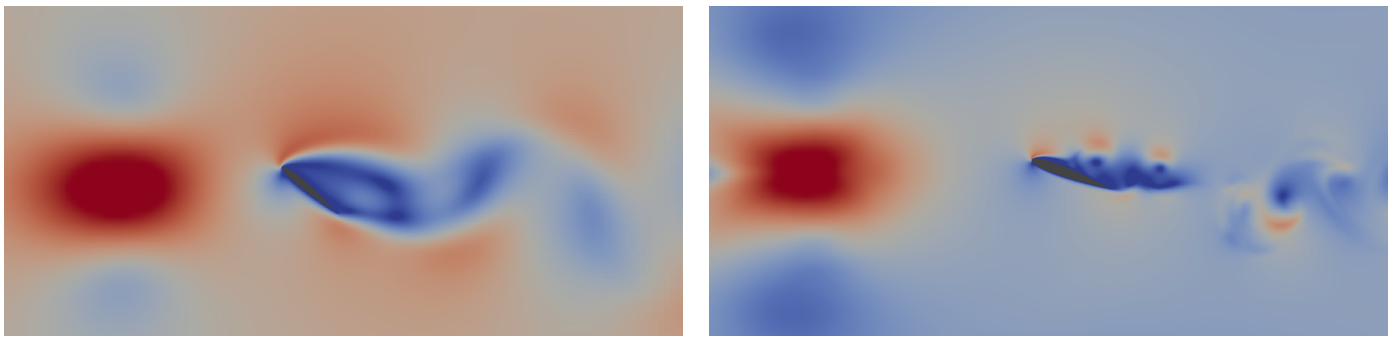

(a) 2D environment: $Re = 100$ & $\alpha = 40°$

(b) 3D environment: $Re = 1,000$ & $\alpha = 20°$

Figure SI 8: Exemplary visualization of the transversal gust scenario for 2D (a) and 3D (b) environments

simulate a nominally two-dimensional configuration while capturing three-dimensional flow instabilities.

The grid resolution is chosen to ensure that the smallest turbulent scales are adequately captured, particularly in the separated flow regions. The computational mesh employs an adaptive refinement approach with 14 refinement levels, with the grid spacing determined by $\Delta_n = \Delta_0/2^n$ where $\Delta_0^{(3D)} = 32c$. For 2D cases, the base grid spacing is $\Delta_0^{(2D)} = 40c$ with refinement levels up to $n = 12$, providing approximately 200 grid points per chord length in the highest resolution regions around the airfoil. Similar to [209], multiple refinement patches are strategically positioned to capture the boundary layer, wake region, and areas of expected flow separation with sufficient resolution. The numerical setup is validated against benchmark data from the literature [207, 210–214] showing good agreement in time-averaged lift and drag coefficients across various angles of attack $0° < \alpha < 30°$ for both 2D and 3D configurations (see Fig. SI 7).

Environment implementation. The transverse gust is implemented through a prescribed velocity perturbation imposed at the inflow boundary. The gust profile follows a 1-cosine approach with a gust factor $G =$

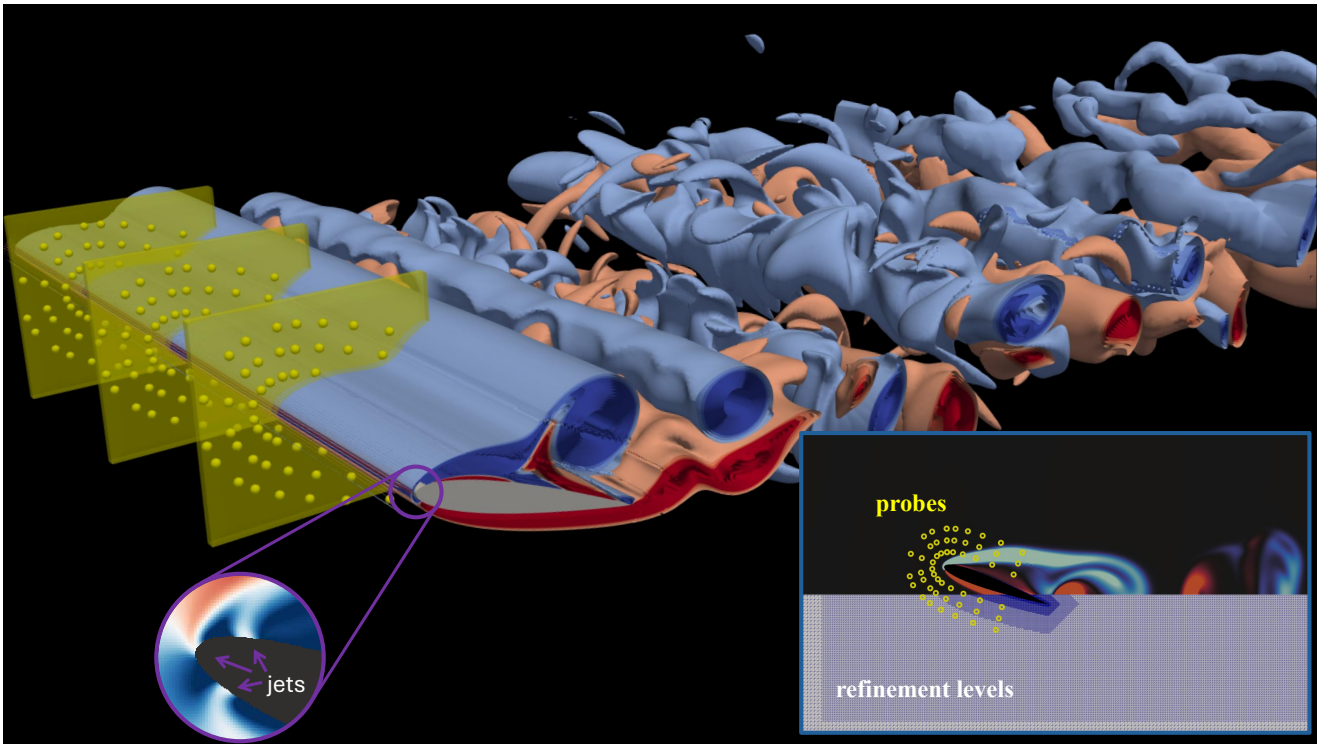

Figure SI 9: Computational domain setup, sensor probe distribution and actuation strategy for the gust-airfoil interaction environments: Three-dimensional view showing the probe distribution around the airfoil with vortical structures visualized through Q-criterion isosurfaces. The yellow dots in lower right zoom-in highlight sensor probe locations in a single spanwise plane. Active flow control is performed using three independent jet actuators positioned along the leading edge of the NACA 0012 airfoil, each covering 3% of the chord length and extending across the full span (see lower left zoom-in).

2.0, representing the ratio of peak gust velocity to freestream velocity (see Fig. SI 8). The gust temporal development is controlled to achieve the desired interaction dynamics with the airfoil. The state space representation consists of user-configurable point probes distributed throughout the computational domain, providing measurements of velocity components, pressure, density, and body forces at specified locations. To facilitate interactions between the RL agent and the flow environment, three jet actuators are distributed across the leading edge of the airfoil (see Fig. SI 9). Each actuator can be controlled independently, covers 3% of the chord length, and extends over the entire spanwise location. The action spaces are continuous and normalized in the range $[-1.0, 1.0]$.

Depending on the investigated Reynolds number, the number of CFD timesteps varies in the range of $225 - 1,000$, delivering the necessary temporal granularity to represent critical flow physics while preserving computational tractability. The reward function is formulated to minimize gust-induced force fluctuations while maintaining aerodynamic efficiency:

$$R(t) = -|C_L(t) - \overline{C_{L,ref}}| - \omega\,|C_D(t) - \overline{C_{D,ref}}| \tag{25}$$

where $C_L(t)$ and $C_D(t)$ are the instantaneous drag and lift coefficients while $\overline{C_{L,ref}}$ and $\overline{C_{D,ref}}$ represent time-averaged coefficients of the unperturbed reference case. The weighting coefficient $\omega = 0.25$ is tuned to balance the competing objectives of gust mitigation and drag reduction.

5.6 Flow around a cube

Characteristic physics. The flow around a suspended cube represents a canonical problem in fluid dynamics, offering a fundamental case study for three-dimensional bluff body wakes with fixed separation points. Unlike a sphere, where the separation location is Reynolds number dependent, the sharp leading edges of a cube dictate the points of flow separation, leading to a unique and complex evolution of the wake structure as the Reynolds number increases. For Reynolds numbers in the range of 300 to 3,700, the flow transitions through a sequence of distinct regimes, each characterized by specific vortical dynamics and stability properties.

Within the lower end of this Reynolds number range, several key bifurcations govern the wake's topology. The flow is initially steady and symmetric up to a critical Reynolds number of approximately 215 [215]. As the Reynolds number increases beyond this point, the flow undergoes a first bifurcation, losing its orthogonal symmetry to become steady but asymmetric, a state that persists up to a Reynolds number of about 265. This is followed by a second Hopf bifurcation around a Reynolds number of 270, where the flow becomes unsteady and periodic, characterized by the shedding of hairpin-like vortices [215, 216]. These hairpin vortices are initially shed in a regular, periodic manner. Experimental investigations using techniques such as Particle Image Velocimetry (PIV) and laser-induced fluorescence have confirmed this sequence of bifurcations, aligning well with numerical simulations [216]. As the Reynolds number further increases towards 400, the hairpin vortex shedding becomes more complex, eventually transitioning to a chaotic vortex shedding regime around a Reynolds number of 310, where the coherence of the shed structures begins to break down [217].

Modeling the flow around a cube presents significant challenges, particularly as the Reynolds number increases into the turbulent regime. Accurately capturing the precise Reynolds numbers for the initial bifurcations requires high-fidelity numerical methods with sufficient spatial resolution to resolve the thin shear layers separating from the leading edges [215]. The interaction between these shear layers from the top, bottom, and side faces of the cube creates a highly three-dimensional and inherently unstable wake. As the Reynolds number climbs towards 3,700, the wake becomes fully turbulent, characterized by a broad range of spatial and temporal scales. The breakdown of larger coherent structures into smaller-scale turbulence and the complex interactions between different vortical structures are computationally expensive to resolve. Furthermore, ensuring the numerical schemes accurately capture the sharp-corner-induced separation without introducing excessive numerical diffusion is a persistent challenge. Understanding the physics is complicated by the fully three-dimensional nature of the vortex dislocations and the transition to turbulence in the separated shear layers.

Therefore, the flow around a cube serves as an important test case for the development and benchmarking of flow control strategies, including those based on reinforcement learning. The well-defined sequence of flow regimes offers a varied landscape to test the robustness and adaptability of control algorithms. The objective of such control could be drag reduction, lift suppression, or wake stabilization. The sharp edges provide fixed locations for the placement of actuators, such as synthetic jets or plasma actuators, simplifying one aspect of the control problem. However, the inherent three-dimensionality of the wake presents a significant challenge for flow control. Actuation strategies must be able to influence a complex, three-dimensional flow field, which necessitates a high-dimensional action space for an RL agent. For instance, controlling the interaction and instability of the multiple shear layers simultaneously is a non-trivial task. A key challenge for RL is the development of a low-dimensional state representation from achievable sensor measurements (e.g., surface pressure sensors) that can adequately describe the high-dimensional state of the flow. The agent must learn a control policy that can effectively manipulate the different instabilities present in the various flow regimes, from the steady asymmetry to the chaotic vortex shedding. The time delay between an actuation and its effect on the global flow properties, such as drag, also poses a significant hurdle for the learning process, requiring the RL algorithm to handle delayed rewards and long-term consequences of its actions. The complexity of the cube wake with its multiple interacting shear layers and instabilities therefore provides a challenging and realistic benchmark for advancing the capabilities of reinforcement learning in active flow control.

(a) $Re = 300$

Reference	St	$\overline{C_D}$
Present study	**0.102**	**0.855**
Saha et al.[215]	0.095	0.804
Saha[218]	0.097	0.833
Haider & Levenspiel [219]	–	0.985
Holzer & Sommerfeld[220]	–	0.923
Khan et al. [221]	–	0.843

(b) $Re = 1,000$

Reference	$\overline{C_D}$
Present study	**0.984**
Holzer & Sommerfeld[220]	0.815
Khan et al.[222]	0.883
Khan et al. [221]	0.968
Haider & Levenspiel [219]	1.121

Table SI 6: Comparison of 3D cube flow results at different Reynolds numbers. St: Strouhal number; $\overline{C_D}$: Time-averaged drag coefficient; –: Data not reported or not applicable

Numerical setup and validation. The cube benchmark follows the same computational setup as the square cylinder case, with the key difference being the three-dimensional bluff body geometry. The cube has a side length D and the Reynolds numbers are $Re \in [300,\ 1,000,\ 3,700]$. The 3D domain is $(x/D, y/D, z/D) \in [0, 32] \times [0, 16] \times [0, 16]$ with the cube centered at $(x/D, y/D, z/D) = (8, 8, 8)$ and non-periodic boundary conditions in all directions. All other boundary conditions, grid refinement levels, and resolution criteria follow the square cylinder specifications. Validation results shown in Tab. SI 6 demonstrate comparable accuracy to the square cylinder cases, with good agreement to established literature values where available.

Environment implementation. The cube environment follows the same fundamental framework as the square cylinder configuration, with identical reward formulation, state space representation, and episode structure.

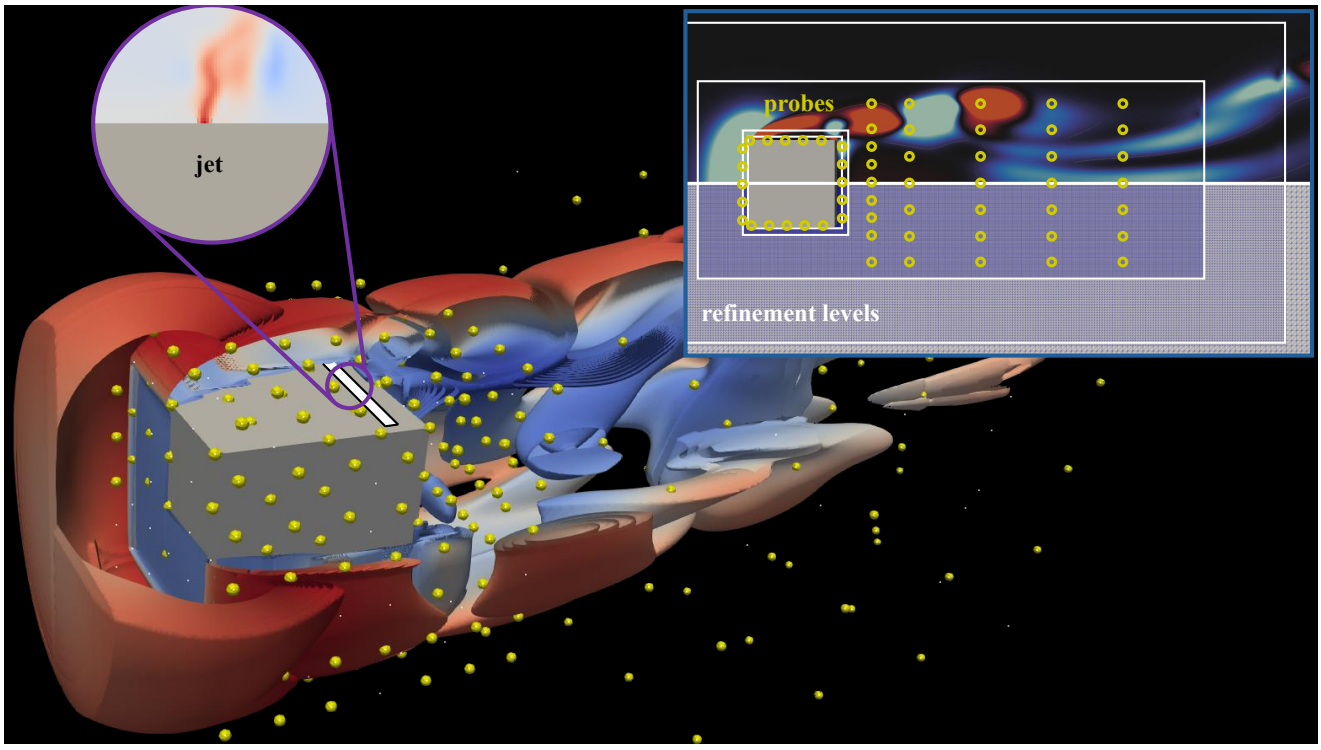

Figure SI 10: Computational domain setup, sensor probe distribution and actuation strategy for the flow around a cube: Three-dimensional view showing the probe distribution around the cube with vortical structures visualized through Q-criterion isosurfaces. The yellow dots highlight sensor probe locations in a single spanwise plane. Active flow control is performed using independent jet actuators positioned along the leading and trailing edge of the cube.

The key distinction is the three-dimensional jet actuation strategy, where jets can be positioned across multiple cube faces: leading/trailing edges with upper, lower, and side face locations (see Fig. SI 10). The RL agent controls each jet's mass flux independently, with actions normalized to $[-1, 1]$. Temporal coupling follows the square cylinder approach with Reynolds number-specific action frequencies in the range of 1,000 to 1,250 CFD timesteps per control action. This configuration enables the investigation of multi-face actuation strategies for three-dimensional wake control.

5.7 Flow around a sphere

Characteristic physics. Flow past spheres within the Reynolds number regime 300-3,700 demonstrates intricate transitional phenomena marked by sequential symmetry-breaking bifurcations and progressive wake complexity that establishes this configuration as fundamental for understanding three-dimensional bluff body aerodynamics and developing advanced control methodologies. This intermediate Reynolds number range captures the essential transition from organized periodic vortex structures to chaotic subcritical turbulent behavior, presenting distinctive opportunities and obstacles for both theoretical analysis and practical intervention strategies.

The underlying flow mechanics throughout this range are dictated by a systematic bifurcation sequence that progressively destroys flow symmetries and introduces increasingly complex temporal dynamics. The initial critical transition manifests around $Re = 212$ through a supercritical pitchfork bifurcation that eliminates axisymmetry while preserving planar symmetry, establishing steady non-axisymmetric flow patterns [223]. Subsequently, at approximately $Re = 280$, a supercritical Hopf bifurcation introduces periodic temporal behavior characterized by regular hairpin vortex shedding with Strouhal numbers near 0.18-0.20 [224]. The final primary transition occurs through a Neimark-Sacker bifurcation around $Re = 330$, generating quasiperiodic dynamics with two incommensurate frequencies that create complex modulation patterns while maintaining overall wake organization [225].

These successive instability mechanisms establish fundamental distinctions between lower Reynolds number steady flows and the complex transitional behavior observed in the $Re = 300 - 3,700$ range. While computational approaches utilizing steady-state assumptions remain viable below $Re = 212$, the emergence of temporal instabilities necessitates fully unsteady three-dimensional simulation methodologies that capture both large-scale wake evolution and fine-scale vortical structures [224, 226]. The hairpin vortex morphology characteristic of this regime creates a distinctive flow topology involving interconnected vortex loops and induced secondary structures that significantly influence drag, heat transfer, and mixing properties. Beyond $Re = 800$, the wake transitions toward subcritical turbulent characteristics while retaining coherent large-scale organization, establishing a complex multiscale environment where deterministic and stochastic elements coexist [227].

Consequently, this rich transitional behavior positions spherical wake flows as exceptionally valuable canonical benchmark for advancing flow control science and validating emerging computational strategies. The geometric simplicity eliminates confounding effects associated with complex shapes while preserving all essential three-dimensional bluff body physics, creating optimal conditions for isolating and understanding control mechanisms. The Reynolds number window of $Re \in [300 - 3,700]$ provides particularly favorable conditions for these developments because the flow complexity challenges algorithm sophistication while maintaining computational feasibility for extensive training iterations.

In summary, the well-established theoretical foundation surrounding spherical wake physics renders this configuration invaluable as advancing computational methodologies and experimental capabilities continue expanding flow control horizons for purely three-dimensional bluff body aerodynamics. The thorough documentation of fundamental mechanisms enables confident evaluation of whether innovative approaches genuinely capture essential physics or merely exploit numerical artifacts. Consequently, the extensively characterized sphere wake provides an indispensable validation platform for novel developments prior to extension toward more complex geometries and flow physics.

(a) $Re = 300$

Reference	St	$\overline{C_D}$
Present study	**0.142**	**0.636**
Johnson & Patel[223]	0.137	0.656
Roos & Willmarth[228]	–	0.629
Almedeij[229]	–	0.602
Clift et al.[230]	–	0.674

(b) $Re = 3,700$

Reference	St	$\overline{C_D}$
Present study	**0.212**	**0.391**
Almedeij[229]	–	0.409
Clift et al.[230]	–	0.378
Haider & Levenspiel[219]	–	0.392
Turton & Levenspiel[231]	–	0.386
Rodriguez et al.[226]	0.215	0.394
Yun et al.[232]	0.21	0.355

Table SI 7: Comparison of 3D sphere flow results at different Reynolds numbers. St: Strouhal number; $\overline{C_D}$: Time-averaged drag coefficient; –: Data not reported or not applicable

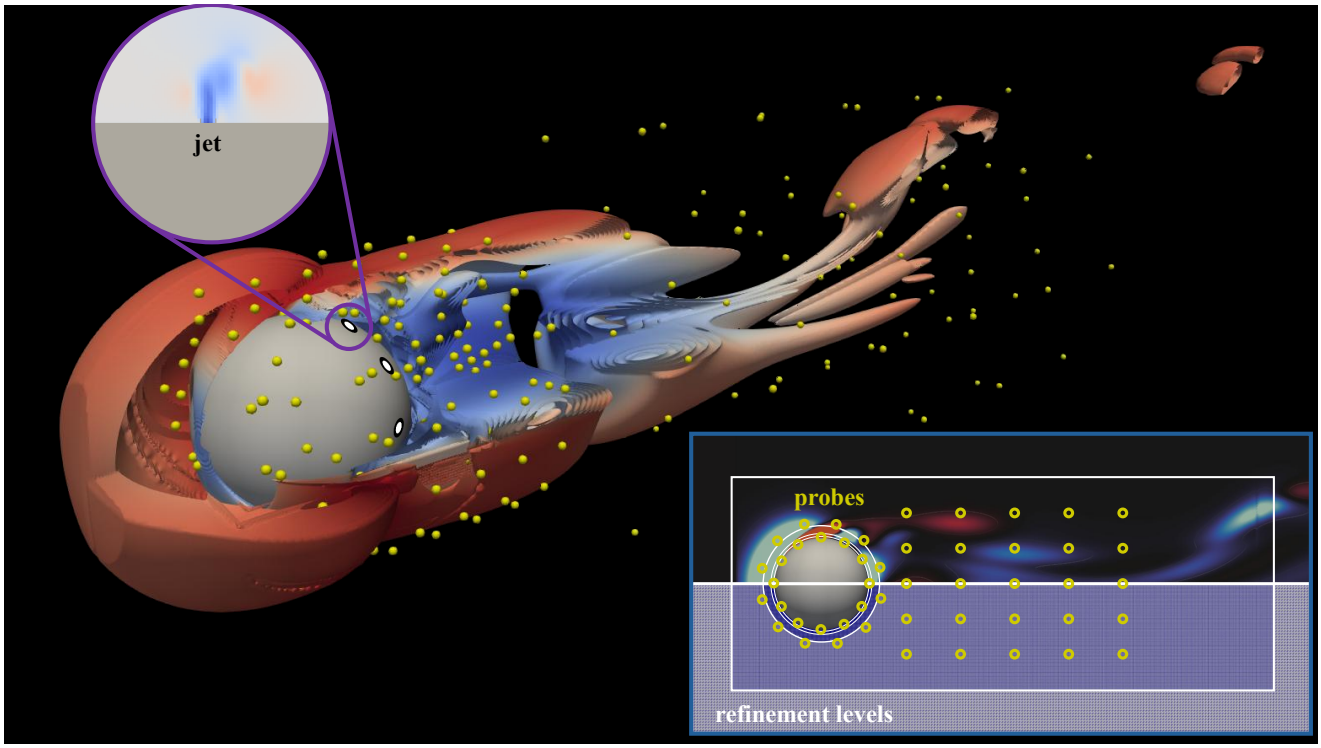

Figure SI 11: Computational domain setup, sensor probe distribution and actuation strategy for the flow around a sphere: Three-dimensional view showing the probe distribution around the sphere with vortical structures visualized through Q-criterion isosurfaces. The zoom-in highlights sensor probe locations in a single spanwise plane. Independent jet actuators positioned in the sphere's rear half enable active flow control.

Numerical setup and validation. The sphere setup follows the cylinder benchmark scenario with 3D low Mach number flows ($Ma < 0.2$) at Reynolds numbers $Re \in [300,\ 3,700]$ based on the sphere diameter D. The computational domain differs from the cylinder configuration with $(x/D, y/D, z/D) \in [0, 32] \times [0, 16] \times [0, 16]$, featuring an extended z-direction domain. The sphere is centered at $(x/D, y/D, z/D) = (8, 8, 8)$. Grid spacing and refinement follow the cylinder setup with $\Delta_0^{(3Dsphere)} = 32D$ and refinement levels up to $n = 14$, leading up to 512 cells per sphere diameter D. Inlet and outlet boundary conditions are identical to the cylinder configuration. However, outlet boundary conditions replace the periodic conditions on all lateral boundaries due to the extended z-domain. Validation results demonstrate similarly good accuracy compared to the cylinder setup, with Strouhal numbers and drag coefficients matching within established literature ranges for sphere flows (see Tab. SI 7), where benchmark results are available.

Environment implementation. The sphere flow environment uses the same default reward objective as the cylinder setup, targeting drag minimization and lift force oscillation reduction. The actuation strategy differs from the cylinder configuration through eight cylindrical jets positioned on a circle at the sphere's backside, located at 60° around the streamwise x-axis. Unlike the cylinder's slot-like jets, these jets have a circular shape in the z-direction (see Fig. SI 11) and allow independent mass flux control by the RL agent.

The environment supports the Reynolds numbers $Re = 300,\ 3,700$, with an identical state space representation through user-configurable point probes as the cylinder counterpart. Similarly, training episodes and temporal coupling parameters follow the cylinder configuration, featuring 300 and 750 CFD timesteps per control action, respectively.

5.8 Flow through a stenotic pipe

Characteristic physics. Flow through a stenotic pipe has been extensively studied as a canonical configuration to investigate complex hemodynamic and biofluidic phenomena. The presence of a localized narrowing introduces strong acceleration of the fluid jet, followed by an adverse pressure gradient downstream that promotes flow separation, shear layer instabilities, and, at sufficiently high Reynolds numbers, transition to turbulence [233]. These dynamics create characteristic features such as recirculation zones, vortex shedding, and highly fluctuating wall shear stresses, which are of particular relevance in cardiovascular applications, for instance, in the progression of atherosclerosis and thrombosis. The flow field is highly sensitive to the severity and geometry of the stenosis as well as the Reynolds number. As such, stenotic pipe flow serves as a benchmark problem for studying transitional shear flows as well as fluid–structure interaction in arterial geometries.

Beyond its relevance to vascular hemodynamics, the stenotic pipe is also a valuable generic case for studying respiratory flows under obstructed conditions. The localized constriction mimics the airflow limitations encountered in the human nasal cavity during pathological states such as septal deviation or turbinate hypertrophy. In this context, a level-set approach has been developed for monitoring the change in pressure and temperature distributions when iteratively modifying the surface from a stenosed to an unconstricted pipe [234]. After successfully testing this on the stenotic pipe, the authors have extended this framework to capture surface modifications from pre- to post-surgical nasal geometries. Building on this methodological foundation, subsequent studies integrated RL with CFD by letting an agent control interpolation factors that modify the geometry via the same level-set representation [83]. The agent's goal was to find a compromise between reducing pressure loss and improving the heating capability. In the context of nasal obstruction surgery, this approach has been extended to nasal cavity geometries to design optimal surgical intervention strategies [103]. In this sense, the stenotic pipe serves as a bridge between canonical fluid mechanics problems and clinically relevant respiratory applications, making it a suitable benchmark for developing and validating RL–CFD platforms.

Beyond steady inflow conditions, stenotic pipe flow has also been investigated under pulsatile forcing, which more closely resembles the physiological environment in cardiovascular and respiratory systems. The periodic acceleration and deceleration of the fluid introduce additional instabilities that interact with the stenosis-induced shear layers, often amplifying vortex shedding and enhancing the complexity of the downstream flow structures [235]. These effects can result in intermittent turbulence, increased wall shear stress fluctuations, and significant cycle-to-cycle variability in recirculation zones.

In addition to pulsatile inflow, oscillatory flow through stenotic geometries has been examined as a canonical setup for studying shear reversal and resonance phenomena under zero-mean periodic forcing. Unlike pulsatile flow, which superimposes forward and reverse phases on a mean flow, purely oscillatory forcing accentuates the interaction between unsteady shear layers and flow separation in both directions, leading to enhanced mixing and strongly asymmetric vortex dynamics. Under such conditions it has been demonstrated how the frequency of oscillation relative to the stenosis geometry governs vortex strength and flow reversal patterns [236].

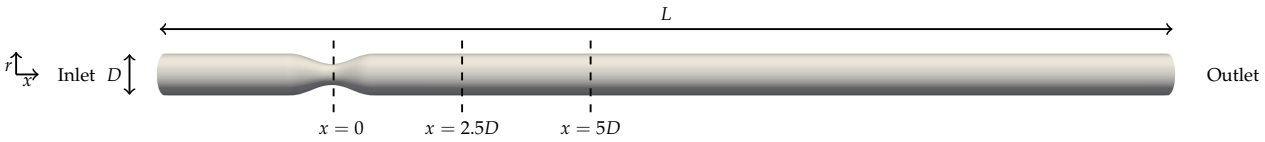

Figure SI 12: Computational domain for validating the stenotic pipe flow.

Building on this canonical framework, the present study explores a novel RL–CFD coupling in which an RL agent interacts with oscillatory stenotic pipe flow by controlling the inlet temperature. The agent's objective is to maintain the temperature field downstream of the stenosis as close as possible to a prescribed target value. This setup not only leverages the complex unsteady dynamics of oscillatory stenotic flows as a challenging benchmark for flow control, but also provides a direct link to biomedical applications. Specifically, the stenotic pipe serves as a generic surrogate for obstructed respiratory passages, where maintaining controlled temperature and flow conditions is critical. In this context, the methodology holds promise for extension to clinically relevant scenarios such as the pre-calibration of mechanical ventilation machines, where RL-driven control strategies could help adapt inlet conditions to patient-specific airway geometries and pathologies.

Implementation validation. The computational domain used for validating the stenotic pipe flow and its coordinate system are illustrated in Fig. SI 12. Details about the curvature of the stenosis can be found in [233]. The Reynolds number based on the pipe diameter at the inlet D is set to $Re = U_{ref} \cdot D)/\nu = 500$ to match the conditions in [233], where $D = 1m$, $\nu = 1.63 \cdot 10^5\ m^2/s$ is the kinematic viscosity of air, and U_{ref} the spatially averaged velocity at the inlet. The domain length is $L = 38D$.

At the inlet, the velocity profile of a fully developed laminar pipe flow is prescribed and the density of the fluid is linearly extrapolated from the neighboring inner cells. At the outlet, a constant pressure p_{out} is set, and the velocity is extrapolated from the inner cells. To satisfy the no-slip condition at the pipe walls, an interpolated bounce-back scheme is used [126]. These boundary conditions match the boundary conditions of the reference simulation in [233].

Figure SI 13a shows results of a mesh refinement study. Profiles of the normalized streamwise velocity component u/U_{ref} at $x = 5D$ with various mesh resolutions are compared to the reference solution from [233] (black). The coarse mesh (blue) has a resolution of $\Delta x = D/50$ and $2.5 \cdot 10^6$ cells. Results with the coarse

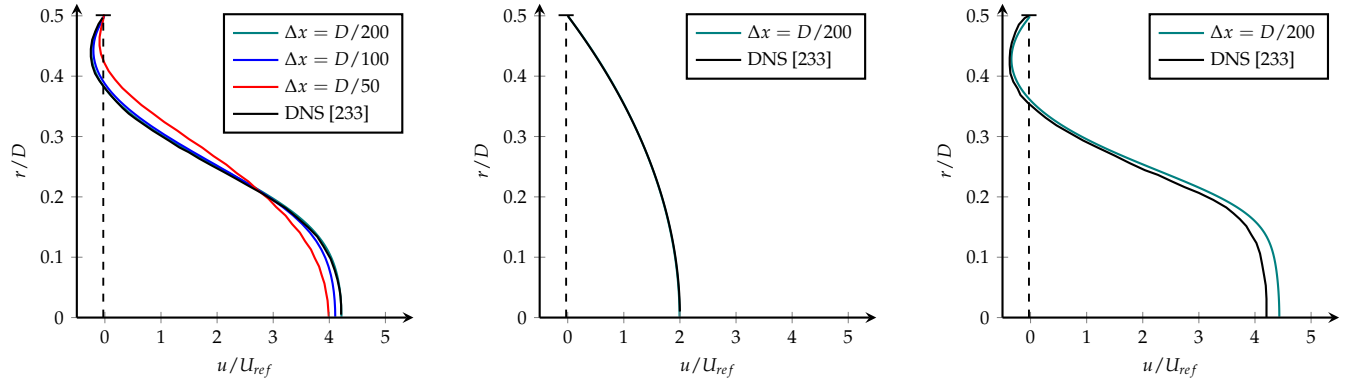

(a) Mesh refinement study at $x = 5D$.

(b) Inlet profiles with $\Delta x = D/200$.

(c) Profiles at $x = 2.5D$ with $\Delta x = D/200$.

Figure SI 13: Profiles of u/U_{ref} for different mesh resolutions (a) or at different locations with the highest resolution (b, c) compared to the reference case from the DNS in [233].

mesh indicate a smaller recirculation zone between $r/D = 0.4$ and $r/D = 0.5$ and an underprediction of the maximum velocity at $r/D = 0$ by 5.2%. The solution of the medium mesh (red) with a resolution of $\Delta x = D/100$ and $20 \cdot 10^6$ cells agrees better with the reference solution near the recirculation zone, but still shows a slight underprediction of the maximum velocity by 2.5%. Finally, the fine grid (green) has a resolution of $\Delta x = D/200$ and features $160 \cdot 10^6$ cells. The corresponding velocity profile matches well with the reference solution and has only a deviation in the maximum velocity of 1.4%.

Figure SI 13b shows that the inlet profile of the simulation with the LB method matches the inlet profile in [233]. The velocity profiles at $x = 2.5D$ in Fig. SI 13c reveal that the LB simulation agrees well with the reference solution in the near-wall region and recirculation zone. Deviations below 5% are observed near $r/D = 0$.

The comparisons of velocity profiles and recirculation dynamics across different grid resolutions demonstrate that the fine mesh solution agrees closely with the established DNS benchmark [233]. Together with the previously verified thermal model [124], these results confirm that the present LB solver reliably reproduces the key flow features of the stenotic pipe.

Environment implementation. The stenotic pipe control environment is likewise formulated as a discrete-time Markov Decision Process. The underlying flow is driven by an oscillatory inflow with a Womersley number of $\alpha = \frac{1}{2}D\sqrt{\frac{\omega}{\nu}} = 4$, where ω denotes the angular frequency. To introduce variability and mimic physiological fluctuations, a Gaussian noise term with mean 0, standard deviation 1, and amplitude 0.05 is superimposed on the sinusoidal signal. The agent interacts with the system by modulating the inlet temperature. Actions are continuous and normalized, with the initial condition corresponding to a normalized inlet-to-wall temperature ratio of $T_{\text{inlet}}/T_{\text{wall}} = 0.9$. At each time step, the agent can adjust the inlet temperature within the bound $|\Delta T_{\text{inlet}}/T_{\text{wall}}| \leq 0.05$.

The environment advances in intervals of 4,000 simulation time steps between two consecutive control decisions. This duration ensures that thermal perturbations introduced at the inlet have sufficient time to advect downstream and alter the velocity and temperature fields in the vicinity of the stenotic region. The state space is defined by 10 velocity, pressure, and temperature probes placed along the pipe centerline, distributed between $x = -3.5D$ upstream of the stenosis and $x = D$ downstream (see Fig. SI 14). These probes capture the temporal development of the flow response to the applied control, providing the agent with the necessary feedback for learning effective strategies. The reward function is formulated as $R(t) = -100 \cdot |(T_{target}(t)/T_{wall}) - 0.95|$, where T_{target} is the temperature on the centerline at $x = D$.

Figure SI 14 presents the normalized velocity and temperature fields of the uncontrolled 3D stenotic pipe flow for four characteristic states. In state I, the inflow velocity reaches its peak and cold fluid enters the pipe. In state II, the inflow velocity transitions from positive to negative, resulting in near-zero velocities throughout most of the domain. Under these conditions, wall-to-fluid heat transfer is enhanced, leading to a rise in fluid temperature. In state III, the reverse flow attains its maximum, driving warm fluid into the pipe from the outlet. Finally, state IV marks the transition from negative back to positive inflow velocity, again associated with low velocities and elevated heat transfer.

5.9 Kolmogorov flow

Characteristic physics. Chaotic dynamical systems often exhibit extreme events in which the system significantly deviates from its expected behavior. These extreme events exist in both nature and engineered systems, such as oceanic rogue waves, earthquakes, and shocks in power grids, often leading to adverse financial and humanitarian impacts [237]. As such, it is important to be able to predict and control these events. In turbulence, extreme events manifest as energy bursts, which are random and intermittent in both space and time [238]. To demonstrate this phenomena, a canonical two-dimensional turbulent flow driven by a sinusoidal forcing term is developed. This flow is known as the Kolmogorov flow, and in a certain

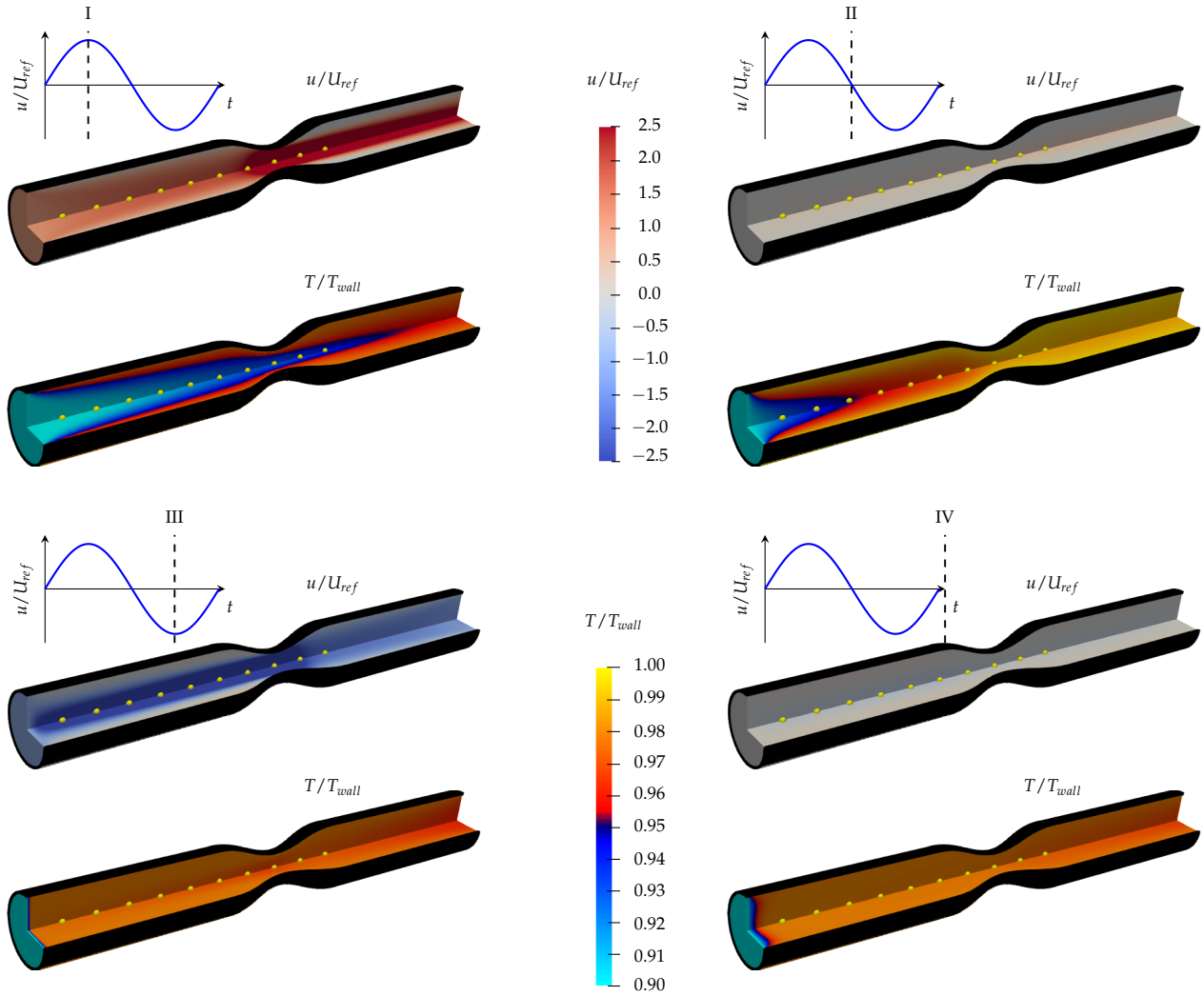

Figure SI 14: Normalized velocity and temperature fields of states I-IV of the uncontrolled 3D stenotic pipe flow.

parameter regime, it exhibits sporadic energy dissipation bursts due to a non-linear energy transfer between scales [42]. This often happens between Reynolds numbers 40 to 80 [239], as depicted in Figure SI 15 (b). For this implementation, it was found that the energy transfer that occurs is between a larger fluid structure with wavenumber (1,0), which transfers energy to smaller structures with wavenumber $(0,k_f)$ [42]. This rapidly increases the energy dissipation, as turbulent energy dissipates at smaller scales.

Numerical implementation. Earlier in this section, the vector form of the incompressible Navier-Stokes equation 14 was introduced. This can be reformulated in vorticity space by taking the curl of the momentum equation, which can then be solved with Fourier methods. To demonstrate this, recall that $\nabla \times \mathbf{u} = \omega$, $\nabla \cdot \mathbf{u} = 0$ for an incompressible fluid, and $\nabla \times \nabla \cdot q = 0$ where q is a scalar quantity. Equation 14 can then be simplified to:

$$\frac{\partial \mathbf{!}}{\partial t} + \mathbf{u} \cdot \nabla \omega = \nu \nabla^2 \omega + \mathbf{f}, \quad \omega = -\nabla^2 \Psi; \tag{26}$$

where the stream function Ψ, defined as $\mathbf{u} = \nabla \times \Psi$, ensures continuity. Equation 26 is also known as the vorticity equation [240], and is approximated numerically on a doubly-periodic domain of $[(0, 2\pi) \times (0, 2\pi)]$ with a sinusoidal forcing term of $\mathbf{f} = (\sin \mathrm{k}_f y, 0)$, where k_f is the forcing wavenumber. A pseudo-spectral

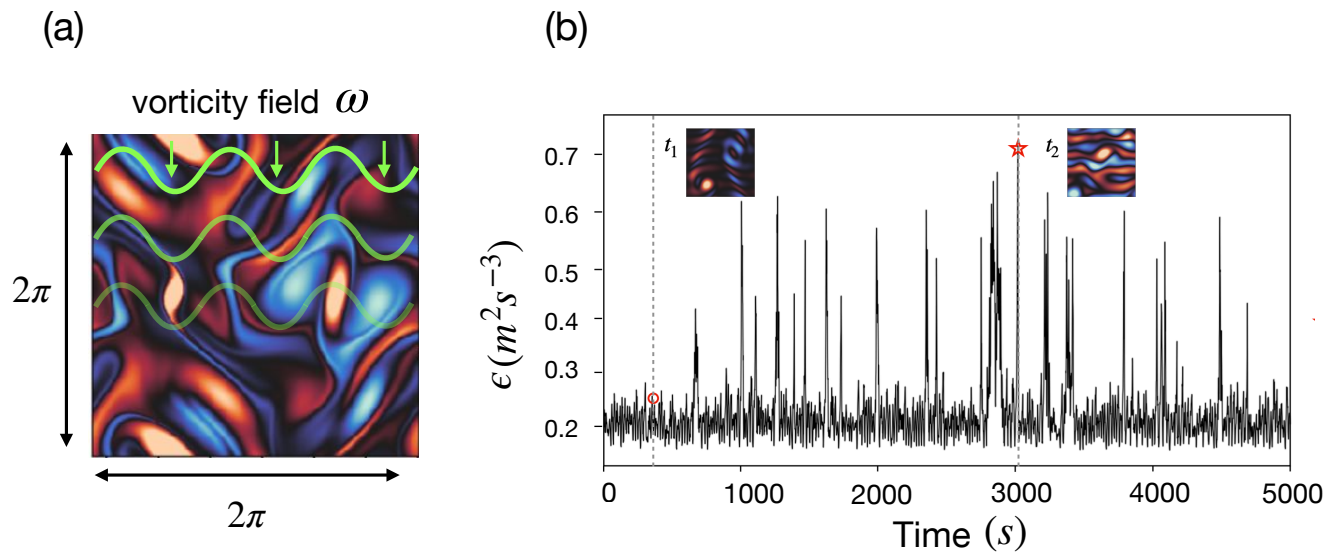

Figure SI 15: (a) A snapshot of the vorticity field for a Re≈100 case of the Kolmogorov flow, and (b) the energy dissipation rate over time for Re≈40. Highlighted with the red circle is the stable state, and the red star indicates one of the few extreme energy dissipation bursts.

method with 2/3 aliasing was developed to solve the equation [241]. For the time integration, a fourth order Runge Kutta and Crank Nicolson method from [242] was implemented.

Environment implementation. The Kolmogorov flow contained two control objectives: (1) mitigating energy dissipation, ϵ, and (2) increasing turbulent kinetic energy (TKE). While the obvious control objective is to predict and mitigate the energy burst, it can instead be leveraged to drive the system into a more turbulent regime, thereby increasing TKE and mixing. For the first objective, the energy dissipation rate is computed as $\epsilon = 2\nu < S_{ij}S_{ij} >$, where S_{ij} is the strain rate tensor [243]. The reward function penalizes both energy dissipation magnitude and events characterized as extreme. In this case, any energy dissipation value that is greater than three standard deviations is penalized. For the second objective, the average turbulent kinetic energy (TKE) is computed as: $\frac{1}{n^2}\sum_{i=1}^{n}\sum_{j=1}^{n}[\frac{1}{2}(u_i - U)^2 + (v_i - V)^2]$, where (u, v) are the x and y velocity components with mean fields of U and V, respectively. In this case, the reward is proportional to the TKE. The observations are the same for both objectives - equally spaced velocity point values across the domain. The actuation is formulated as amplitudes of a forcing wavenumber, where the amplitudes are the actions of the agent. Four wavenumbers are chosen to manipulate the system, and the control function took the form $c = a_1 f(k_{f_1}) + a_2 f(k_{f_2}) + a_3 f(k_{f_3}) + a_4 f(k_{f_4})$, where f is the sinusoidal forcing function with wavenumber k_f. The wavenumbers selected are greater than the forcing wavenumber, as any additional energy in the large-scale structures dominated the dynamics. In the case presented in this work, the specific forcing wavenumbers of $k_1, k_2, k_3, k_4 = 4, 5, 6, 7$ are chosen. For both objectives, the actions are added as a term to the reward function to penalize large actions and promote more efficient controllers.

5.10 Turbulent channel flow

Characteristic physics. The turbulent channel flow at $Re_\tau = 180$ is an ideal example of a fully developed turbulent flow. It exhibits the phenomena of wall-bounded flows in general, serving as an ideal case for understanding flow over surfaces. In HydroGym, the channel flow is solved on a 3D domain of size $(2\pi \times 2 \times \pi)$ discretized into $(72 \times 72 \times 72)$ cells. The streamwise and spanwise directions contain uniform

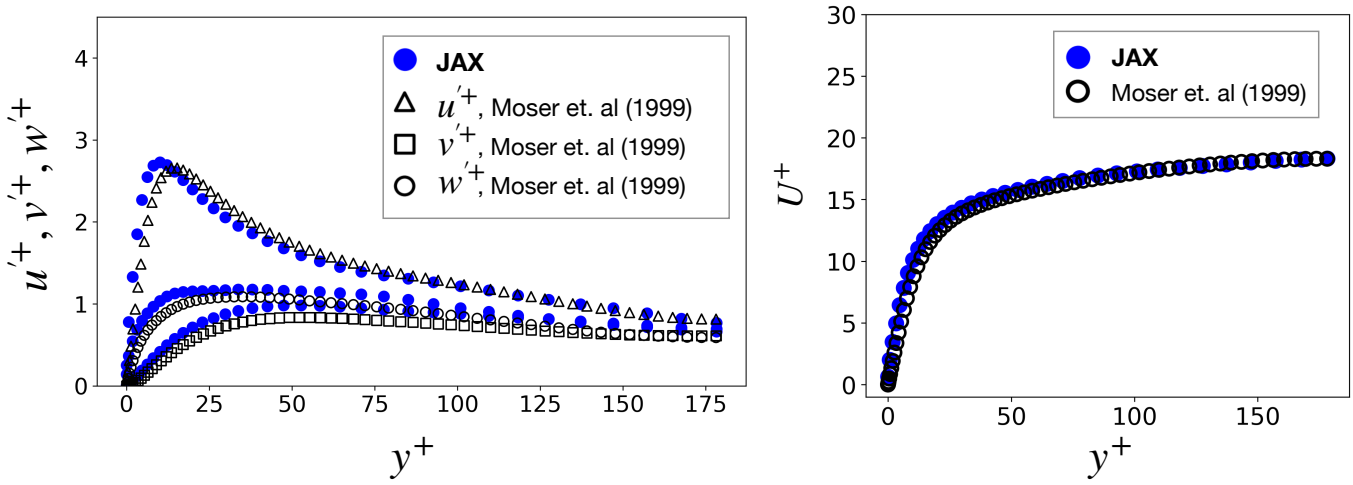

Figure SI 16: Dimensionless velocity fluctuations and mean velocity from the 3D channel flow compared to Moser et. al. DNS data.

spacing, while a tuneable hyperbolic tangent function is applied to the spacing in the wall-normal direction resulting in a finer grid close to the wall. A no-slip boundary condition is implemented at the walls, and periodic boundary conditions are applied in the streamwise and spanwise directions. A Neumann boundary condition is applied on the walls for pressure, $\frac{\partial p}{\partial z}_{wall} = 0$. The channel flow is driven by a constant, external body force in the x-direction, $f = (fx, 0, 0)$, to ensure a statistically stationary turbulent flow [244]. The flow is initialized with a laminar flow plus a random perturbation to generate turbulence. The forcing term sets the friction Reynolds number, Re_τ, through the following relation:

$$f_x = \frac{8\nu^2}{H^3} Re_\tau^2, \tag{27}$$

where H is the height of the channel. The velocity and pressure are both solved at the cell-centroids of the grid. The timestep, Δt, of the simulation is dynamically updated to ensure a maximum Courant number of 0.9 [245].

Numerical setup and validation. The 3D channel flow problem is solved with a finite-difference direct numerical solver (DNS) inspired by work of Vuorinen et. al. [245]. A compact way to numerically solve the derivatives in equation 14 is with differentiation matrices. Consider a derivative operator $\frac{\partial}{\partial x}$ and the velocity u and pressure p at the cell-centroid points. For a grid of size (N, N, N), the velocity and pressure can be expressed as column vectors of size $(N^3, 1)$, and the differentiation operators, say $\frac{\partial}{\partial x}$, as a sparse differentiation matrix $\mathbf{D_x}$ of size (N^3, N^3). All together, there are six differentiation matrices for velocity and six for pressure, $(\mathbf{D_x}, \mathbf{D_{xx}}, \mathbf{D_y}, \mathbf{D_{yy}}, \mathbf{D_z}, \mathbf{D_{zz}})$. The derivatives in the Navier-Stokes equations can then be computed with basic linear algebra $\frac{\partial u}{\partial x} \approx \mathbf{D_x} u$. For instance, the diffusive term in x would be computed as: $\nu(\mathbf{D_{xx}} u + \mathbf{D_{yy}} u + \mathbf{D_{zz}} u)$. The Poisson equation is used to solve for the pressure, using the formula: $\mathbf{M} p = \mathbf{D_x} u + \mathbf{D_y} u + \mathbf{D_z} u$ where $\mathbf{M}$ is the Poisson operator. This is a linear system, which is solved using the Biconjugate gradient solver from lineax `BiCGStab` [246]. Once the pressure is solved for, the velocity is corrected using the pressure gradient: $u^* = u - \mathbf{D_{x,p}} p$. To validate the solver, the dimensionless velocity fluctuations and mean velocity profile were plotted against the well-known Moser et. al. 1999 DNS study [40], as shown in Figure SI 16.

Environment implementation. The control task for the 3D channel flow is to locally minimize the wall-shear stress with synthetic jets. Specifically, zero-mass-flux jets with periodic blowing and suction are implemented

at the wall of the channel. This is essentially a wall-normal velocity distribution with a parabolic velocity profile, ensuring it is maximal at the centerline and smoothly decays to zero at the jet's edges. The actuation time is determined by the travel time of the velocity streaks, and ranges from $50\Delta t$ to $150\Delta t$ depending on the amount of jets implemented and the friction Reynolds number. The environment observation is the point value of the velocity in the x-direction, u, sampled from an off-wall location parallel to the jet locations. The sampling height was chosen as $y_s^+ \approx 15$, where there exists a strong correlation between wall-normal velocity and near-wall vortical structures [247]. Similar works have also used this sampling plane to ensure the best results [248]. The objective was to reduce the skin friction, or wall-shear stress, of the channel. The wall shear stress was computed as $\tau_w = \nu u(y)/y$, where y was chosen within the viscous sub-layer. Mathematically, this is equivalent to computing the velocity gradient with respect to the wall, since u(y=0) = 0 [249, 250]. To decrease τ_w, reward signal was calculated as the ratio between the magnitude of the uncontrolled wall shear stress and the controlled wall shear stress. Both GPPO and PPO used the same observations and rewards, with the main distinction being that the GPPO training uses the reward signal in the loss function to differentiate through the environment dynamics when updating the policy.